Single molecule spectroscopic studies of solute nanoconfinement in nanoporous membranes and on surfaces

by

Hamid Rashidi

B.S., University of Mazandaran, 2004
M.S., University of Tabriz, 2008

AN ABSTRACT OF A DISSERTATION

submitted in partial fulfillment of the requirements for the degree

DOCTOR OF PHILOSOPHY

Department of Chemistry
College of Arts and Sciences

KANSAS STATE UNIVERSITY
Manhattan, Kansas

2025

Abstract

This dissertation investigates the mass transport of molecules confined within anodic aluminum oxide (AAO) membranes and on PET microplastic surfaces, using fluorescence correlation spectroscopy (FCS) as a single-molecule detection technique. Rhodamine B (RhB) was employed as a fluorescent probe to study molecular dynamics and surface interactions. The first study focuses on understanding how solvent mixtures and solutes behave under nanoconfinement. To this end, RhB diffusion within 10 nm and 20 nm diameter AAO nanopores filled with ethanol/water mixtures was examined, with solvent compositions ranging from pure ethanol to pure water. The results revealed two distinct diffusion mechanisms, with mean diffusion coefficients, D_f (fast) and D_s (slow), differing by nearly two orders of magnitude. Both D_f and D_s were found to increase with pore size and were significantly lower than the bulk diffusion coefficient (D_b) of RhB in the free solution. The fast diffusion component, closely related to mixture viscosity, represents hindered bulk-like diffusion in the central pore regions and is influenced by hydrodynamic drag and electrostatic interactions with the nanopore surface. In contrast, slow diffusion likely involves the adsorption of RhB to the pore walls governed by an adsorption-mediated mechanism. Trends in the autocorrelation amplitude and D_s exhibited a strong dependence on solvent composition, mimicking RhB solubility behavior. D_s was smallest in pure ethanol and pure water and largest in intermediate mixtures, suggesting that RhB surface adsorption is strongest in the pure solvents and weakest where the dye is most soluble in intermediate mixtures.

The second study applies confocal fluorescence correlation spectroscopy (FCS) to investigate organic molecules adsorbed from aqueous solutions onto the surfaces of both virgin and post-consumer synthetic microplastics. The investigation includes fresh and artificially aged

polyethylene terephthalate (PET) plastics, with the aging process meticulously conducted in a UV-ozone chamber. Raman spectroscopy confirms the composition of the PET microplastics, while water contact angle measurements and surface roughness analyses reveal increased wettability and changes in surface texture with aging, consistent with surface oxidation. Rhodamine B (RhB) dye, used as a fluorescent probe in the FCS experiments, serves as an analog for organic pollutants commonly found on microplastics. FCS results demonstrate dye accumulation on the PET surfaces as the plastics age, with significantly slower dye motion on the surfaces compared to the bulk aqueous solution. The dye undergoes anomalous subdiffusion on the PET surfaces, with diffusion rates slowing dramatically and becoming more anomalous as the plastics age. The reduced mobility is likely due to ionic interactions or hydrogen bonding between the dye molecules and the oxidized plastic surfaces. These findings offer critical new insights into how microplastics accumulate and transport organic pollutants as they undergo environmental weathering, contributing to our understanding of the risks associated with microplastic pollution.

Single molecule spectroscopic studies of solute nanoconfinement in nanoporous membranes and on surfaces

by

Hamid Rashidi

B.S., University of Mazandaran, 2004
M.S., University of Tabriz, 2008

A DISSERTATION

submitted in partial fulfillment of the requirements for the degree

DOCTOR OF PHILOSOPHY

Department of Chemistry
College of Arts and Sciences

KANSAS STATE UNIVERSITY
Manhattan, Kansas

2025

Approved by:

Major Professor
Dr. Daniel A. Higgins

Copyright

Abstract

This dissertation investigates the mass transport of molecules confined within anodic aluminum oxide (AAO) membranes and on PET microplastic surfaces, using fluorescence correlation spectroscopy (FCS) as a single-molecule detection technique. Rhodamine B (RhB) was employed as a fluorescent probe to study molecular dynamics and surface interactions. The first study focuses on understanding how solvent mixtures and solutes behave under nanoconfinement. To this end, RhB diffusion within 10 nm and 20 nm diameter AAO nanopores filled with ethanol/water mixtures was examined, with solvent compositions ranging from pure ethanol to pure water. The results revealed two distinct diffusion mechanisms, with mean diffusion coefficients, D_f (fast) and D_s (slow), differing by nearly two orders of magnitude. Both D_f and D_s were found to increase with pore size and were significantly lower than the bulk diffusion coefficient (D_b) of RhB in the free solution. The fast diffusion component, closely related to mixture viscosity, represents hindered bulk-like diffusion in the central pore regions and is influenced by hydrodynamic drag and electrostatic interactions with the nanopore surface. In contrast, slow diffusion likely involves the adsorption of RhB to the pore walls governed by an adsorption-mediated mechanism. Trends in the autocorrelation amplitude and D_s exhibited a strong dependence on solvent composition, mimicking RhB solubility behavior. D_s was smallest in pure ethanol and pure water and largest in intermediate mixtures, suggesting that RhB surface adsorption is strongest in the pure solvents and weakest where the dye is most soluble in intermediate mixtures.

The second study applies confocal fluorescence correlation spectroscopy (FCS) to investigate organic molecules adsorbed from aqueous solutions onto the surfaces of both virgin and post-consumer synthetic microplastics. The investigation includes fresh and artificially aged

polyethylene terephthalate (PET) plastics, with the aging process meticulously conducted in a UV-ozone chamber. Raman spectroscopy confirms the composition of the PET microplastics, while water contact angle measurements and surface roughness analyses reveal increased wettability and changes in surface texture with aging, consistent with surface oxidation. Rhodamine B (RhB) dye, used as a fluorescent probe in the FCS experiments, serves as an analog for organic pollutants commonly found on microplastics. FCS results demonstrate dye accumulation on the PET surfaces as the plastics age, with significantly slower dye motion on the surfaces compared to the bulk aqueous solution. The dye undergoes anomalous subdiffusion on the PET surfaces, with diffusion rates slowing dramatically and becoming more anomalous as the plastics age. The reduced mobility is likely due to ionic interactions or hydrogen bonding between the dye molecules and the oxidized plastic surfaces. These findings offer critical new insights into how microplastics accumulate and transport organic pollutants as they undergo environmental weathering, contributing to our understanding of the risks associated with microplastic pollution.

Table of Contents

List of Figures

List of Tables

Acknowledgements

I would like to express my deepest gratitude to my major professor and research advisor, Dr. Daniel Higgins, for his unwavering guidance and support throughout my studies at Kansas State University. His mentorship has helped me grow into a more competent and independent researcher, and I sincerely appreciate his patience throughout my research journey. Beyond academics, I have also learned valuable life lessons and insights from him, for which I am truly grateful.

I am deeply grateful to Dr. Takashi Ito for his invaluable guidance and for instilling in me the importance of critical thinking. His thought-provoking questions during our weekly meetings challenged me, inspired new insights, and provided direction that was fundamental to my Ph.D. journey.

I am sincerely grateful to Dr. Christine Akines and Dr. Ryan Hansen for serving as my committee members and for their valuable feedback and suggestions on my research.

My heartfelt thanks go to the faculty and staff of the Chemistry Department at Kansas State University for their warm welcome, friendly environments, exceptional education, and continued support during my time at KSU.

I also wish to acknowledge the assistance and camaraderie of former and current members of Dr. Higgins' and Dr. Ito's research groups, including Dr. Lianjie Xue, Dr. Akash Nathani, Dr. Abdolhafiz Usman, Dr. Omid Shafiee, and others who have contributed to my learning experience.

Special thanks go to the Iranian Student Association, as well as to Dr. Ryszard Jankowiak and his wife, Majka, for their kindness and for making my stay in Manhattan more enjoyable.

I am thankful to the U.S. Department of Energy for their financial support, which made my research work possible.

Finally, a very special thank you to my best friend and wife, Mahboobe, for her constant encouragement and unwavering support through the ups and downs of graduate studies and for always keeping me motivated to reach the finish line.

Dedication

This work is dedicated to my beloved wife, Mahboobe, and to the cherished memory of my parents, who passed away while I was in Manhattan. They always wished to see me complete my PhD.

List of Acronyms and Definitions

1D/3D	One/Three Dimensional
A	Absorbance
AAO	Anodic Aluminum Oxide
AFM	Atomic Force Microscopy
APD	Avalanche Photodiode
ATR-FTIR	Attenuated Total Internal Reflection Fourier Transform Infrared
C	Concentration
CA	Chronoamperometry
CCD	Charge-Coupled Device
CV	Cyclic Voltammetry
D	Diffusion Coefficient
D_b	Bulk Diffusion Coefficient
D_f	Fast Diffusion Coefficient
D_s	Slow Diffusion Coefficient
DNA	Deoxyribonucleic acid
DLS	Dynamic Light Scattering
DOSY	Diffusion-Ordered Spectroscopy
EIS	Electrochemical Impedance Spectroscopy
ESR	Electron Spin Resonance
FCS	Fluorescence Correlation Spectroscopy
FRAP	Fluorescence Recovery After Photobleaching
FTIR	Fourier Transform Infrared

$G(\tau)$	Autocorrelation Function
GC-MS	Gas Chromatography-Mass Spectrometry
HPLC	High-Performance Liquid Chromatography
IC	Internal Conversion
ISC	Intersystem Crossing
J	Flux
NA	Numerical Aperture
NMR	Nuclear Magnetic Resonance
MF	Microfiltration
PET	Polyethylene Terephthalate
PFG-NMR	Pulsed-Field Gradient NMR
PMT	Photomultiplier Tube
PALM	Photoactivated localization microscopy
τ_D	Diffusion Time
SMT	Single-molecule tracking
STORM	Stochastic Optical Reconstruction Microscopy
QENS	Quasi-Elastic Neutron Scattering
RF	Radio Frequency
RO	Reverse Osmosis
S	Solubility
RhB	Rhodamine B
SEM	Scanning Electron Microscopy
SMFM	Single Molecule Fluorescence Microscopy

UF	Ultrafiltration
UV	Ultra-Violet
VR	Vibrational Relaxation

Chapter 1 - General Introduction

1.1 Importance of Chemical Separations

1.1.1 Historical Perspective of Separations

The history of chemical separation dates back to ancient times, evolving through empirical observations, alchemical experimentation, and scientific advancements. The development of separation techniques played a crucial role in the advancement of chemistry, allowing scientists to isolate, purify, and study-specific substances.

In ancient civilizations such as Persia, Egypt, and China,[1] rudimentary separation methods were employed, demonstrating their practical applications even before the formalization of chemistry. For instance, distillation was used to produce perfumes, essential oils, and alcohol. Ancient Egyptians are known to have used filtration techniques to purify water, while simple sedimentation was applied in metallurgy for extracting precious metals from ores.

Alchemists during the medieval period contributed significantly to separation techniques, particularly in the Islamic world and Europe. Distillation and sublimation were common techniques employed by alchemists, who sought to purify substances and transmute base materials into gold or create the "elixir of life."[2]

With the dawn of modern chemistry in the 17th century, scientists began understanding the principles behind chemical separations. In 1659, Johann Rudolf Glauber developed an early form of crystallization to isolate sodium sulfate, known as "Glauber's salt." The 17th and 18th centuries saw improvements in extraction, precipitation, and filtration methods, driven by the need to isolate pure substances for study.[1,3]

Antoine Lavoisier, often hailed as the father of modern chemistry, was a staunch advocate for the use of pure substances in his experiments. His emphasis on purity was

instrumental in the discovery of gases like oxygen, hydrogen, and nitrogen, which relied heavily on advancements in separation techniques such as distillation and compression. These breakthroughs laid the foundation for our modern understanding of elements and compounds.[1,3]

In the 19th century, fractional distillation and chromatography advances further revolutionized chemical separations. The work of Justus von Liebig in organic chemistry and Dmitri Mendeleev's periodic table development were based on an improved ability to isolate and characterize pure substances.[1]

The 20th century marked a significant turning point in the evolution of chemical separation techniques. This era witnessed a rapid expansion in the complexity and sophistication of these methods, driven by the needs of both industrial and laboratory chemistry. The development of chromatography in 1906, for instance, allowed for the separation of complex mixtures of organic compounds, particularly plant pigments, and paved the way for future innovations in the field.

The discovery of ion exchange techniques in the 1930s and 1940s further expanded the ability to separate ions from solutions. These methods became particularly important in the purification of drinking water and processing of radioactive materials during and after World War II.[1,3]

Advancements in mass spectrometry and electrophoresis during the mid-20th century enabled the separation and analysis of molecules based on their mass and charge. These techniques became critical in biochemistry, where they are used to study proteins, DNA, and other macromolecules.

In recent decades, separation techniques have become even more refined, enabling the isolation and characterization of highly complex substances at the molecular level. Innovations

such as high-performance liquid chromatography (HPLC), gas chromatography-mass spectrometry (GC-MS), and capillary electrophoresis have expanded the boundaries of what can be analyzed and purified.[1,3]

Today's separation techniques are not just confined to laboratory research; they have become integral to a wide range of industries. From pharmaceuticals to petrochemicals, environmental science to food processing, these techniques play a crucial role in ensuring the purity and quality of products. Moreover, the rise of green chemistry has spurred the development of more environmentally friendly separation methods, such as supercritical fluid extraction and membrane filtration. Expanding on this, the following sections provide a detailed exploration of membrane-based separation techniques, shedding light on the principles and applications that make these processes effective and sustainable.

1.1.2 Membrane Based Separations

Membrane-based chemical separations, a versatile and widely used class of techniques, selectively separates components of a mixture based on differences in size, charge, or chemical affinity. Thin and semi-permeable membrane barriers allow specific molecules to pass through while restricting others. This technology is highly efficient and finds applications in various industries, such as water purification,[4-6] pharmaceuticals,[7,8] food processing,[7,8] and energy production.[9]

Membrane separation works by allowing selective permeation of specific molecules through a membrane. The efficiency of the process depends on factors like pore size, membrane material, and the driving force applied. The driving force, which can be pressure,[10,11] a concentration gradient,[12] or an electric field,[13] is the energy that pushes the molecules through

the membrane. Based on the separation mechanism, membrane processes are classified into various categories, including microfiltration, ultrafiltration, nanofiltration, and reverse osmosis.

The microfiltration (MF)[14,15] process involves membranes with larger pore sizes (0.1 to 10 micrometers) and is commonly used to separate particles, bacteria, and large colloids from liquids. It operates under low pressure and is frequently applied in water treatment and food processing. Ultrafiltration (UF)[4,5] with smaller pore sizes (0.01 to 0.1 micrometers) separates macromolecules such as proteins and polysaccharides. It is effective in concentrating or purifying proteins, as well as in wastewater treatment to remove organic pollutants. Nanofiltration (NF)[16] uses even smaller pores (1 to 10 nanometers) and is suited for removing dissolved salts, sugars, and small organic molecules. This method is widely used in water softening, desalination, and the pharmaceutical industry to separate small molecules. In reverse osmosis,[17] membranes with very fine pore sizes (less than 1 nanometer) are used to reject almost all solutes, including ions, small molecules, and even microorganisms. This process is driven by high pressure and is extensively used for water desalination, allowing the production of drinking water from seawater.

Membranes can be classified based on their material, structure, and permeability characteristics. The two main types of membranes are organic polymer (polycarbonate, polyamide, polyether sulfone, and polyethylene glycol)[18,19] membranes and inorganic (metals and ceramics, such as alumina, titania, zirconia, and silica) membranes.[15,20] Together, these all have numerous applications in water and wastewater treatment,[4-6] the food and beverage industry,[7,8] the pharmaceutical industry,[7,8] gas separation,[21] and energy production.[9]

The advantages of membrane-based chemical separations are numerous. They are energy-efficient, scalable, and highly selective. Moreover, they are environmentally friendly,

often requiring less energy and producing less waste compared to traditional separation methods, making them a sustainable choice for various industries.[22]

As demand for cleaner water, energy-efficient separations, and sustainable industrial processes grows, membrane-based chemical separation will remain a critical area of research and application. Expanding on the foundational principles of membrane separation, the next section explores nanoporous membranes, which push the boundaries of selectivity and efficiency by using highly controlled pore structures to regulate molecular transport at the nanoscale, opening up new possibilities for advanced separations.

1.1.3 Nanoporous Membranes

Nanoporous membranes, as advanced materials, are pivotal in the separation and purification of chemical mixtures. These membranes, with pores on the nanometer scale, typically ranging from 1 to 100 nanometers in diameter, enable the precise and selective separation of molecules based on size, charge, and other physicochemical properties. As per the IUPAC classifications,[23] nanoporous materials are categorized as microporous materials with less than 2 nm pore size, mesoporous materials with 2–50 nm pore size, and macroporous materials with greater than 50 nm pore size.

Nanoporous membranes are distinguished by their highly controlled pore size, high surface area to volume ratio, and selective permeability. These characteristics make them particularly effective for separating small molecules or ions from complex mixtures. Nanoporous membranes separate chemical mixtures through different mechanisms, depending on the properties of the membrane and the substances being separated. The most common mechanisms include size exclusion,[24,25] which is also known as sieving, in which molecules larger than the membrane's pore size are retained while smaller molecules pass through. This principle is

particularly useful in separating macromolecules, proteins, and colloidal particles from solutions.[26,27] Other common mechanisms include charge-based separation,[28,29] in which the membrane is designed to have surface charges, allowing for the selective separation of ions based on their charge. Positively or negatively charged ions interact with the membrane surface, leading to ion selectivity. In chemical processing, this mechanism is often used in nanofiltration processes to remove multivalent ions from water or separate ionic species. Affinity-based mechanisms,[30,31] are also employed to achieve a separation. In this case, the separation medium is functionalized with chemical groups or coatings that selectively bind to specific molecules. This type of adsorptive separation is used in processes like protein purification,[32] where the membrane surface interacts specifically with target molecules based on their chemical affinity. Diffusion-controlled separations[33] are another form of separation in which selective diffusion of molecules through the nanopores allows certain molecules to pass through while hindering others, depending on their diffusion rates. In this process, molecules move based on their size, shape, or interaction with the nanopore surface. For instance, smaller or more mobile molecules diffuse faster through the membrane, while larger or more restricted molecules are retained. This principle is often utilized in gas separation and molecular filtration.[33] Most of these mechanisms in nanoporous systems occur when the solute is confined within the membrane, making it essential to understand the role of nanoconfinement in chemical separations.

1.1.4 Nanoconfinement and its Role in Separations

Nanoconfinement refers to the spatial restriction of molecules, ions, or particles on nanometer length scales, typically less than 100 nanometers. This restriction significantly alters the physical and chemical behavior of these species compared to their behavior in bulk environments. For example, the freezing points and glass transition temperatures of solvents are

often remarkably lowered under confinement.[34] The variation of the thermodynamic environment within the nanopores, where confined dimensions and a high surface-to-volume ratio influence the energetics of phase transitions, causes differences in their properties compared to the bulk.[35] Moreover, solvent and solute dynamics tend to slow down under nanoconfinement, reflecting increased interactions with pore walls and limited molecular mobility.[36]

The chemical compositions of nanoconfined mixtures may differ from those in the bulk solution.[37,38] These variations can arise from differential partitioning of mixture components into the nanopores, where specific components may preferentially enter the pores due to size compatibility or favorable interactions with the pore surfaces. Additionally, phase separation and the formation of solvent layers near the pore walls can further influence mixture composition. Simulations[38,39] and experimental[40,41] studies have shown that nanoconfined environments can induce layering of solvent molecules, with those closest to the pore surface becoming more ordered and oriented than those in the bulk. These surface layers can promote or limit behaviors important to chemical separations, such as the partitioning of solutes into nanopores[42] or their adsorption to pore surfaces.[43]

After exploring separation mechanisms across the nanoporous membranes, it is essential to focus on the broader concept of mass transport in chemical separations. Understanding the mechanisms behind mass transport, whether driven by diffusion, convection, or other forces—provides key insights into optimizing separation efficiency across various processes and materials.

1.2 Investigations of Mass Transport in Separations

Understanding how molecules move through different media, such as membranes or liquids, and how this affects separation efficiency is essential to understanding how chemical

separations can be improved and optimized. Mass transport is often quantified using two primary approaches, which are based on the concepts of flux and diffusion. Flux refers to the overall rate at which mass moves through a given area over time, considering various driving forces such as pressure, concentration gradients, and temperature. Diffusion is a crucial mechanism of mass transport which refers to the random motion of molecules from regions of high concentration to regions of low concentration. Fick's laws of diffusion govern this process:

Fick's First Law in one dimension:

$$\boldsymbol{J = -D\frac{dC}{dx}} \tag{1.1}$$

This law describes the flux *J* (the amount of substance passing through a unit area per unit of time), where *D* is the diffusion coefficient, *C* is the concentration, and *x* is the spatial coordinate. The negative sign indicates that diffusion occurs from high to low-concentration regions.

Fick's Second Law in one dimension:

$$\boldsymbol{\frac{\partial C}{\partial t} = D\frac{\partial^2 C}{\partial x^2}} \tag{1.2}$$

This law predicts how concentration changes over time due to diffusion, providing dynamic information about how quickly species move in a system. Understanding the diffusion coefficient (*D*) is critical to designing efficient separation processes. Factors influencing *D* include temperature, viscosity, molecular size, and the nature of the medium.

The following section delves into the methods used to study mass transport processes, focusing on both ensemble and single-molecule measurements to gain deeper insights into molecular dynamics and behavior during separations.

1.2.1 Ensemble Methods

In ensemble methods, flux and diffusion measurements provide critical insights into the mass transport dynamics of chemical separations, aiding in optimizing processes across various applications, as outlined below. This section explores the principles and mechanisms that underlie each method.

1.2.1.1 Flux Methods

Mass transport is often quantified in separation processes using flux methods, which describe the rate at which species are transferred per unit area of a membrane or interface. Various techniques, including optical[44] and electrochemical methods,[45,46] can be employed to study mass transport, allowing for efficient separation and analysis of complex mixtures.

Mass transport in separation processes occurs through different mechanisms, depending on the species nature and the type of driving force applied. The primary modes of mass transport include diffusion, convection, and migration.[47] Diffusion, is the movement of molecules or ions from a region of high concentration to a region of low concentration, driven by a concentration gradient. Fick's laws of diffusion describe the relationship between the concentration gradient and the flux. Convection is the transport of particles due to bulk fluid movement, such as flow through a membrane or along a channel. Convective transport is often driven by external forces like pressure. Migration, which in electrochemical systems refers to the movement of charged species (ions), is motion driven by an electric field. Optical and electrochemical techniques, which are explained below, play a critical role in monitoring these mass transport processes.

1.2.1.1.1 Optical Methods

Optical methods provide non-invasive ways to monitor mass transport in separation processes. These techniques rely on light-based interactions with the material being studied, such as absorption, emission, and light scattering.

Absorption spectroscopy[48,49] measures light absorption by a substance at specific wavelengths to determine how concentration changes over time. The mass transport rate can be calculated by measuring how the concentration of a solute varies in time on either side of a membrane or other separation medium.

Beer's Law describes the relationship between absorbance (A) and concentration (C) of a solute:

$$\boldsymbol{A = \epsilon . l . C} \qquad 1.3$$

Where ϵ is the molar absorptivity, l is the path length of light through the sample, and C is the concentration. By tracking absorbance changes, the flux of species during transport can be determined.

Fluorescence spectroscopy[44] is a technique that employs fluorescent dyes as markers or tracers, and their emission is monitored to track their movements. This method is beneficial for studying the diffusion of small molecules or ions in liquids or across membranes. Changes in fluorescence intensity over time in the solution on either side of the membrane provides insights into the diffusion coefficient and flux of the target molecules.

Light scattering (LS),[50,51] occurs when light passes through a medium containing particles or molecules, causing the light to be reflected in various directions due to interactions with these particles. The intensity of scattered light is directly proportional to the concentration of particles or molecules in the solution. As solutes pass through a membrane, the concentration of solutes

changes on both sides, leading to measurable variations in scattering intensity. This method monitors the absolute scattering intensity as a function of solute concentration over time. By tracking these changes in scattering intensity as the solution concentration fluctuates (e.g., due to diffusion), the flux of solutes across the membrane can be accurately determined.

1.2.1.1.2 Electrochemical Methods

Electrochemical methods play a vital role both in separating charged species, particularly in ion-exchange membranes, electrodialysis, and battery technologies and in detecting and quantifying their passage through a membrane. In the former, these methods rely on the application of an electric field to drive the movement of ions through the membrane. Several different forms of electrochemical methods are employed to measure their concentrations after permeation through the membrane. Some of these can be used to follow analyte flux during the separation as well as for determining their concentrations in a receiving solution. For this purpose, a porous or metal mesh working electrode was positioned inside the receiving chamber of a two-chamber cell, making contact with the membrane surface. This setup enables the diffusion flow of the substance under study through the membrane to be converted into an electric current.

Chronoamperometry (CA)[52] measures the current response over time when a constant potential or a step-change in potential is applied across an electrochemical cell. The current is directly related to the flux of electroactive species being transported. The diffusion coefficient and transport properties of the species involved can be determined by analyzing the current-time profile. Analyzing the current-time profile can give insights into both the transient behavior immediately following a step change in potential and the steady-state response once reactive currents have stabilized and mass transfer limitations become apparent. This method provides

critical information about long-term, steady-state reaction rates under specific conditions. For instance, in ion-selective membranes, the flux of specific ions can be monitored through the corresponding current measurements, making CA a powerful tool for studying transport properties in electrochemical systems.

Electrochemical impedance spectroscopy (EIS)[53] is used to study the resistance and capacitance of materials as a function of frequency, providing insights into the transport of ions and electrons in a separation process. In separation applications, EIS helps characterize the movement of ions through membranes and interfaces, as well as the role of diffusion, migration, and reaction kinetics in controlling mass transport. Experimentally, EIS involves perturbing an electrochemical system with an AC voltage or current over a wide frequency range and measuring the response. By assuming the system is linear and time-invariant, EIS models the relationship between the input and output signals across frequencies. The resistance of a liquid electrolyte, bulk and grain boundary conductivities in solid polycrystalline electrolytes, charging/discharging of the electric double layer at the electrolyte interface, the capacitive behavior of the double layer (influenced by electrode surface morphology and electrolyte composition), electrode charge-transfer kinetics, adsorption/desorption phenomena, and mass transfer (diffusion of species to the electrode surface) all exhibit distinct time constants In systems like fuel cells or electrodialysis membranes, EIS can distinguish between bulk ion transport and surface adsorption phenomena, allowing for the investigation of membrane properties and operating conditions.

Cyclic voltammetry (CV)[54] is a crucial tool used to measure the redox behavior of electroactive species by cycling the potential of an electrode. Changes in the current at different potentials provide vital information about the transport and reaction kinetics of the species being

studied. CV is indispensable for investigating ion transport in membranes, as well as for analyzing the behavior of charged species in separation processes such as electroplating or electrodeposition. Experimentally, the potential of a working electrode is cycled between two set potential limits, inducing the successive oxidation and reduction of an electroactive species, which may either be dissolved in solution or adsorbed onto the electrode surface. This cycling process drives electron transfer reactions at the electrode-solution interface, allowing the study of redox behavior, reaction kinetics, and the transport properties of the species involved. This method can be used to study the deposition or dissolution of materials during mass transport processes, particularly in separations involving metal ions or electrodeposition. The current result of the change in concentration as a function of time changes, which, by monitoring the mass changes, can quantify the flux of ions or molecules.

1.2.1.2 In situ Studies of Diffusion

1.2.1.2.1 Nuclear Magnetic Resonance spectroscopy

Nuclear Magnetic Resonance (NMR) spectroscopy is one of the most potent methods for studying diffusion, allowing for ensemble diffusion studies to be performed directly within the separations medium. This technique provides molecular-level insights into how substances move through different phases, including liquids, gels, and membranes, by measuring the translational motion of molecules over time. NMR can directly measure diffusion within the interior environment of membrane pores (i.e., in situ), whereas the methods discussed in the previous section are primarily used to assess the analyte concentrations in either the feed or receiving solutions.

NMR diffusion experiments rely on the interaction between magnetic fields and the nuclear spins of atoms (typically hydrogen, ^{1}H, ^{13}C, and ^{19}F). These interactions allow for tracking molecular displacements over time.

The most common NMR technique for studying diffusion is Pulsed-Field Gradient NMR (PFG-NMR),[55] also known as Diffusion-Ordered Spectroscopy (DOSY). This method applies magnetic field gradients to encode spatial information about molecular motion, allowing the diffusion coefficient to be measured directly. PFG-NMR allows for the precise measurement of molecular diffusion in a sample by applying two magnetic field gradients separated by a delay period. During this period, molecules diffuse, and their displacements cause phase shifts in their NMR signals. By measuring how the signal decays as a function of the gradient strength, the diffusion coefficient (D) can be extracted.

The general form of the NMR signal attenuation due to diffusion is described by the Stejskal-Tanner equation:

$$\boldsymbol{I = I_0 \exp\left(-\gamma^2 g^2 \delta^2 D(\Delta - \frac{\delta}{3}\right)} \qquad 1.4$$

Where I is the attenuated NMR signal intensity, I_0 is the initial signal intensity, γ is the gyromagnetic ratio of the nucleus being observed, g is the strength of the magnetic field gradient, δ is the duration of the gradient pulse, D is the diffusion coefficient, and Δ is the diffusion time (the time between the two gradient pulses).

The exponential decay of the NMR signal with increasing gradient strength provides a direct measure of the diffusion coefficient. This allows the observation of ensemble diffusion—how a population of molecules moves collectively over time. Even though diffusion studies by NMR are a non-invasive and non-destructive method and can give direct and accurate access to

diffusion coefficients and molecular-level insight, they still provide ensemble data that is averaged over a large number of molecules in the sample.

1.2.1.2.2 Quasi-Elastic Neutron Scattering

Quasi-elastic neutron scattering (QENS)[56,57] is a powerful technique used to study the dynamics of atoms and molecules in materials, particularly their diffusive motions on a microscopic scale. Unlike purely elastic scattering, where no energy exchange occurs between the neutrons and the sample (giving information on static structures), quasi-elastic scattering involves a small energy transfer that reflects slow, dynamic processes such as diffusive motion. Because the energy shifts are small but measurable, it is called "quasi-elastic." This energy exchange corresponds to motions such as diffusion, rotation, or vibration of the molecules in the sample.

1.2.1.2.3 Fluorescence Recovery After Photobleaching

Fluorescence recovery after photobleaching (FRAP)[58-61] is an optical technique that can provide quantitative information on the diffusion of molecules in any optically transparent medium. FRAP allows the measurement of the diffusion coefficient of fluorescence tracers within the separations medium. This technique is well suited to understanding molecular diffusion as it relates to separation processes, where mass transport governs the rate and efficiency of separations, offering direct insight into molecular mobility.

A typical FRAP experiment involves several procedures. The molecules of interest, such as proteins, small molecules, or nanoparticles, must either be fluorescent or they must be tagged with a fluorescent dye. Fluorescence is usually excited by a laser. The fluorescent species must also be easily photobleached. Photobleaching of the sample involves illuminating a small, well defined region of the sample with intense laser light, causing the fluorescent dye in that region to

lose its ability to emit light (photobleaching). A dark spot where fluorescence is no longer observed is produced. The photobleached region is usually circular in shape based on the profile of the incident laser beam. Immediately after photobleaching the laser intensity is reduced to allow for the recovery of fluorescence in the photobleached region to be monitored. Recovery occurs by diffusion of unbleached fluorescent molecules back into the bleached region. The rate of fluorescence recovery directly reveals the diffusion rate of the molecules. The fluorescence recovery curve (fluorescence intensity vs. time) obtained in these experiments is fitted to mathematical models to extract the diffusion coefficient D. Faster recovery corresponds to higher diffusion rates, while slower recovery indicates more restricted diffusion.

The fluorescence recovery process in FRAP can be modeled using appropriate diffusion equations. The simplest model assumes a homogenous medium and free diffusion, where the recovery of fluorescence follows an exponential curve:

$$\boldsymbol{F(t) = F_0(1 - e^{-t/\tau})} \qquad 1.5$$

Where F(t) is the fluorescence intensity at time t, F_0 is the pre-bleaching fluorescence intensity, and τ is the characteristic recovery time related to the diffusion coefficient *D*. By analyzing τ, the diffusion coefficient *D* can be estimated using the relationship:

$$\boldsymbol{D = \frac{R^2}{4\tau}} \qquad 1.6$$

Where *R* is the radius of the bleaching area, and this equation directly measures how fast molecules diffuse through the medium.

While FRAP is a powerful technique for measuring molecular diffusion, it is also an ensemble method, meaning it provides averaged data over a large number of molecules in the sample. This makes it difficult to detect heterogeneity in molecular motion or surface-interacting molecules, such as slow-diffusing or immobilized species, which are critical for understanding

complex systems. Additionally, FRAP has limitations in detecting adsorbed molecules, as it is most well suited to studies of freely diffusing molecules that can rapidly move back into the bleached region.

1.2.2 Single Molecule Methods

Ensemble-averaged methods, as mentioned above, tend to mask molecular-level details of the diffusion mechanism, which can be particularly important in nanostructured materials. These methods provide an average over many molecules, potentially overlooking key variations in behavior, such as heterogeneity in diffusion rates or the presence of surface-adsorbed or immobilized molecules. Such details are crucial for fully understanding how molecular motion is influenced by the unique environments within nanostructures. Single-molecule methods offer unparalleled insight into the behavior of individual molecules, which can reveal details about heterogeneities and rare events often hidden in bulk measurements.

The most common single-molecule methods for studying molecular diffusion include single-molecule tracking (SMT),[62-65] photoactivated localization microscopy (PALM),[66,67] stochastic optical reconstruction microscopy (STORM),[68] and fluorescence correlation spectroscopy (FCS).[69-71] Each offers unique insights into molecular behavior.

Single-molecule tracking (SMT) [62-65] allows observing individual molecules' motion over time by following their trajectories. This method enables the direct observation of diffusion patterns, including random walks and constrained or directed movements, offering insight into how molecules move through different environments. By tracking the positions of single molecules with high spatial and temporal resolution, SMT can reveal heterogeneities in diffusion, which are often masked by ensemble-averaged methods. SMT is beneficial in studying

complex media, such as cells or nanostructured materials, where molecular motion may vary significantly in different regions.

Photoactivated localization microscopy (PALM)[67] and stochastic optical reconstruction microscopy (STORM)[68] are super-resolution techniques that break the diffraction limit of light to allow imaging of molecular structures and diffusion at a much finer resolution than conventional microscopy techniques. PALM was developed using photoactivatable or photoconvertible fluorescent proteins as switchable probes, while STORM initially utilized synthetic organic dyes. Despite these differences in their historical development, both techniques share similar instrumentation. PALM and STORM use fluorescent molecules that can be turned on and off (photoactivated or photoswitched) to build a high-resolution image. In the context of diffusion studies, closely related methods that rely upon the same principle of super-resolved localization can visualize how molecules move within highly crowded environments or confined spaces, providing spatial information about diffusion at nanometer scales. While PALM and STORM represent critical advances in materials imaging that led to the awarding of the 2014 Nobel Prize in Chemistry, these methods and many other super-resolution analogs have not yet been widely used in studies of diffusion within separations related materials. Previous work from our group,[72-77] and from the group of Christoph Brauchle[78-82] represent primary studies of diffusion in separations methods that have employed SMT methods closely related to STORM.

Fluorescence correlation spectroscopy (FCS)[69-71] is a highly sensitive technique that measures fluctuations in fluorescence intensity as molecules diffuse through the small detection volume of a confocal optical microscope. By analyzing these fluctuations, FCS provides quantitative data on diffusion coefficients and molecular concentration. FCS is particularly useful for studying diffusion in small volumes or confined environments, such as nanopores or

membranes, and can detect fast and slow diffusing species, revealing details about how molecular confinement affects diffusion.

1.3 Objective and Motivation of Present Research

Biofuels extracted from organic materials such as plants are considered as a sustainable alternative to fossil fuels, with significant potential to address current global issues such as climate change. Biofuels can help reduce greenhouse gas emissions that contribute to climate change, decrease our dependence on fossil crude oil, enhance energy security, and promote sustainable development worldwide.[83] The most common biofuel used globally is ethanol, with the United States being the world's largest producer. Most of the ethanol used as vehicle fuel in the U.S. is produced domestically, with production concentrated in the Midwest region.[84]

Ethanol is most commonly used in its dehydrated form, requiring water removal. However, conventional distillation methods pose challenges, as the ethanol-water mixture forms an azeotrope at approximately 95.6% ethanol and 4.4% water by volume under atmospheric pressure.[85] At this azeotropic point, the liquid and vapor phases have identical compositions, with a boiling point of 78.2°C, slightly lower than that of pure ethanol (78.4°C). This highlights the unique thermodynamic properties of this composition. To achieve higher purity and surpass the azeotropic point, alternative methods must be used to break the ethanol-water azeotrope. Common industrial methods include chemical dehydration, pressure-swing distillation,[86] azeotropic distillation,[87,88] extractive distillation,[89] adsorption on molecular sieves,[90] and pervaporation.[91,92]

Current ethanol dehydration methods are costly and energy-intensive,[93] prompting exploration of alternative approaches. The use of nanoporous materials has emerged as a promising strategy, leveraging surface interactions in which certain species are preferentially

adsorbed to the pore surface. However, nanoconfinement of solutions leads to changes in their properties, as described above. Importantly, computational studies show that in 1 nm slits of anodic aluminum oxide (AAO), water molecules are selectively adsorbed from an ethanol-water mixture, leading to a shift in composition compared to the bulk mixture. [38]

This research uses FCS for probing molecular dynamics, diffusion, and mass transport of solute molecules within nanoporous anodic aluminum oxide (AAO) membranes. By monitoring the interactions and movements of fluorescent dyes, FCS can provide insights into how solvent molecules, such as ethanol and water, behave under nanoconfinement; this information cannot be easily accessed in ensemble or bulk studies. They also review how solute molecules interact with complex solvent mixtures within the pores and with the pore surfaces. The research reported in this dissertation highlights the critical importance of solvent nanostructure in influencing the molecular dynamics within the pores and the important role of surface interactions, partitioning effects, and solubility of probe molecules. FCS provides a more detailed understanding of the complex interplay of forces affecting molecular transport in confined spaces, paving the way for the design of more effective membranes with properties better suited to specific applications.

The motivation for the second part of this study is related to environmental issues. Plastic pollution is a pervasive ecological issue, with large plastic objects breaking down into microplastics through exposure to sunlight, air, and mechanical forces. This process alters their chemical composition and creates secondary microplastics capable of adsorbing and later releasing toxic organic substances. Such behavior poses risks to both ecosystems and human health, as microplastics can serve as vectors for pollutants like pesticides, pharmaceuticals, and industrial chemicals. While many studies have investigated the sorption mechanisms of organic

compounds by microplastics, there needs to be more knowledge about the detailed interactions at the molecular level. This gap, especially regarding the mobility and adsorption of organic contaminants on fresh and aged microplastics, underscores the need for new experimental approaches. Fluorescence correlation spectroscopy (FCS) offers a promising method for probing these interactions at trace concentrations, revealing crucial details about surface adsorption and diffusion behaviors. By studying these mechanisms on fresh and UV-light-exposed polyethylene terephthalate (PET) microplastics, this research aims to advance our understanding of microplastic contamination's environmental and health consequences.

1.4 Overview of This Dissertation

This dissertation consists of six chapters. Chapter 1 introduces key concepts, including a brief history of chemical separations, as well as background material on fluorescence spectroscopy, and nanoconfinement, and their roles in chemical separations. It emphasizes the importance of studying solute behavior in confined environments, where physical barriers and surface interactions significantly influence molecular diffusion.

Chapter 2 details the experimental setup and methodologies used throughout this research. It introduces the basics of fluorescence spectroscopy and describes the confocal microscope employed for FCS, Raman microscopy, and, briefly, nuclear magnetic resonance (NMR) spectroscopy.

Chapter 3 investigates the diffusion of solute molecules in nanoporous AAO membranes with pure ethanol and ethanol-water mixtures at varying concentrations (0%, 2%, 5%, 10%, and 33% by volume). The diffusion coefficients of molecules in different pore sizes and environments are quantified by analyzing fluorescence time transients and autocorrelation functions obtained through FCS. The results demonstrate how nanoconfinement affects diffusion

rates, providing critical insights into how confinement influences molecular dynamics at the nanoscale.

Chapter 4 extends this investigation to a wider range of ethanol-water mixtures in AAO nanopores, focusing on the adsorption and solvation of RhB dye in these environments. FCS measurements are used to observe the real-time behavior of individual molecules interacting with the pores' surfaces.

Chapter 5 examines FCS studies of RhB diffusion on fresh and aged virgin and post-consumer polyethylene terephthalate (PET) plastics, further expanding the scope of the research to different material systems.

Chapter 6 concludes the dissertation with a summary of the key findings and their implications for studying nanoconfined systems. It also discusses potential applications of this research in areas such as chemical separations and suggests directions for future research.

Chapter 2 - Materials and Characterization Methods

2.1 Fluorescence Spectroscopy

2.1.1 Principles of Light-Matter Interactions

When light interacts with molecules, if the frequency of the light matches the natural frequencies of the molecules, the light energy can be absorbed. It causes molecules to be excited from a lower energy state (usually the ground state) to a higher energy state. Here is a detailed look at what happens after a molecule is excited and the various transitions that can occur. This transition is virtualized by the Jablonski diagram shown in Figure 2.1.

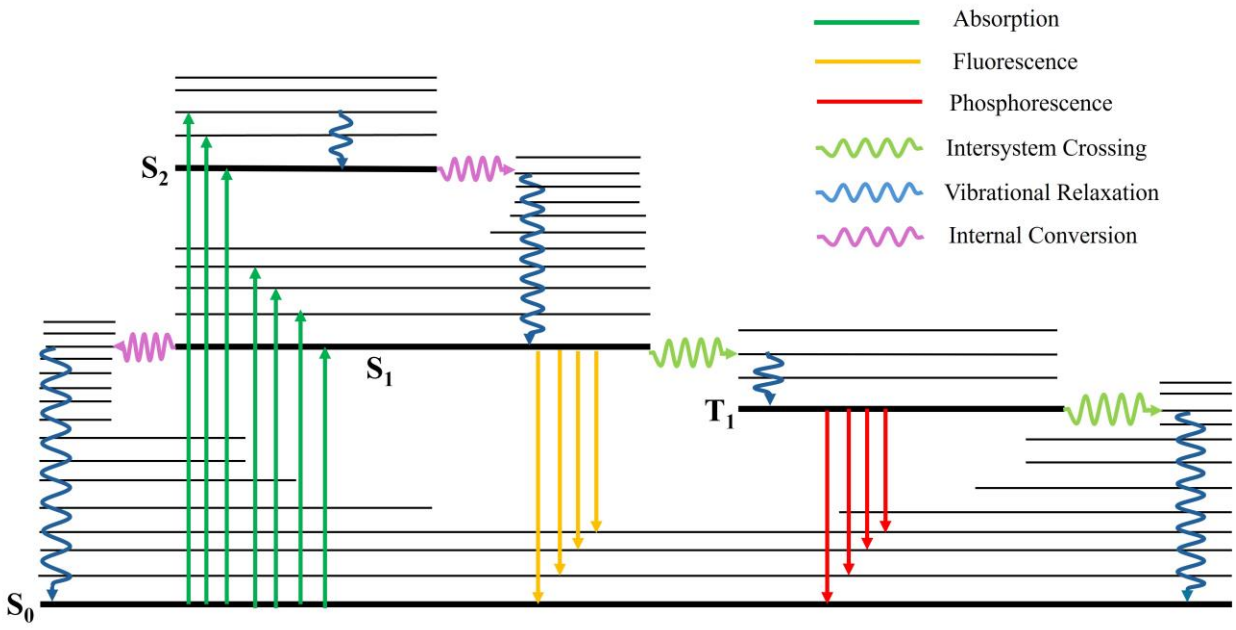

Figure 2.1 A Jablonski diagram. Possible transitions between electronic and vibrational energy levels, including absorption/excitation, internal conversion, vibrational relaxation, intersystem crossing, phosphorescence and fluorescence processes.

A molecule absorbs a photon, the straight green arrows, elevates an electron from a lower energy orbital (ground state, usually denoted as S_0) to a higher energy orbital (excited state, such as S_1 or S_2)). The excited molecules can release their gained energy in the form of radiation

(emitting a photon) or in nonradiative ways and return to the ground state by conversion of their excess energy directly into heat.

Nonradiative transitions:

Internal Conversion (IC), shown by the wavy purple occurs when a molecule transitions between electronic states of the same spin multiplicity, such as S_2 to S_1. Vibrational Relaxation (VR), shown by the wavy blue arrows, is when a molecule loses excess vibrational energy within the same electronic state through collisions with surrounding molecules, dissipating energy as heat. Intersystem Crossing (ISC), wavy green arrows, is when a molecule transitions from an excited singlet state (S_n) to a triplet state (T_m), where the electron spins are no longer paired. These transitions involve an electron spin flip. Quenching is the interaction with other molecules that increases the non-radiative deactivation rate of an excited molecule from its excited state.

Radiative transitions:

The fluorescence process, designated by the straight downward pointing orange arrows, occurs after the molecule is excited from the ground electronic state (S_0) to an excited singlet state (S_1 or higher). Typically, the molecule is promoted to a higher vibrational level within the excited state; once it has relaxed to the lowest vibrational level of the excited electronic state, it returns to the ground electronic state. During this transition, the molecule emits a photon of light. However, because the molecule has lost some energy through vibrational relaxation, the emitted photon has less energy and a longer wavelength than the absorbed photon. This shift to a longer wavelength is known as the Stokes shift.

The phosphorescence process, designated by the straight downward pointing red arrows, occurs after intersystem crossing to a triplet state (T_1). The molecule returns to the ground state (S_0) in this case by emitting a photon.

2.1.2 Ensemble Fluorescence Measurements

Ensemble fluorescence measurements were conducted to observe the average fluorescence behavior of the entire population of molecules in the sample. These measurements were performed using a spectrofluorometer, which captures the collective fluorescence signal from all molecules within the illuminated volume. The goal was find the fluorescence intensity and, peak position, and environmental effects on fluorescence.

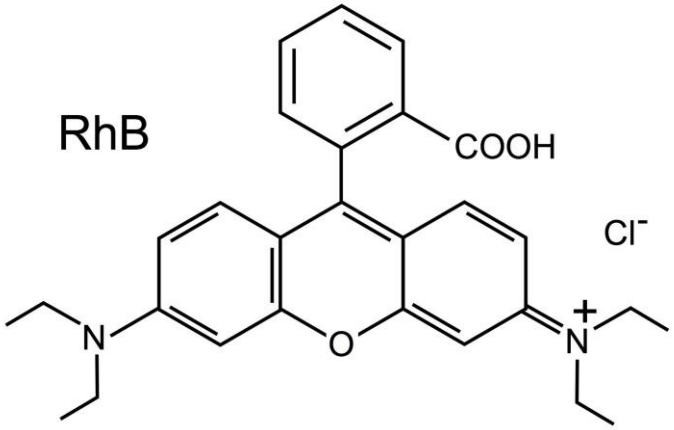

Figure 2.2 Chemical structure of Rhodamine B.

A benchtop spectrofluorometer (FluoroMax-2) was used for ensemble fluorescence measurements. A xenon arc lamp was used to provide a broad spectrum of excitation light, which was passed through a monochromator to select the appropriate wavelength for exciting the fluorescent molecules. In this study, the 532 nm wavelength was chosen for its ability to efficiently excite the Rhodamine B (RhB) dye. The emission spectra were recorded using a photomultiplier tube (PMT) detector, with a second monochromator tuned to measure emission for wavelengths of 540-700 nm. The widths of the excitation and emission monochromator slits were adjusted to 5 nm as a means to control the intensity of excitation light and the resolution of the emission spectra. All spectra were recorded at 1 nm increment and 1 second integration times. The excitation and emission spectra were recalibrated each time the instrument was used.

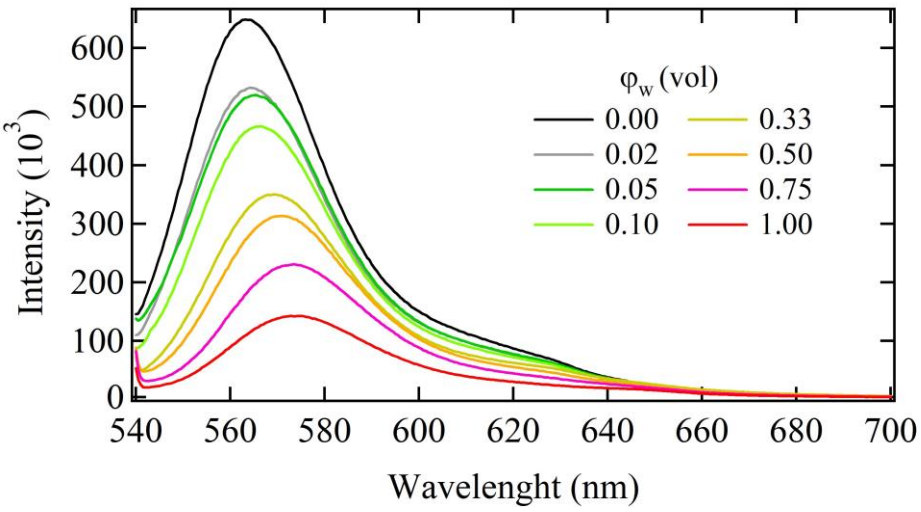

Figure 2.3 Rhodamine B fluorescence spectra as a function of volume fraction of water, φ_w, in ethanol-water mixtures. Fluorescence was excited at 532 nm. The fluorescence intensity decreased as the water content increased and exhibited a 10 nm red shift in peak position from pure ethanol to pure water.

Rhodamine B (RhB) dye (from Sigma-Aldrich) was used for much of the work performed in this dissertation. Its structure is shown in Figure 2.2. A stock solution of 200 µM RhB prepared in pure ethanol and pure water (HPLC grade) was further diluted to obtain the dye solutions employed in individual experiments. These solutions were all 4 mL in volume and contained RhB at 100 nM concentrations. Solutions of pure ethanol, pure water, and mixtures of 2%, 5%, 10%, 33%, 50%, and 75% (by volume) water and ethanol were prepared. All ensemble fluorescence spectra were recorded in a clean 1 cm pathlength quartz cuvette. Data analysis and plotting were performed using the Igor Pro v.6 software package. Figure 2.3 shows representative ensemble spectra for the entire range of ethanol/water mixtures explored. The maximum peak positions of the spectra shifted to the red by around 10 nm from pure ethanol to pure water. Simultaneously, the fluorescence intensity with increasing water content. The RhB fluorescence intensity at 580 ± 20 nm in water was approximately 27% of that in ethanol.

2.1.3 Fluorescence Correlation Spectroscopy (FCS)

FCS is based on the autocorrelation of fluorescence time series data (i.e., time transients) over time. It is performed under equilibrium conditions and can be used to extract quantitative results on molecular diffusion, solute molecular binding kinetics, photophysical properties, and reaction rates. This dissertation used the FCS method to study solute diffusion in solutions, on surfaces, and in nanoporous membrane materials.

In FCS experiments, laser light is focused onto the sample through a high numerical (NA) objective lens. A NA = 1.3 oil immersion objective was used in this dissertation. The focal volume in this configuration was typically less than 1 μm^3 (1 femtoliter).[94-96] Since nanomolar concentrations of fluorescent dye were employed in these studies (see below), the excitation and detection of fluorescence from a femtoliter volume means that, on average, approximately one fluorescent molecule would reside in the focal volume at any instant in time. In fact, the average number of molecules in the focal volume at 2 nM would be approximately 1 molecule. For this reason, the confocal time transients recorded and reported in this dissertation represent single-molecule level data. As the FCS results average these data over many single molecules, FCS may be considered a “near-single-molecule” or a “sub-ensemble” method.

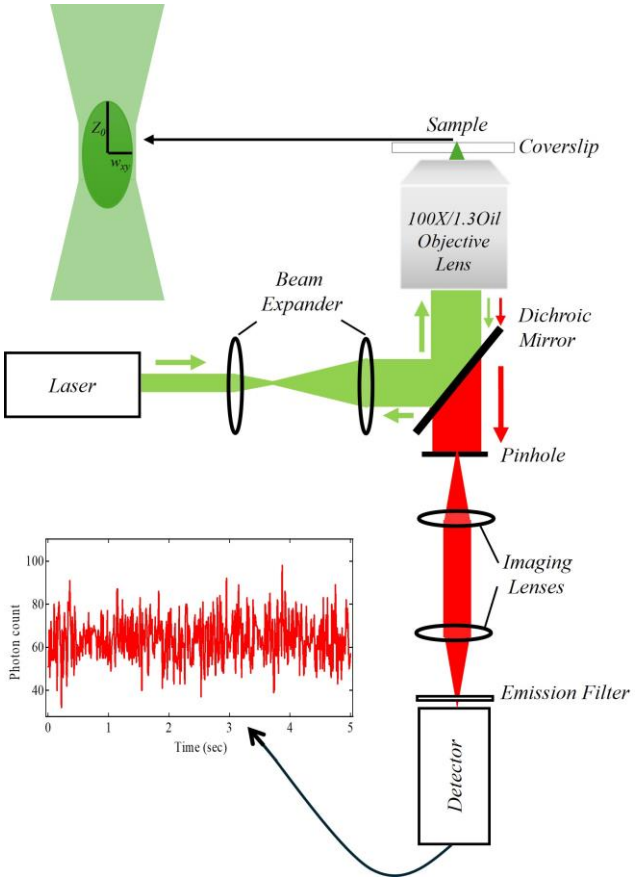

Figure 2.4 Schematic diagram showing the confocal microscope used in fluorescence correlation spectroscopy experiments in this dissertation.

Figure 2.4 provides a schematic of the confocal microscope used in this dissertation. The microscope was constructed in-house and is built upon a commercial inverted light microscope (Nikon TE-200). The FCS setup was optimized to study the diffusion dynamics and interactions of fluorescent molecules within confined environments. The optical path begins with the excitation source, which in this case was a solid-state laser emitting 532 nm light. Lasers are commonly employed in single molecule studies due to their inherent stability, low noise levels, and good optical beam quality, which is crucial for efficiently exciting the fluorescent probe molecules and for achieving the smallest possible excitation and detection volume. The solid-state laser operates in continuous wave mode, providing a stable output for extended periods of

time, as is essential for precise fluorescence correlation spectroscopy (FCS) measurements. Before reaching the microscope, the laser beam passes through a telescope to expand its diameter. This step is critical because the laser beam size needs to match the back aperture of the objective lens. The laser beam is actually expanded slightly beyond the size of the back aperture to ensure overfilling, which guarantees that the full numerical aperture (NA) of the objective lens is utilized. The importance of this step lies in the ability of the expanded beam to achieve a tightly focused spot in the sample, ensuring that the focal volume is as small as possible, typically on the order of less than a femtoliter (10^{-15} liters). This small focal volume is necessary for sensitive FCS measurements, as it increases the signal-to-noise ratio in molecular diffusion studies. Once the beam is expanded, it reflects from a dichroic mirror (Chroma 550 DCLP), which serves as a beam splitter. The dichroic mirror reflects the laser light toward the sample while allowing the emitted fluorescence to pass through. The laser beam is then directed to the objective lens, a high NA lens (Nikon Plan Fluor, 100X, 1.3 NA). The objective lens focuses the laser beam onto the sample, creating a tightly confined oval-shaped observation volume. The dimensions of this volume are around half a micron in diameter and 2 microns in depth, which is ideal for detecting stochastic fluorescence fluctuations as molecules diffuse in and out of the volume.

When the fluorophores within the sample enter the focused laser spot, they become excited, and fluorescence is emitted. This emitted light is collected by the same objective lens used to focus the excitation laser. The fluorescence signal passes back through the dichroic mirror, while residual laser light is blocked. This ensures that only the emitted fluorescence is detected, allowing for dark-field detection of the individual molecules. After passing through the dichroic mirror, the fluorescence passes through a tube lens that focuses the light onto a pinhole

placed in the primary image plane of the microscope. The pinhole is a critical component in the confocal microscope setup, as it filters out light that from outside the focal plane (i.e., out-of-focus light). This ensures that the detected fluorescence is only from the microscope focal volume, improving the spatial resolution of the measurement and helping to achieve optimum signal-to-noise levels. The pinhole size is carefully selected (50 μm diameter) to match the size of the magnified Airy pattern produced by the diffraction-limited focus of the microscope.

Following the pinhole, the emitted light is sent through a convex lens, which collimates the light as it travels onward towards the detector. Immediately prior to the detector, it passes through a second lens that focusses the light onto the detector. The collimated region between the lenses ensures that no light is lost in the process. Immediately prior to incidence on the detector, the emitted fluorescence passes through a bandpass filter (Chroma, 580/40m), which was carefully selected to match the Rhodamine B emission spectrum. This filter allows light at the desired emission wavelength (around the peak emission of the dye) to pass through while blocking any stray light or background fluorescence at other wavelengths. Using a bandpass filter improves the signal-to-noise ratio by allowing detection of only the relevant fluorescent signal.

The filtered fluorescence is then detected using an avalanche photodiode detector (APD, Perkin Elmer SPCM-AQ-141R), which is a single photon counting device. APDs are highly sensitive detectors capable of registering individual photon arrival events. This is crucial for FCS measurements that detect very small numbers of photons emitted from a few fluorophores in the observation volume. The APD used in this setup is operated in photon time-stamping mode, which records the exact time each photon is detected with high temporal resolution. The electrical pulses output by the APD were counted using a National Instruments counter/timer

board (PCIe-6612) that records the detected photon arrival times. In this dissertation, a 25 MHz clock was. employed as the timer in time-stamping mode, allowing detection of photons with 40 ns time resolution. This high temporal resolution is necessary for accurately capturing the rapid fluorescence fluctuations caused by the diffusion of molecules in and out of the observation volume. Time-stamping data were recorded using a National Instruments Labview program written in-house. The data were autocorrelated and analyzed using C++ code and Igor Pro (Wavemetrics) macros written in-house. The analyzed data provides quantitative information about the diffusion coefficients, molecular concentrations, and interaction dynamics of the fluorophores under study.

2.1.3.1 Fluorescence Time Transients

In FCS, fluorescence time transients are recorded from the confocal volume over time. The fluorescence time transients are characterized by rapid, stochastic fluctuations in intensity that occur as fluorescent molecules randomly diffuse through the confocal volume, causing the number of fluorescent molecules contributing to the signal to change over time. The resulting fluorescence signal shows periods of higher intensity, or bursts of fluorescence, when one or more probe molecules are in the detection volume and periods of lower intensity when no or fewer probe molecules are in the detection volume. The time transients are typically “noisy” in this sense, because the measurements are based on random diffusion events. The intensity might seem erratic, with no apparent pattern when visualized on short time scales, but analyzing these fluctuations over longer timescales provides meaningful insights.

The magnitude of the intensity fluctuations reflects the number of fluorescent molecules in the observation volume at a given instant in time. When taken relative to the overall average signal level, larger fluctuations indicate fewer molecules are present, while smaller fluctuations

suggest more molecules are present. This is because, with a small number of molecules, individual molecules entering or exiting the detection volume cause more significant changes in relative intensity. The timescale of the fluctuations is related to how fast the molecules move through the detection volume. Faster diffusion results in rapid fluctuations, while slower diffusion causes more prolonged intensity bursts.

The fluorescence time transients also incorporate characteristics that point to the occurring of molecular interactions such as binding and unbinding events. When molecules undergo binding, they become immobilized in the detection volume and their diffusion necessary slows as a result. This is reflected in the time transients as longer-duration bursts in fluorescence. In the case of binding, these bursts take on a distinct appearance in that the signal rises and remains constant (within shot noise limits) during the binding event. In the case of anomalously slow diffusion, the signal instead gradually rises and falls in time as the molecule slowly moves through the detection volume. Changes in environmental conditions, such as viscosity, temperature, or the presence of binding partners, can influence molecular diffusion and, thus, the appearance of the time transients. In general, the appearance of dramatically different burst lengths can indicate the presence of multiple species with different diffusion rates, and different diffusion mechanisms, suggesting complex interactions or heterogeneous environments.

The time transients can also provide insight into photophysical behaviors such as blinking, which arises from triplet state formation. If a molecule enters a non-fluorescent state (such as when it crosses to a triplet state), the fluorescence intensity will sharply drop, creating distinctive dips in the time transient. These dips show up as fast-decaying components in the autocorrelation analysis. If the molecule photobleaches, the drop in intensity is permanent and

the signal only increases later when a new molecule diffuses into the detection volume. Further analysis of the time transient data in FCS studies can effectively provide quantitative results revealing the time scales over which these phenomena occur as well as their overall contributions to the observe fluctuations.

2.1.3.2 Autocorrelation

Further analysis of the time transient data described above is frequently accomplished by calculating its autocorrelation function. This constitutes the basis for FCS method. Autocorrelation, also known as serial correlation, can be understood with a simple analogy. It's like comparing today's weather to yesterday's or the day before. It measures how a variable's value at a one-time delay is related to its previous values in a time series.[97] For example, in the case of temperatures measured daily over a month, the value on the 1st day might be more similar to the value on the 2nd day than to the value on the 30th day. The more similar values are across time, the stronger the correlation. If values further apart in time show little similarity, the correlation weakens as the time delay increases.

Autocorrelation is most commonly used in the context of time series (i.e. time transient) data, where observations occur sequentially over time. It helps identify patterns or trends that repeat over intervals, such as daily temperatures or stock prices. In a time series, the value of a variable at a certain point in time is often related to its value at earlier points. The time between each pair of data points being compared in this way is known as the lag time, or the time delay. Autocorrelation quantifies the degree of correlation between pairs of data points as a function of the lag time. The final correlation value represents the average correlation exhibited by a large number of pairs of data points at a particular lag time.

By autocorrelation of the time transient data obtained in a single molecule experiment, FCS can provide information about the diffusion coefficient of fluorescent molecules in the sample. Analysis of the time transient data involves calculating its autocorrelation function as described in the next section. Diffusion timescales are extracted from the autocorrelation function by fitting it to an appropriate model for the correlation decay. In the absence of the background noise, the amplitude of the autocorrelation function is inversely related to the number of fluorescent molecules in the detection volume. This allows FCS to provide precise estimates of molecular concentration in solutions along with the diffusion time.[69,98,99] More importantly, the shape and decay of the fluorescence–autocorrelation function can reveal molecular interactions such as binding and unbinding events.

2.1.4 Autocorrelation Data and Fitting Models

Autocorrelation functions are obtained from the confocal fluorescence time transient data by applying Eq. 2.1. In this process, each point in the autocorrelation function is obtained by simply multiplying two copies of the time transient together, with one copy delayed by time τ. The normalized average of this product is then obtained and plotted as a function of τ. The autocorrelation function is normalized by the square of the mean fluorescence count rate across the full transient length. A representative autocorrelation decay is shown in Figure 2.5a. Analysis of the autocorrelation decay provides quantitative data on the mean rate of dye diffusion and the mean concentration of molecules detected within the focal volume, while also providing evidence of the mechanism behind the observed fluorescence fluctuations. In this dissertation, the fluctuations of interest all arise from movement (i.e., diffusion) of individual molecules within the sample. Hence, these data provide information on the mechanisms of molecular mass transport.

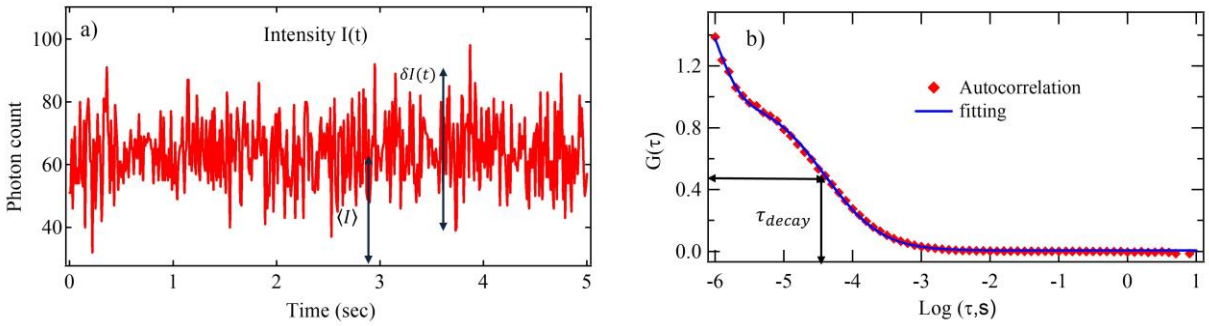

Figure 2.5 a) Fluorescent time transient showing intensity fluctuations over time for 2 nM rhodamine B in ethanol and b) autocorrelation function (red dots) calculated from the time transient in a). The blue line shows a fit to the 3D diffusion model shown in Eq. 2.2.

All time transients (see Figure 2.5a) were autocorrelated as given in Eq. 2.1.

$$\boldsymbol{G(\tau) = \frac{\langle \delta I(t) \delta I(t+\tau) \rangle}{\langle I(t) \rangle^2}} \qquad 2.1$$

In Eq. 2.1, $I(t)$ represents the time transient, and $\delta I(t)$ and $\delta I(t + \tau)$ are the intensity difference between the $I(t)$ data and the mean fluorescence intensity $\langle I \rangle$, and between $I(t + \tau)$ and the mean intensity $\langle I \rangle$, respectively. The angular brackets indicate that the average value is calculated over t. The data plotted as red dots in Figure 2.5b represent the autocorrelation decay from bulk solution calculated from the time transient shown in Figure 2.5a.

In order to obtain information on the mechanism of molecular diffusion, the concentration of diffusing molecules, and the rate at which the molecules diffuse, the autocorrelation data must be fit to an appropriate model. The chosen model depends upon the expected dimensionality of diffusion, and its mode, whether Fickian free diffusion or anomalous diffusion. The data shown in Figure 2.5 was obtained from 2 nM rhodamine B (RhB) in bulk ethanol solution. Thus, the results were fit to a model for free 3D Fickian diffusion. The model employed is given in Eq. 2.2.[100] The quality of the fit provides evidence as to whether or not the correct model (i.e., diffusion mechanism) has been chosen.

$$\boldsymbol{G(\tau) = A_o + \frac{1}{N}\left[A_b\left(1 + \left(\frac{\tau}{\tau_{D_b}}\right)\right)^{-1}\left(1 + \left(\frac{\tau}{\tau_{D_b}}\right)\left(\frac{1}{\gamma^2}\right)\right)^{-1/2}\left(1 + A_r e^{-k\tau}\right)\right]} \qquad 2.2$$

Where A_o is a constant (≈ 0), N is the average number of molecules in the detection region, and A_b is the fractional contribution of free 3D diffusion to the autocorrelation decay. A_r and k are the fractional amplitude and rate constant, respectively, for contributions from faster fluctuations that were too fast (near ~ 10^{-6} s and not related to transitional motion) to result from dye diffusion. The average residence time of individual RhB molecules in the detection region is given by τ_{D_b}, while $\gamma = w_z/w_{xy} \approx 4$,[101] where w_z and w_{xy} are, respectively, the experimentally determined axial and radial dimensions of the detection region. τ_{D_b} is related to the diffusion coefficient of the dye in bulk solution, D_b, by $\tau_{D_b} = w_{xy}^2/4D_b$. The known value of D_b for RhB in aqueous solution (430 $\mu m^2/s$[102,103]) was employed to determine w_{xy} (and w_z) from the measured value of τ_{D_b}, also in aqueous solution.

Derivation of Fitting Model for One Dimensional Diffusion

In this dissertation, much of the data collected reflects diffusion of dye molecules in 1D due to their confinement within anodic alumina nanopores. Therefore, a model for 1D diffusion was employed due to the narrow pore size (10 nm and 20 nm), which causes restriction of dye movement in the x or y dimension, with freedom of movement only in the z direction (along the long pore axis) in the lab frame. Specifically, a two-component 1D fitting model was used because of the observation of two distinct mechanisms having diffusion times that differed from each other by 10-100-fold. One of these mechanisms is related to those molecules moving close to the pore surface and interacting with the surface, resulting in slower diffusion. The other is related to those molecules that mostly move in the center of the pores and exhibit relatively faster diffusion. The final model is given in Eq. 2.3.

$$\boldsymbol{G(\tau) \approx A_o + \frac{1}{N}\left[\left(A_f\left(1+\left(\frac{\tau}{\tau_{D_f}}\right)\left(\frac{1}{\gamma^2}\right)\right)^{-1/2} + A_s\left(1+\left(\frac{\tau}{\tau_{D_s}}\right)\left(\frac{1}{\gamma^2}\right)\right)^{-1/2}\right)\right]} \qquad 2.3$$

Where, A_o is a constant (≈ 0), N is again the average number of molecules in the detection region, A_f and A_s represent the fractional contributions of fast and slow diffusion to each autocorrelation decay, τ_{D_f} and τ_{D_s} are the average residence times of the molecules in the detection region for molecules exhibiting fast and slow diffusion, and $\gamma = w_z/w_{xy} \approx 4$, as described above. Our measurements are performed in the z-direction, where the beam propagates along the pore direction, resulting in a longer path compared to the x or y directions, which are perpendicular to the laser beam and have shorter radii. In the case of diffusion in the x or y directions alone, the term $\left(\frac{1}{\gamma^2}\right)$ is removed from the equation above.

The derivation of this model (Eq. 2.3) begins with a definition of the dye concentration fluctuations along the z axis within the nanopores:

$$\boldsymbol{\delta C(z,t) = C(z,t) - \langle C \rangle} \qquad 2.4$$

Where δC is the concentration fluctuation and $\langle C \rangle$ is the average dye concentration. The concentration correlation function is then,

$$\boldsymbol{\phi(z,z',\tau) = \langle \delta C(z,t) \delta C(z',t+\tau) \rangle} \qquad 2.5$$

Where t is time, τ is a time delay and the brackets <> indicate that the average is calculated in time. Since the correlation function (ϕ) does not depend on absolute time, it is possible to write:

$$\boldsymbol{\phi(z,z',\tau) = \langle \delta C(z,0) \delta C(z',\tau) \rangle} \qquad 2.6$$

Since only the fluctuations caused by diffusion are of interest, $\delta C(z,t)$ is determined by Fick's second law (in 1 D):

$$\boldsymbol{\frac{\partial(\delta C(z,\tau))}{\partial t} = D\nabla^2(\delta C(z,\tau)) = D\frac{\partial^2(\delta C(z,\tau)}{\partial^2 z}} \qquad 2.7$$

The standard method of solving a partial differential equation of the form of Eq. 2.7 is to apply the Fourier transform of Eq. 2.7 under the proper boundary conditions.

The boundary conditions were defined by considering that the microscope focus was positioned 5 μm inside the pores. Again, the pores are oriented in the z direction and are 50 μm long, so it is assumed that the system is infinite along the z direction. Thus, the boundary condition is

$$\boldsymbol{\delta C(z,\tau) = 0} \quad \text{at} \qquad \boldsymbol{z = \pm\infty} \tag{2.8}$$

The Fourier transform, which converts spatial coordinates to frequency coordinates, is defined and applied to the concentration fluctuations as follows:

$$\boldsymbol{F_{\vartheta_z}[\delta C(z,\tau)] = \widetilde{C}(\vartheta_z,\tau) = \frac{1}{\sqrt{2\pi}}\int_{-\infty}^{+\infty} e^{iz\vartheta_z}\delta C(z,\tau)\, dz} \tag{2.9}$$

The inverse Fourier transform, which converts frequency coordinates back to spatial coordinates, is again applied to concentration fluctuations as follows:

$$\boldsymbol{F_z^{-1}\left[\widetilde{C}(\vartheta_z,\tau)\right] = \delta C(z,\tau) = F_z^{-1}\left[\widetilde{C}(\vartheta_z,\tau)\right] = \frac{1}{\sqrt{2\pi}}\int_{-\infty}^{+\infty} e^{-iz\vartheta_z}\widetilde{C}(\vartheta_z,\tau)\, d\vartheta_z} \tag{2.10}$$

Taking the Fourier transform of Eq. 2.7 gives

$$\boldsymbol{\frac{d\widetilde{C}(\vartheta_z,\tau)}{d\tau} = -D\vartheta_z^2\widetilde{C}(\vartheta_z,\tau)} \tag{2.11}$$

Which has the solution

$$\boldsymbol{\widetilde{C}(\vartheta_z,\tau) = \widetilde{C}(\vartheta_z,0)e^{-D\vartheta_z^2\tau}} \tag{2.12}$$

This solution is used to calculate the concentration correlation fluctuation equation.

Eq. 2.6 consists of $\delta C(z,0)$ and $\delta C(z',\tau)$ which are copies of the same concentration fluctuation function with one starting at arbitrary time 0 and the other at the time delay τ. They both are a function of position along the pore axis, with coordinates define as z and z'. Since the experiments being performed deal with dilute, ideal solutions at time 0, when the system is supposed to be in equilibrium, there is no correlation between the concentration of one point and

the concentration of another point along the z axis. The concentration fluctuation in the detection volume should be Poisson distributed, so the mean-square fluctuation is equal to the average concentration.

$$\langle \boldsymbol{\delta C}(\boldsymbol{z},\boldsymbol{0})\boldsymbol{\delta C}(\boldsymbol{z'},\boldsymbol{\tau})\rangle = \langle \boldsymbol{C}\rangle \boldsymbol{\delta}(\boldsymbol{z}-\boldsymbol{z'}) \qquad 2.13$$

Applying the Fourier transform, and inverse Fourier transform to the second fluctuation function in Equation 2.6:

$$\boldsymbol{\phi}(\boldsymbol{z},\boldsymbol{z'},\boldsymbol{\tau}) = \langle \boldsymbol{\delta C}(\boldsymbol{z},\boldsymbol{0})\boldsymbol{\delta C}(\boldsymbol{z'},\boldsymbol{\tau})\rangle = \langle \boldsymbol{\delta C}(\boldsymbol{z},\boldsymbol{0})\boldsymbol{F}_{\boldsymbol{z'}}^{-\boldsymbol{1}}\big[\widetilde{\boldsymbol{C}}(\boldsymbol{\vartheta}_{\boldsymbol{z}},\boldsymbol{\tau})\big]\rangle \qquad 2.14$$

Due to the linear nature of the Fourier transform and averaging, the inverse transform can be factored out, resulting in

$$\boldsymbol{\phi}(\boldsymbol{z},\boldsymbol{z'},\boldsymbol{\tau}) = \boldsymbol{F}_{\boldsymbol{z'}}^{-\boldsymbol{1}}\langle \boldsymbol{\delta C}(\boldsymbol{z},\boldsymbol{0})\widetilde{\boldsymbol{C}}(\boldsymbol{\vartheta}_{\boldsymbol{z'}},\boldsymbol{\tau})\rangle \qquad 2.15$$

Inserting Eq. 2.12 into Eq. 2.15 it is found that

$$\boldsymbol{\phi}(\boldsymbol{z},\boldsymbol{z'},\boldsymbol{\tau}) = \boldsymbol{F}_{\boldsymbol{z'}}^{-\boldsymbol{1}}\big(\langle \boldsymbol{\delta C}(\boldsymbol{z},\boldsymbol{0})\widetilde{\boldsymbol{C}}(\boldsymbol{\vartheta}_{\boldsymbol{z}},\boldsymbol{0})\boldsymbol{e}^{-\boldsymbol{D}\boldsymbol{\vartheta}_{\boldsymbol{z}}^{\boldsymbol{2}}\boldsymbol{\tau}}\rangle\big) \qquad 2.16$$

Applying the definition of the Fourier transform leads to:

$$\boldsymbol{\phi}(\boldsymbol{z},\boldsymbol{z''},\boldsymbol{\tau}) = \boldsymbol{F}_{\boldsymbol{z'}}^{-\boldsymbol{1}}\left[\langle \boldsymbol{\delta C}(\boldsymbol{z},\boldsymbol{0}).\frac{\boldsymbol{1}}{\sqrt{\boldsymbol{2\pi}}}\int_{-\infty}^{+\infty}\boldsymbol{e}^{-\boldsymbol{iz''}\boldsymbol{\vartheta}_{\boldsymbol{z}}}\boldsymbol{\delta C}(\boldsymbol{z''},\boldsymbol{0})\,\boldsymbol{e}^{-\boldsymbol{D}\boldsymbol{\vartheta}_{\boldsymbol{z}}^{\boldsymbol{2}}\boldsymbol{\tau}}\,\boldsymbol{dz''}\rangle\right] \qquad 2.17$$

Since the second exponential is not a function of *z''*, it can be written as

$$\boldsymbol{\phi}(\boldsymbol{z},\boldsymbol{z''},\boldsymbol{\tau}) = \boldsymbol{F}_{\boldsymbol{z'}}^{-\boldsymbol{1}}\big[\langle \boldsymbol{\delta C}(\boldsymbol{z},\boldsymbol{0})\boldsymbol{F}_{\boldsymbol{\vartheta}_{\boldsymbol{z''}}}[\boldsymbol{\delta C}(\boldsymbol{z''},\boldsymbol{0})]\boldsymbol{e}^{-\boldsymbol{D}\boldsymbol{\vartheta}_{\boldsymbol{z}}^{\boldsymbol{2}}\boldsymbol{\tau}}\,\boldsymbol{dz''}\rangle\big] \qquad 2.18$$

Since $e^{-D\vartheta_z^2\tau}$ remains constant for a given τ, it can be pulled out from the averaging brackets <>. Additionally, due to the linearity of both the Fourier transform and averaging, it can also be pulled out and expressed as

$$\boldsymbol{\phi}(\boldsymbol{z},\boldsymbol{z''},\boldsymbol{\tau}) = \boldsymbol{F}_{\boldsymbol{z'}}^{-\boldsymbol{1}}\big[\boldsymbol{e}^{-\boldsymbol{D}\boldsymbol{\vartheta}_{\boldsymbol{z}}^{\boldsymbol{2}}\boldsymbol{\tau}}\boldsymbol{F}_{\boldsymbol{\vartheta}_{\boldsymbol{z''}}}\langle \boldsymbol{\delta C}(\boldsymbol{z},\boldsymbol{0})\boldsymbol{C}(\boldsymbol{z''},\boldsymbol{0})\rangle\big] \qquad 2.19$$

Using Eq. 2.19 and the inverse Fourier transform, the final expression for the concentration correlation can be obtained as

$$\boldsymbol{\phi}(z,z'',\tau) = \boldsymbol{F}_{z'}^{-1}\left[\langle C\rangle \delta(z-z')e^{-D\vartheta_z^2\tau}\right] = \frac{\langle C\rangle}{\sqrt{2\pi}}\int_{-\infty}^{+\infty} e^{-i\vartheta_{z(z'-z)}}\, e^{-D\vartheta_z^2\tau}\, d\vartheta_z \qquad 2.20$$

Next, we examine the laser intensity and beam profile, where near the beam waist, the profile can be approximated by a Gaussian distribution. The beam intensity in the z-direction can be expressed as

$$\boldsymbol{\rho}(z) = \boldsymbol{\rho_0} e^{-2z^2/w_z^2} \qquad 2.21$$

Where ρ_0 represents the intensity at the center of the beam, and w_z is the radius of the confocal volume in the z direction. At this radius, the intensity drops to $\rho(z) = \frac{\rho_0}{e^2}$. The intensity of detected photons at any given time at the detector can be expressed as

$$\boldsymbol{I}(t) = \int dz\, \rho(z) q C(z,t) \qquad 2.22$$

Where q is the combined efficiency coefficient for excitation and emission. The time averaged signal is then given by the following equation.

$$\langle I\rangle = \frac{1}{T}\int_0^T dt \int dz\, \rho(z) q C(z,t) = q\langle C\rangle \rho_0 \int dz e^{-2z^2/w_z^2} = q\langle C\rangle \rho_0 \left(\frac{\pi}{2}\right)^{1/2} w_z \qquad 2.23$$

The intensity fluctuation just results from the change in the dye concentration. So, it given by

$$\delta I(t) = I(t) - \langle I\rangle = \int dz\, \rho(z) q \delta C(z,t) \qquad 2.24$$

Since the autocorrelation function of fluorescence intensity fluctuation, $g(t)$, is independent of absolute time, it can be expressed as

$$g(t) = \frac{\langle \delta I(t)\delta I(t+\tau)\rangle}{\langle I\rangle^2} = \frac{\langle \delta I(0)\delta I(\tau)\rangle}{\langle I\rangle^2} \qquad 2.25$$

Applying the Eq. 2.24,

$$g(t) = \frac{1}{\langle I\rangle^2}\iint dz dz' \rho(z)\rho(z') q^2 \langle \delta C(z,0)\delta C(z',\tau)\rangle \qquad 2.26$$

substituting Eq. 2.20 in 2.26,

$$\boldsymbol{g(t) = \frac{q^2\langle C\rangle}{\sqrt{2\pi}\langle I\rangle^2} \iint dz dz' \rho(z)\rho(z') \int_{-\infty}^{+\infty} e^{-i\vartheta_z(z'-z)}\, e^{-D\vartheta_z^2\tau}\, d\vartheta_z} \qquad 2.27$$

The main integral part is the Fourier transform of the beam profile described by Eq. 2.21. By substituting Eq. 2.21 into Eq. 2.27, it obtains:

$$\boldsymbol{g(t) = \frac{q^2\langle C\rangle\rho_0^2}{\sqrt{2\pi}\langle I\rangle^2} \iint_{-\infty}^{+\infty} dz dz' e^{-2z'^2/w_z^2} e^{-2z^2/w_z^2} \int_{-\infty}^{+\infty} e^{-i\vartheta_z(z'-z)}\, e^{-D\vartheta_z^2\tau}\, d\vartheta_z} \qquad 2.28$$

From the Integral Handbook, it is known that $\int_{-\infty}^{+\infty} e^{-ax^2 \pm ibx} dx = \sqrt{\frac{\pi}{a}} e^{-b^2/4a}$.

Therefore, by applying the known integral formula to Eq. 2.28, we can rewrite it as

$$\boldsymbol{g(t) = \frac{\sqrt{\pi}q^2\rho_0^2 w_z^2\langle C\rangle}{2\sqrt{2}\langle I\rangle^2} \int_{-\infty}^{+\infty} e^{-\frac{\vartheta_z^2 w_z^2}{8}} e^{-\frac{\vartheta_{z'}^2 w_z^2}{8}} e^{-D\vartheta_z^2\tau}\, d\vartheta_z} \qquad 2.29$$

Then, since $z=z'$ and $\vartheta_z = \vartheta_{z'}$ (the same explanation for Eq. 2.13), substituting Eq. 2.23 gives

$$\boldsymbol{g(t) = \frac{1}{\sqrt{2\pi}\langle C\rangle} \int_{-\infty}^{+\infty} e^{-\vartheta_z^2\left(\frac{w_z^2}{4}+D\tau\right)}\, d\vartheta_z} \qquad 2.30$$

Carrying out the integral in Eq. 2.30 results in the following expression

$$\boldsymbol{g(t) = \frac{1}{\sqrt{2\pi}\langle C\rangle} \sqrt{\frac{\pi}{\frac{w_z^2}{4}+D\tau}}} \qquad 2.31$$

By defining the $\frac{w_z}{w_{xy}} = \gamma$ and $\tau_D = \frac{w_{xy}^2}{4D}$,

$$\boldsymbol{g(t) = \frac{\sqrt{2}}{w_z\langle C\rangle} \frac{1}{(1+\frac{1}{\gamma^2}\frac{\tau}{t_D})^{1/2}}} \qquad 2.32$$

Eq. 2.32 represents the final expression, which is inversely proportional to concentration and is used for fitting the autocorrelation plots in one-dimensional space, particularly along the beam propagation direction.

2.2 Raman Scattering Spectroscopy

Raman scattering spectroscopy provides valuable evidence for the molecular structure of a substance. It can also provide information about the chemical composition of mixtures, and the occurrence of interactions between molecules. Raman scattering is the inelastic scattering of photons by a sample. When light is scattered from a polarizable atom or molecule, most photons are elastically scattered at the same energy. This process is called Rayleigh scattering. However, a small fraction of light (~1 in 10^7 photons) is scattered at optical frequencies different from, and usually lower than, the frequency of the incident photons. The photon energy changes in the process. In vibrational Raman scattering, the change in energy is equal to the difference between two vibrational energy-levels of the molecule. If the molecule gains energy in the process this is known as Stokes scattering and the scattered photons of lower energy generate a Stokes line on the red side of the incident light. When the molecules instead lose energy to the photon, the process is known as anti-Stokes scattering, which results in scattered photons that are shifted to the blue side of the incident light, thus generating an anti-Stokes line.

When an incident photon interacts with a molecule, it polarizes the electron cloud of the molecule, creating what is known as a virtual state. The oscillations of the electron cloud then relauches the photon after either capturing some energy from the molecule or transferring some energy to the molecule. As a result, the molecule is left either a lower or higher vibrational state than prior to interacting with the photon. The molecule will typically be left in a higher energy vibrational state, and this generates Stokes Raman scattering. If the molecule is instead left in a lower energy vibrational state, anti-Stokes Raman scattering is produced.

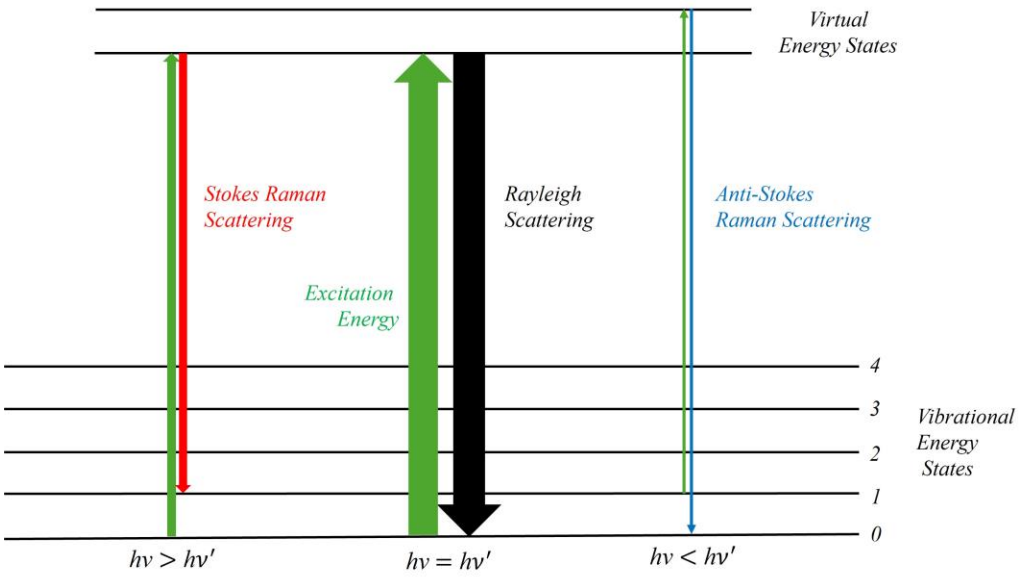

Figure 2.6 Raman scattering diagram showing Stokes, anti-Stokes and Rayleigh Scattering.

The Raman shift represents the difference between the energies of the incident and the scattered photons, as shown in Eq. 2.33.

$$\Delta\bar{\nu}(\boldsymbol{cm^{-1}}) = \left[\frac{\mathbf{1}}{\boldsymbol{\lambda_{in}}} - \frac{\mathbf{1}}{\boldsymbol{\lambda_{scat}}}\right] \times \mathbf{10^7} \qquad 2.33$$

Here, $\Delta\bar{\nu}$ is the Raman shift, while λ_{in} and λ_{scat} represent the wavelengths of the incidence and scattered photons in nanometers.

Raman spectra reported in this dissertation were obtained on a home built inverted confocal microscope that was virtually identical to the microscope used in FCS experiments. The primary difference was that the Raman scattered light collected from the sample was directed into a spectrograph and onto a CCD camera for the recording of Raman spectra in the present case. The configuration for Raman experiments is illustrated in Figure 2.7a. The Raman setup uses the same excitation source and optical path to the oil immersion objective (Nikon Plan Fluor, 100X, 1.3 or 1.49 NA) as in FCS experiments. The objective lens is essential in focusing laser light onto the sample and collecting scattered light with a high numerical aperture (NA).

The high NA (1.3 or 1.49) means that the objective gathers a large fraction of the light scattered by the sample, making it highly effective for Raman scattering experiments, where the signal is inherently weak.

The scattered light is directed through a pinhole located at the microscope's primary image plane. This helps eliminate background in the form of stray light and selectively transmits signal from the focal plane. After passing the pinhole, the light was then directed through a holographic notch filter (Kaiser Optical). A notch filter selectively removes any residual incident laser light while allowing Raman-scattered light to pass through unattenuated. This is critical because the laser used to excite Raman scattering typically overwhelms the weak scattered light. Removing it efficiently ensures that only the Raman signal reaches the detector. Then the Raman-scattered light is directed into an imaging spectrograph (Acton Research, SpectraPro-300i), which is equipped with a 1200 line/mm diffraction grating. The spectrograph disperses the light based on its wavelength, allowing the Raman shifts to be recorded across a spectrum. The 1200 line/mm grating provides a balance between spectral resolution and signal intensity. Higher line density gratings increase the resolution but may also decrease the light throughput. This configuration was found to be optimal for the present experiments. The dispersed Raman signal is detected by a thermoelectrically cooled, electron-multiplying CCD camera (Andor, Newton DU-970P-BV, 1600x200 pixels, 16μm X 16μm pixels). Thermoelectric cooling minimizes thermally-generated dark charges in the detector, which is crucial for detecting low-intensity Raman signals. Two or four-pixel binning was employed along the wavelength axis, while all the vertically illuminated pixels were binned along the axis normal to the spectral dimension to increase the detected signal. Binning along the wavelength axis sacrifices some spectral resolution (which is ~ 2 and 4 cm^{-1} depending on the binning) but enhances the signal strength,

which is useful when working with weak Raman signals. The entrance slit of the spectrograph is typically maintained at a width of 200 μm, which controls the amount of light entering the spectrograph and defines the ultimate spectral resolution. A wider slit allows more light through, improving signal strength, while a narrower slit enhances the spectral resolution but reduces the amount of light.

The wavelength axis of the spectrometer was calibrated using a neon lamp, as shown in Figure 2.7 b,c. Neon lamps are a common reference for wavelength calibration due to their well-known and stable emission lines. Calibration ensures that the recorded Raman shifts correspond accurately to the values expected for each vibrational mode of the molecules being probed, which is critical for identifying components of mixtures or verifying the identity of molecules being detected.

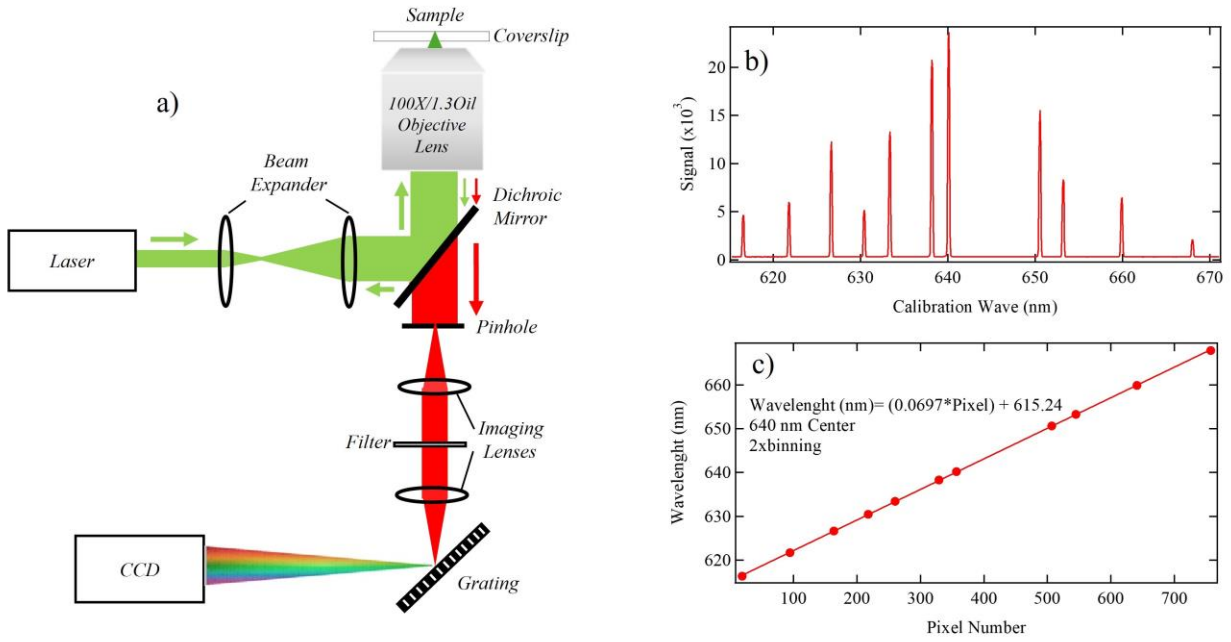

Figure 2.7 a) Optical microscope used to acquire Raman spectra. b) Atomic emission spectra from a Neon lamp acquired on the same microscope. c) Calibration of the spectrometer wavelength from the known peak wavelengths of Neon emission. Red points show the data while the line shows a linear fit.

2.3 Nuclear Magnetic Resonance (NMR) Spectroscopy

Nuclear magnetic resonance (NMR) spectroscopy studies molecules through the interactions of radiofrequency (RF) electromagnetic radiation with the nuclei of molecules in a strong magnetic field. NMR applies only to nuclei with a non-zero nuclear spin quantum number (I), meaning nuclei with I = 0 are 'invisible' to NMR spectroscopy. NMR-active nuclei, particularly those with a spin quantum number 1/2, are significant in NMR spectroscopy such as ^{1}H, ^{13}C, ^{15}N, and ^{31}P.

In the presence of an external magnetic field (B), nuclei with a spin quantum number of 1/2 exhibit two spin states: +1/2 and -1/2. The difference in energy between these two states is directly proportional to the strength of the external magnetic field.

Proton (^{1}H) NMR, a method of paramount importance in organic chemistry, is one of the most widely used NMR methods. The behavior of protons within a molecule varies depending on their chemical environment, allowing for the elucidation of molecular structure. Once the basic structure is known, NMR can be used to determine molecular conformation in solutions and to study a wide range of physical properties at the molecular level, such as conformational exchange, phase changes, solubility, and diffusion. In this dissertation, NMR is used to find the solubility[104] of RhB in the water-ethanol mixture solution. Figure 2.8 provides an example of a proton NMR spectrum acquired for use in this dissertation. This figure specifically displays an NMR spectrum of 12.6 mM rhodamine B in a water-ethanol (20-80 vol%) mixture. The peaks correspond to the different protons within the rhodamine B molecule. The integrated area under each peak is directly proportional the number of protons participating in each resonance. The integrated area under each peak is also proportional to rhodamine B concentration.

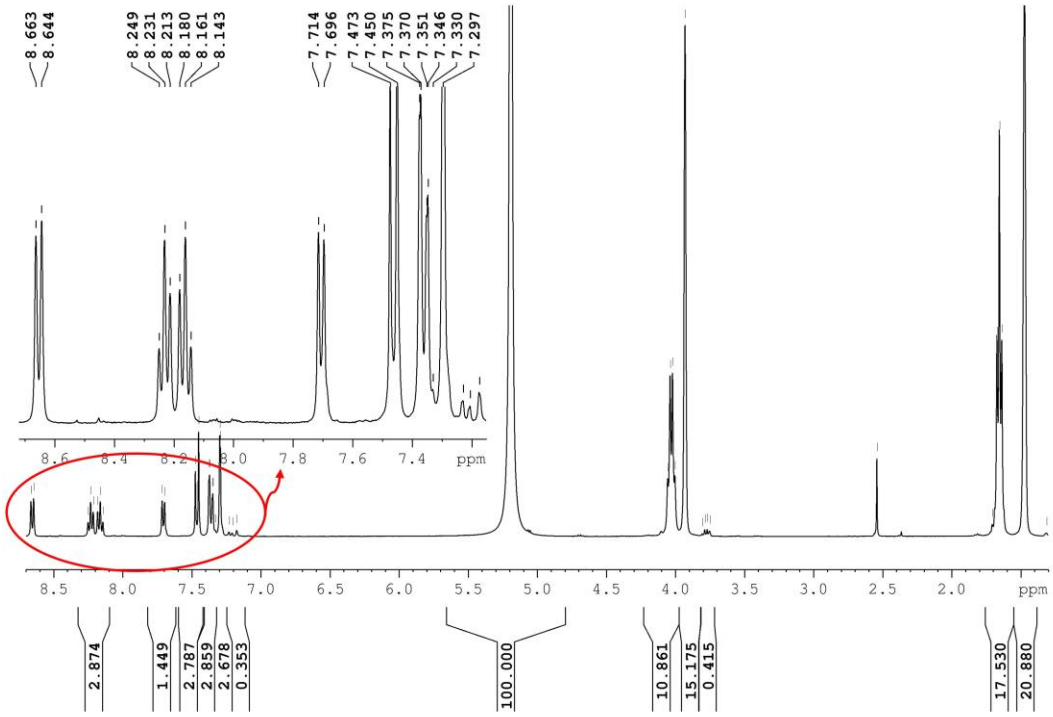

Figure 2.8 NMR spectrum of 12.6 mM rhodamine B in a water-ethanol (20-80 vol%) mixture. The red oval shows the region in which the aromatic protons of rhodamine B appear. The inset shows an enlarged version of this same region to more clearly reveal its spectral features.

Once the basic structure is known, NMR data can be used to determine molecular conformation in solution and to study a wide range of physical properties at the molecular level, such as the rate of conformational exchange, phase changes, solubility, and the rate of diffusion. NMR was employed in this dissertation primarily for determining the solubility of rhodamine B in ethanol-water mixtures. In this case, supersaturated solutions of rhodamine B were prepared in each mixture. Only dissolved rhodamine B contributes to the area under each peak, while solid rhodamine B makes no contribution.

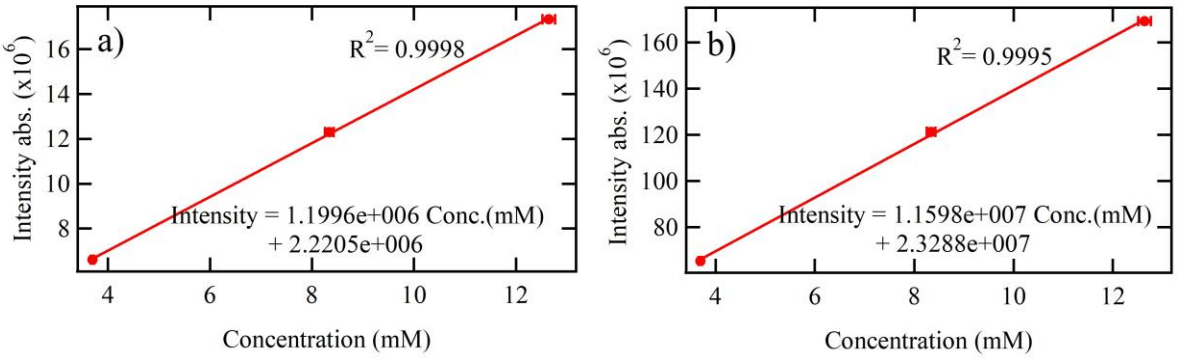

Figure 2.9 Calibration of rhodamine B concentration a) based on the area of the peak at highest chemical shift (8.6 ppm) and b) based on integration of the total peak area for the aromatic protons.

Calibration of the NMR signal was required to quantitatively determine the rhodamine B concentration in each mixture. For this purpose, three known concentrations of rhodamine B in deuterated ethanol and water were prepared for use in the calibration process. The peak area of the aromatic peak at highest chemical shift (8.6 ppm) and the total area for all of the aromatic proton peaks were used in concentration determinations performed in this dissertation. Plots of the calibration data obtained for rhodamine B are shown in Figure 2.9. These curves clearly demonstrate that the expected linear relationship between concentration and integrated peak area is observed, and thus that NMR provides a reliable method for quantifying rhodamine B concentration. Based on these calibration results, the areas under these same aromatic peaks were used to determine the concentration of rhodamine B in samples of unknown concentrations. The results were used to quantify the solubility of rhodamine B in supersaturated solutions of a variety of ethanol-water mixtures (see Chapter 4).

All experiments used a balance with a precision of 0.0001 grams to measure the dye weight and the pure solution before mixing. In this study, changes in volume upon mixing of the pure solvents were not considered. The well-known negative excess molar volume of water and

ethanol mixtures would lead to an increase in rhodamine B solubility of at most approximately 3.5% in intermediate mixtures. Progressively smaller errors occur as the pure solvents are approached.

2.4 Preparation of Anodic Aluminum Oxide (AAO) Membrane

The Nanoporous Anodic Alumina (AAO) membrane is extensively used in various scientific and industrial applications due to its remarkable properties, including a large surface area, high thermal stability, unique optical and electrochemical properties, and customizable characteristics.[105,106]

The structural properties of AAO membranes, such as pore size and thickness, can be finely controlled by adjusting the conditions during its fabrication. The choice of electrolyte, concentrations, applied voltages, and anodization duration are critical parameters in determining these characteristics. Different electrolytes are used to achieve the specific pore sizes; Sulfuric acid is typically employed for small pore sizes (less than 30 nm), oxalic acid for medium pore sizes (30-100 nm), and phosphoric acid for large pore sizes (greater than 100 nm). This flexibility allows the AAO membrane to be customized for particular applications.[107-110]

The fabrication process of nanoporous AAO membrane generally follow a well-stablished two-step anodization method. The process begins with high-purity aluminum foils, which undergo electropolishing using a mixture of ethanol and perchloric acid. This step creates a smooth, defect-free surface on the aluminum, which is crucial for the uniform formation of nanopores.

Next, the first anodization step is carried out under controlled conditions (specific voltage and electrolyte type), during which a porous alumina layer forms on the aluminum surface. This initial layer, however, often contains imperfections and is not ideal for many applications.

Therefore, it is removed through wet chemical etching using a mixture of chromic acid and phosphoric acid. This step eliminates the irregularities and prepares the aluminum surface for a more uniform pore structure during the second anodization.

The second anodization step is performed in the same condition as the first, but it generates a highly ordered and uniform nanoporous structure this time. The resulting membrane is characterized by its ordered pore arrangement and thickness, which are critical for applications requiring precision.

In this dissertation, AAO membranes with pore sizes 10 nm and 20 nm were predominantly used, primarily due to their transparency, which is a critical factor in optical studies. Membranes with smaller pore sizes, like 10 nm, are particularly advantageous in applications requiring high optical clarity, as they exhibit minimal light scattering. The AAO membranes produced using oxalic and phosphoric acid electrolytes often exhibit coloration—yellow for oxalic acid and gray for phosphoric acid. This coloration is due to the incorporation of anions from the electrolyte into the alumina matrix during anodization. Unfortunately, such membranes are unsuitable for optical spectroscopy applications, as the coloration interferes with the transmission and absorption of light, potentially distorting the spectral measurements.

Figure 2.10 (Left and Right) shows the electrolyte side (also referred to as the front side) and barrier side (the back side) the 10 nm, 20 nm and 30 nm AAO membranes. The 30 nm membrane was fabricated through extended etching times compared to the 20 nm membranes, providing an increase in pore size.

All the membranes used in this dissertation were commercially purchased from InRedox Company.

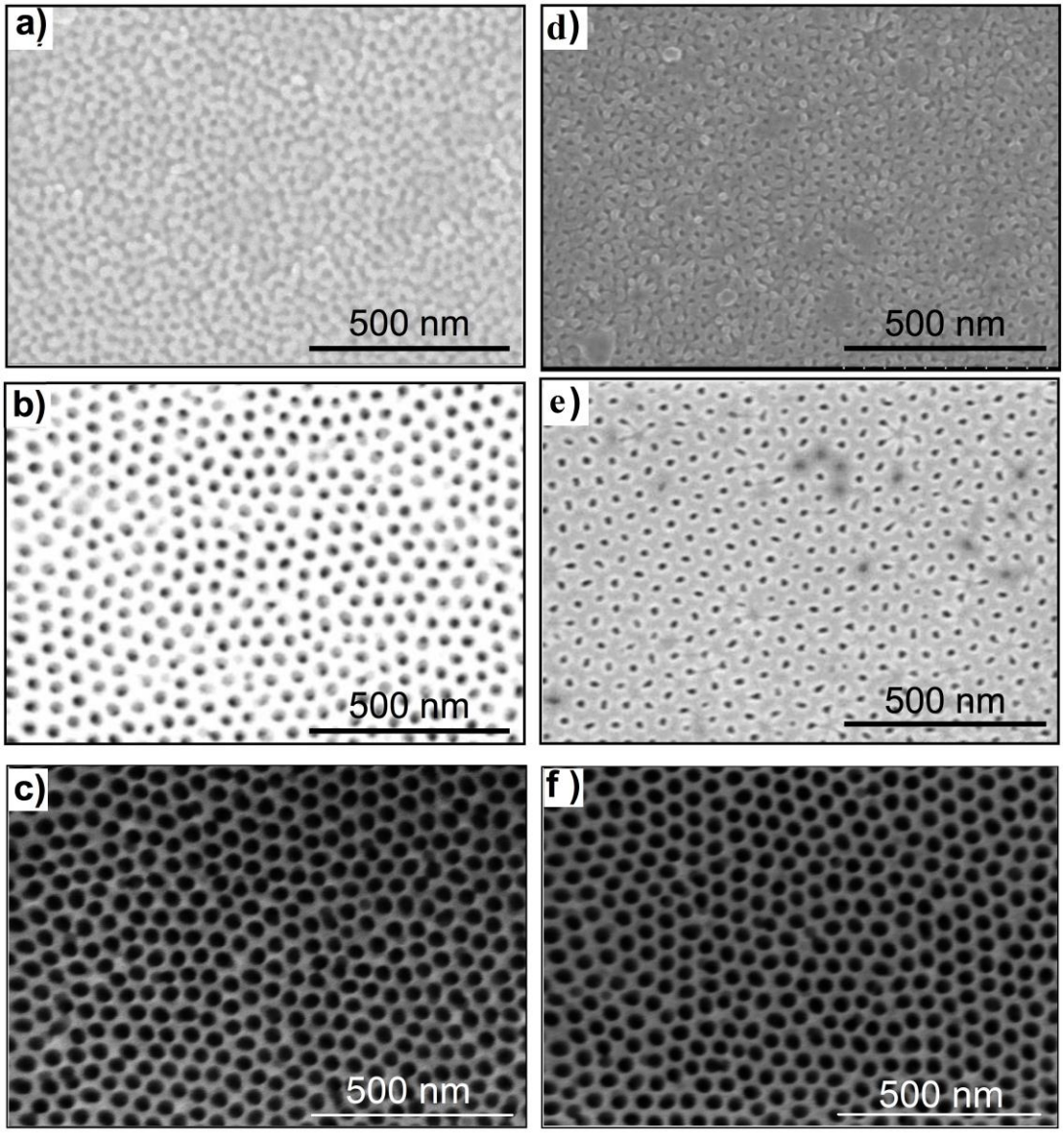

Figure 2.10 Scanning electron microscopy (SEM) images. a), b) and c) representative AAO membranes having 10 nm, 20 nm, and 30 nm nanopores, respectively. The face shown is the face probed in optical experiments. d), e) and f) SEM images of the opposite faces of the same membranes shown on the left side. All the images were taken by Dr. Takashi Ito at the Argonne National Lab.

Chapter 3 - Random Walks and Sticky Surfaces: Single Molecule Measurements of Solute Diffusion in Ethanol/Water-Filled Anodic Alumina Nanopores

Adapted with permission from: Rashidi, H.; Howard, K. J.; Ito, T.; Higgins, D. A. *J. Phys. Chem. C* **2023**, *127*, 411-420, Copyright 2023 American Chemical Society. (https://doi.org/10.1021/acs.jpcc.2c07083),

3.1 Introduction

Nanoporous anodic aluminum oxide (AAO) membranes are now being explored for use in a variety of applications including in catalysis, drug delivery, chemical and biological sensing, and chemical separations.[105,106] While their commercial availability makes them useful in many routine separations, AAO membranes also find emerging applications in the dehydration of renewable biofuels such as ethanol,[40] where they may afford new routes to the breaking of azeotropes. The optimization of membrane performance for a given separation can be particularly challenging when chemically complex mixtures are involved. These challenges are compounded by the fact that many chemicals behave differently under nanoconfinement than in the bulk. For example, the freezing and melting points of many solvents change upon confinement.[34] In addition, the orientational[56,111] and translational[56,57] motions of confined molecules may be substantially slower. They may also exhibit different chemical equilibrium behaviors,[112] and mixtures may phase separate.[38,113,114] Nanoconfinement is also certain to cause

changes in the chemical and physical properties of solutes.[35] Frequent interactions of solute molecules with the pore walls and/or with surface-associated solvent layers may influence their adsorption and desorption energetics and dynamics, altering the rate at which they diffuse within the pores.[36] Once completely understood, the development of new means to control these phenomena will afford routes to chemical separations of enhanced efficiency and/or selectivity.

Exploring the complexities of mass transport phenomena in solvent mixtures confined within AAO nanopores requires the use of experimental tools that directly probe solvent and/or solute motions. Methods that afford such information include pulsed-field-gradient NMR spectroscopy,[55] electron spin resonance spectroscopy,[112] and quasi-elastic neutron scattering.[56,57] A variety of optical spectroscopic and imaging methods can also be used to explore molecular diffusion within nanoporous materials. These include direct fluorescence imaging,[115] fluorescence anisotropy measurements,[58] fluorescence recovery after photobleaching,[58-61] and optical Kerr effect spectroscopy.[111] While all these tools provide important data at the ensemble level and have resulted in improved understanding of mass transport under nanoconfinement, none allow for individual molecular-level events to be directly observed and characterized. As a result, they likely mask many of the relevant details needed to fully understand the mechanisms of diffusion in confined environments.

Optical microscopic methods that directly record single molecule transit events have provided access to new knowledge on mass transport mechanisms in nanoporous materials.[116] Our research groups,[62,117] and others[118-121] have employed wide-field fluorescence video microscopy and single molecule detection and tracking to examine the diffusion of dyes within solvent- and surfactant-filled mesoporous silica. Similar methods have also been applied in recent studies of diffusion within AAO membranes, [69,70,122] and in other nanoporous materials.

[116,123-,125] The results of previous studies have revealed the importance of solvent nanostructuring in governing molecular dynamics within the pores,[75] and have highlighted the roles played by surface interactions,[76] partitioning,[77] and orientational confinement[75] of the probe molecules.

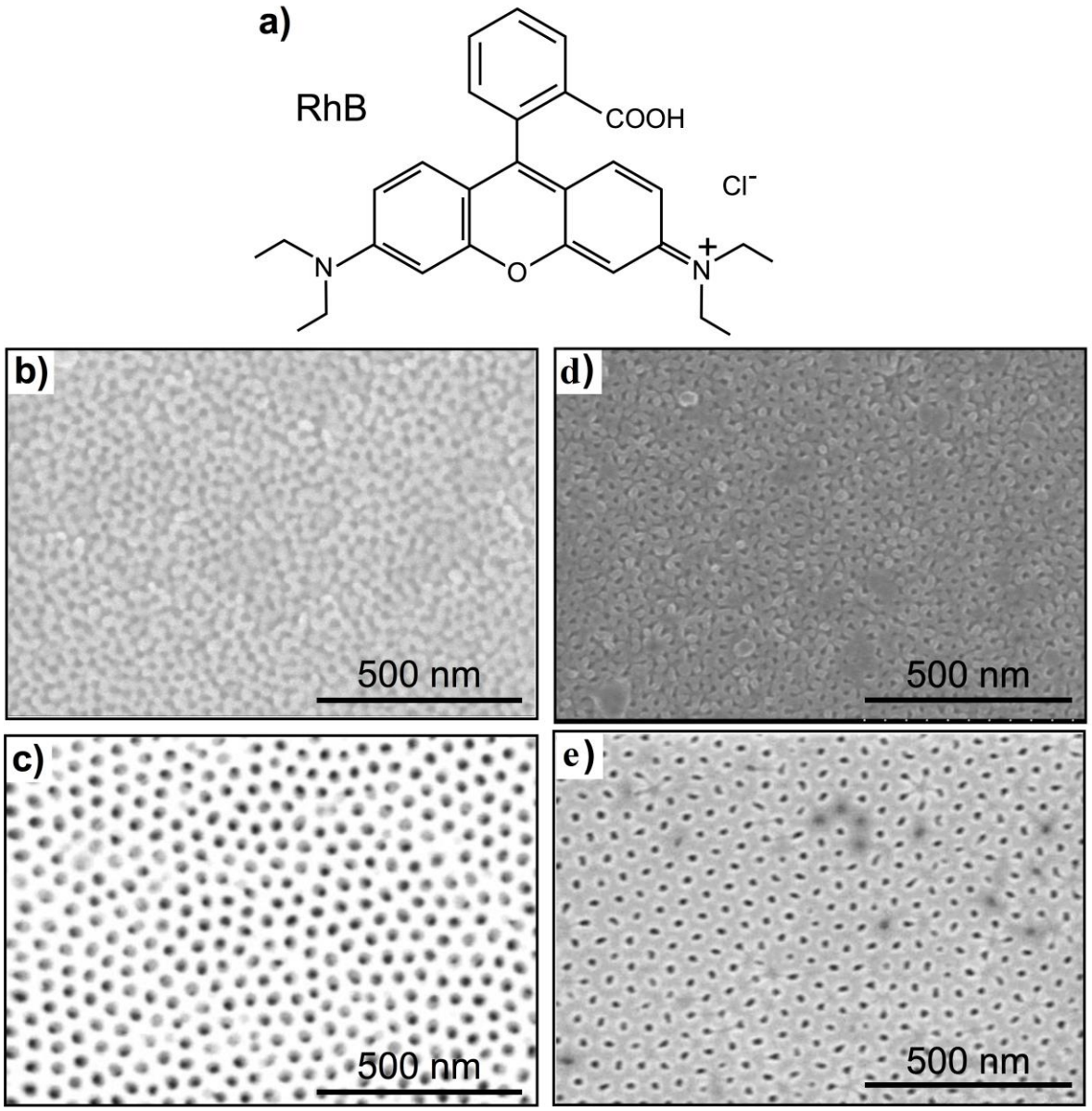

Figure 3.1 a) Chemical structure of Rhodamine B. b) and c) scanning electron microscopy (SEM) images of representative AAO membranes having 10 nm and 20 nm nanopores, respectively. The face shown is the face probed in optical experiments. d) and e) SEM images of the opposite faces of same membranes shown in b and c. The SEM images were taken by Dr. Takashi Ito at the Argonne National Lab.

In this chapter, we employ single molecule detection and fluorescence correlation spectroscopy (FCS)[71] to investigate the mass transport dynamics of rhodamine B (RhB) dye (see Figure 3.1a) confined within the vertically-oriented nanopores of solvent-filled AAO membranes. The commercial AAO membranes employed incorporate uniformly sized 10 nm and 20 nm diameter nanopores that pass completely through the 50 μm thick membranes (see Figure 3.1b, c).

The solutions explored range in composition from pure ethanol to 33% (by volume) water and ethanol mixtures. Fluorescence time transients acquired on a confocal microscope were used to detect the translational motions of individual RhB molecules at a depth of 5 μm within the membranes (see Figure 3.2). The time transient data reveal fluorescence fluctuations attributable to the one-dimensional (1D) diffusion of RhB along the pore axis. These same data are used to investigate interactions occurring between the dye and the pore surfaces. Autocorrelations of the time transient data allow for assignment of RhB diffusion mechanisms and the quantitative determination of their diffusion coefficients as a function of ethanol/water mixture composition. The results of these studies provide an improved understanding of the mass transport mechanisms and dynamics of solutes dissolved within nanoconfined solvent mixtures and will facilitate development of new nanoporous materials for more efficient and more selective chemical separations.

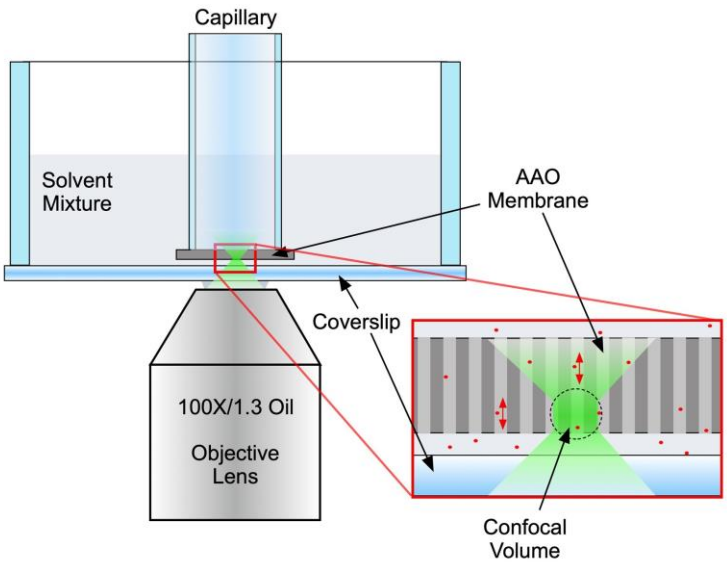

Figure 3.2 Experimental setup employed in FCS experiments and for recording time transient data. An expanded view of the AAO membrane and the confocal volume (not to scale) are shown at the lower right. The red circles represent single RhB molecules.

3.2 Methods

3.2.1 Materials

Rhodamine B (RhB) was obtained from Sigma-Aldrich and was used as received. Figure 3.1a shows its chemical structure. The concentration of RhB was maintained at 2 nM in all FCS experiments. Its emission spectra in bulk solutions of different compositions are shown in Figure 3.3. These reveal a gradual shift of only a few nanometers (~ 10 nm) in its peak emission wavelength over the full range of mixtures examined, demonstrating negligible solvatochromism.

High purity water was obtained from Fisher Scientific (HPLC grade), while pure ethanol was obtained from Sigma-Aldrich (HPLC grade). Both were used as received. These experiments were performed using RhB-doped ethanol and mixtures of 2%, 5%, 10% and 33% (by volume) water and ethanol.

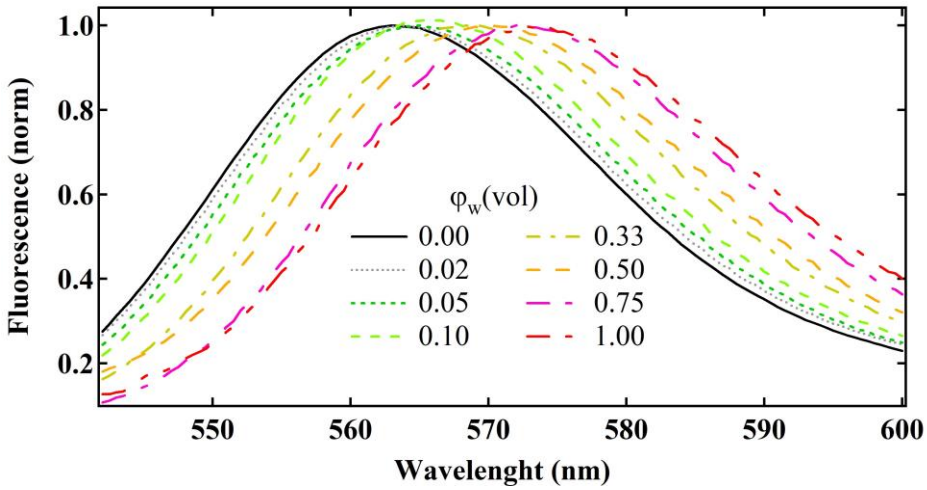

Figure 3.3 RhB fluorescence spectra as a function of volume fraction of water, φ_w, in ethanol-water mixtures. Fluorescence was excited at 532 nm. The results reveal only minor solvatochromism**.**

Nanoporous anodic aluminum oxide (AAO) membranes were purchased from InRedox, LLC. They were obtained as 10 mm diameter disks and incorporate cylindrical 10 nm and 20 nm diameter pores that extend across the full 50 μm membrane thickness. The porosities of the 10 nm and 20 nm membranes are quoted by the manufacturer to be 12±2% in both cases, with 1.6×10^{11} pores/cm^2 and 5.8×10^{10} pores/cm^2, respectively. The membranes were frequently cut into smaller pieces prior to use. Scanning electron microscopy (SEM) images of the AAO membranes are shown in Figure 3.1b-e. The former (b and c) shows images of the membrane face at which all optical measurements were made, while the latter (d and e) shows images of the back face. To ensure the pores were filled with solvent, each membrane was first immersed in pure ethanol and placed under reduced pressure using an oil-free vacuum pump (KNF Lab Filtration Pump) for 60-90 min. The membranes were subsequently maintained under ethanol for at least one day prior to use. At the start of each experiment, the membranes were transferred to an optical cell (described below) for mounting on the microscope and were immediately immersed in one of the RhB-doped solutions. They were maintained under this solution for a

period of 30 min prior to the start of each experiment. Whenever the solution composition was changed, a period of 30 min was allowed for equilibration of the membrane with the new solution before the next experiment was performed. Raman spectra provided conclusive evidence that the solution within the pores was fully exchanged on this time scale.

3.2.2 Measurements

SEM images were acquired on a Hitachi S-4700-II SEM at the Center for Nanoscale Materials, Argonne National Laboratory. High-resolution images were acquired at 10 kV under 100,000X magnification. The membranes were coated with a thin layer of carbon for SEM imaging experiments.

Raman spectra of pure solvents and solvent mixtures (in the absence of dye) were acquired from both bulk solutions and from environments within the AAO membranes. These were obtained on a confocal microscope that was constructed in-house using a commercial inverted light microscope (Nikon TE-200). The microscope focus was positioned 5 μm below the AAO membrane to obtain bulk solution spectra and 5 μm above the membrane/solution interface (i.e., within the membrane) to collect spectra from solvents confined within the membrane nanopores. The scattered light collected by the oil immersion objective (Nikon Plan Fluor, 100X, 1.3 NA) was directed through a 100 μm diameter pinhole located in the primary image plane of the microscope and was then sent into an imaging spectrograph (Acton Research, SpectraPro-300i). The spectrograph incorporated a 1200 line/mm diffraction grating and Raman scattering was detected using a thermoelectrically cooled, electron-multiplying CCD camera (Andor, Newton DU-970P-BV, 1600x200 pixels, 16μm X 16μm pixels). Two-pixel binning was employed in the spectral dimension, giving a resolution of ~ 2 cm^{-1}. The entrance slit of the spectrograph was typically maintained at a width of 150 μm. The wavelength axis of the

spectrometer was calibrated using a neon lamp. An incident laser power (532 nm) of 5 mW was employed in all Raman experiments. The signal was integrated for a period of 10 s in each case and 50 replicate spectra were averaged together to obtain the final spectrum.

Single molecule detection and fluorescence correlation spectroscopy (FCS) experiments were performed on another confocal microscope that was constructed in-house using a commercial inverted light microscope (Nikon TE-200) and virtually identical to those used for confocal Raman spectroscopy. An oil immersion objective (Nikon Plan Fluor, 100X, 1.3 NA) was employed for illumination of the sample and for collection of RhB fluorescence. Fluorescence was excited by 532 nm light from a diode-pumped solid state Nd:YVO_4 laser (Coherent Verdi-5W). The incident laser beam was reflected from a dichroic beam splitter (Chroma 550 DCLP) into the back aperture of the objective lens. The beam was sized to slightly overfill the objective aperture to ensure the smallest possible diffraction-limited focus in the sample. Its $1/e^2$ diameter at the focus was determined to be ~ 520 nm. An incident power of 10 μW, measured prior to incidence on the dichroic beam splitter, was used in all experiments. This power was chosen to provide high signal-to-noise data while also avoiding rapid photobleaching of the dye.

Fluorescence collected from the sample was directed back through the dichroic beam splitter and into the detection path of the microscope. The tube lens within the microscope focused the fluorescence through a 50 μm diameter pinhole positioned in its primary image plane. The use of confocal methods allowed for selective detection of fluorescence from either bulk solution or within the AAO membrane. The light emerging from the pinhole was collected by a telescope constructed from two achromatic lenses. It was subsequently sent through a bandpass filter (Chroma, 580/40m) and then focused onto the photosensitive element of a single-

photon-counting avalanche photodiode (APD, Perkin Elmer SPCM-AQ-141R). The electrical pulses output by the APD were counted using a National Instruments counter/timer board (PCIe-6612)[126] operated in the time-stamping mode. A 25 MHz clock was employed as the timer. Time-stamping data were recorded using a National Instruments Labview program written in house. The data were autocorrelated and analyzed using C++ code and Igor Pro (Wavemetrics) macros that were also written in house.

The detection area in the microscope was regularly and carefully recalibrated by measurement of RhB diffusion in water or ethanol. The RhB diffusion coefficient in water has been reported to be 430 $\mu m^2/s$, [102,103] while its value in ethanol was determined to be 336 $\mu m^2/s$ in these studies. Calibration was performed using solution-phase data that were acquired 5 μm below the AAO membrane surface.

The AAO membranes were mounted in a custom-made solution cell for all optical measurements, as shown in Figure 3.2. The solution cell comprised a 14 mm diameter glass tube that was attached to a microscope coverslip (FisherFinest, Premium) using either glass super glue or parafilm. The coverslip formed a transparent window into the cell. The optical cell was positioned on a 1.25 cm thick aluminum mounting plate that was attached to the microscope base. The mounting plate ensured the microscope focus was stable over long periods of time (> 30 min). The AAO membrane nanopores were oriented vertically (see Figure 3.2, expanded view) with the cylindrical pore axis running parallel to the optical path of the laser.

At the start of each experiment, the AAO membrane was placed in the solution cell and immediately immersed under the selected RhB-doped (2 nM) solution. A glass capillary mounted vertically to a three-dimensional micrometer stage was used to press the AAO membrane down into close proximity to the coverslip surface. This allowed for the membrane-

coverslip distance to be reproducibly maintained to within ~ 20 μm, minimizing variations in the confocal detection area caused by spherical aberrations when focusing at different depths in media of different refractive indexes.[95,101,127] For bulk solution measurements, the microscope focus was positioned in solution, 5 μm below the AAO membrane. For measurements of RhB diffusion within the AAO membrane nanopores, the focus was positioned 5 μm inside the membrane (i.e., above its lower surface).

3.3 Results

3.3.1 Fluorescence Time Transients: Initial Observations

Diffusion of RhB molecules in bulk solution and confined within solvent-filled AAO nanopores was initially explored by acquiring fluorescence time transients from each of these environments. Figure 3.2 shows the experimental setup employed. The diffusion of individual dye molecules through the microscope focus (Figure 3.2, lower right) produces a short burst of fluorescence for each transit event. Representative time transients obtained from RhB-doped bulk ethanol and from RhB-doped ethanol confined within 10 nm and 20 nm AAO nanopores are shown in Figure 3.4. Fluorescence bursts are readily observed in all three sets of data. However, the fluorescence fluctuations due to RhB diffusion in bulk solution (Figure 3.4a) are largely too fast to observe using 1 ms bin times. In contrast, the fluorescence bursts detected from within the AAO membranes are more obvious, occur less frequently, and are longer in duration, consistent with slower RhB diffusion in the 1D nanopores.

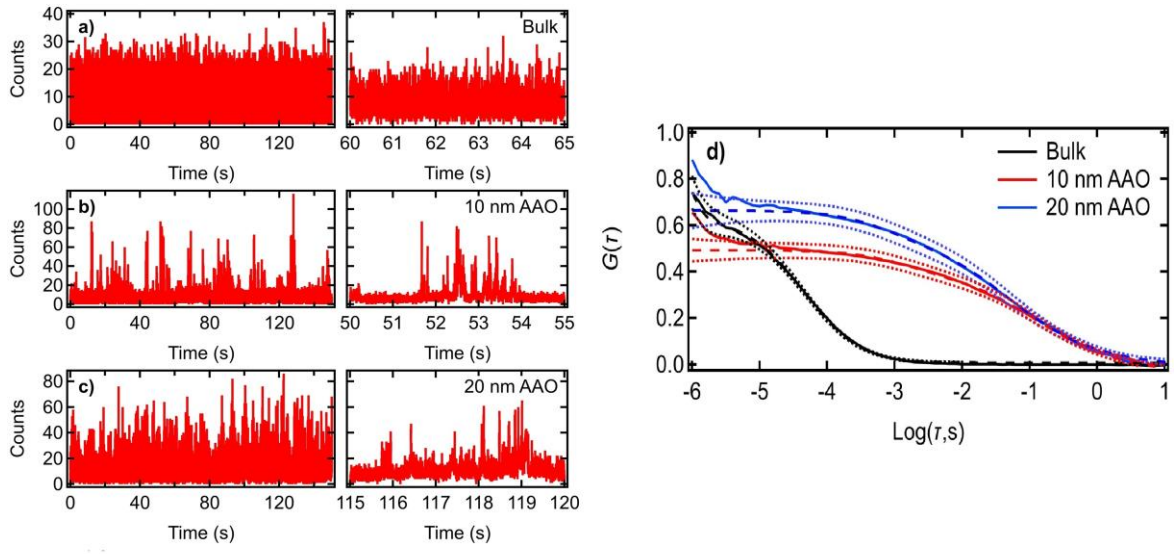

Figure 3.4 Representative time transients for 2 nM RhB in a) bulk ethanol solution, b) ethanol-filled 10 nm AAO nanopores, and c) ethanol-filled 20 nm AAO nanopores. Expanded segments from each transient are shown in the right column of plots. All time transients are displayed with 1 ms bin times. d) Autocorrelation data (solid lines) obtained from the same series of samples. These data depict averages from multiple (9-10) replicate measurements. The dashed lines in d) depict fit the data to Eqs. 3.2 and 3.3 for bulk solution and nanopore environments, respectively. The dotted lines on either side of the fits depict the 95% confidence intervals, as determined from the 9-10 replicates. The AAO autocorrelations were fit from 10^{-4} s to 3 s while the bulk solution data were fit from 10^{-6} s to 10^{-2} s.

Expanded segments of each transient are given in the right column of Figure 3.4a-c. These data show that the fluorescence bursts from within the AAO nanopores are separated by periods of background counts, consistent with passage of individual RhB molecules through the detection region. The fluorescence bursts shown in Figure 3.4 vary in intensity owing to several factors, including the different lengths of time each molecule spends in the detection volume due to its random motions, the non-uniform excitation intensity across the confocal volume, and random variations in the number of molecules present in the detection volume.

The direct visualization of fluorescence bursts from single-molecule transit events is critically important to a full understanding of the dye diffusion mechanisms in this study.[128] Such information cannot be obtained by ensemble-based FCS methods alone. The fluorescence

bursts shown in the expanded segments in Figure 3.4b, c (right column) span a broad range of time scales and suggest that the mechanism for dye diffusion within the solvent-filled nanopores is relatively complex. The origins and impacts of this complexity are addressed further, below.

3.3.2 Autocorrelation Data and Fitting Models

Autocorrelation decays derived from the fluorescence time transients provide quantitative data on the mean rate of dye diffusion, while also providing evidence of the diffusion mechanism. All time transients were autocorrelated as given in Eq. 3.1.

$$\boldsymbol{G(\tau) = \frac{\langle I(t) I(t+\tau)\rangle}{\langle I(t)\rangle^2} - 1} \qquad 3.1$$

Here, $I(t)$ represents the time transient and $I(t + \tau)$ is a copy that has been shifted by time τ. The angular brackets indicate that the average value is calculated over t. In these studies, the autocorrelation data were further averaged across several (i.e. ~ 10) replicate data sets from the same sample region to achieve additional improvements in the signal-to-noise ratio. Representative autocorrelation decays from bulk solution and within the AAO nanopores are plotted in Figure 3.4d.

The autocorrelation functions were fitted to equations that model the expected diffusion mode in each case. For example, the bulk solution data are expected to reflect free 3D diffusion of the dye. The fitting equation employed is given as Eq. 3.2.[100] The quality of the fit provides evidence of whether or not the correct model (i.e., diffusion mechanism) has been chosen.

$$\boldsymbol{G(\tau) = A_o + \frac{1}{N}\left[A_b \left(1 + \left(\frac{\tau}{\tau_{D_b}}\right)\right)^{-1} \left(1 + \left(\frac{\tau}{\tau_{D_b}}\right)\left(\frac{1}{\gamma^2}\right)\right)^{-1/2} \left(1 + A_r e^{-k\tau}\right)\right]} \qquad 3.2$$

In Eq. 3.2, A_o is a constant (≈ 0), N is the average number of molecules in the detection region, and A_b is the fractional contribution of free 3D diffusion to the autocorrelation decay. A_r and k are the fractional amplitude and rate constant, respectively, for contributions from faster

fluctuations that were too fast (see Figure 3.4d, black curve, near ~ 10^{-6} s) to result from dye diffusion. These fluctuations may arise instead from quantum mechanical blinking of the dye.[129] The latter are of no interest in the present studies, but the extra term has been included to ensure accurate parameters are obtained for dye diffusion. The average residence time of individual RhB molecules in the detection region is given by τ_{D_b}, while $\gamma = w_z/w_r \approx 4$,[101] where w_z and w_r are, respectively, the experimentally determined axial and radial dimensions of the detection region. τ_{D_b} is related to the diffusion coefficient of the dye in bulk solution, D_b, by $\tau_{D_b} = w_r^2/4D_b$. The known value of D_b for RhB in aqueous solution (430 μm^2/s[102,103]) was employed to determine w_r (and w_z) from the measured value of τ_{D_b}. These values were regularly recalibrated and were found to vary by < 6.5% relative standard deviation.

Figure 3.4d (black dashed curve) shows a fit of the bulk ethanol data to Eq. 3.2, revealing that the model fits the data very well. Figure 3.4d includes error bars showing that the fit falls well within the 95% confidence interval. All bulk solution data were fit between 10^{-6} s and 10^{-2} s, encompassing both fast and slow signal fluctuations. Again, the fastest fluctuations (~ 10^{-6} s) are neglected in these studies. The autocorrelation results from the slower fluctuations occurring on a ~ 10^{-4} s time scale yielded D_b = 336 ± 2 μm^2/s for RhB in ethanol. Figure 3.5a represents the D_b values for RhB across a whole range of water/ethanol mixtures measured by FCS, as mentioned. Applying the Stokes-Einstein equation on the diffusion coefficients on the bulk water/ethanol mixtures, the viscosity of each mixture was calculated, and it's a good agreement with the reported value in the literature,[130] which is shown in Figure 3.5b.

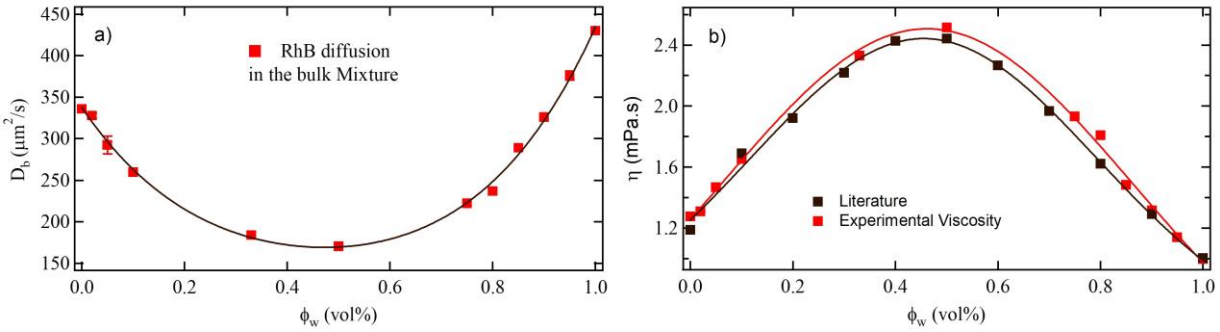

Figure 3.5 a) The bulk diffusion coefficient, D_b, for RhB measured by FCS as a function of water fraction in a series of ethanol/water mixtures. b) Solution viscosity estimated from the data in a) using the Stokes-Einstein equation (red squares) and solution viscosity obtained from the literature.[130] The solid lines were added to better highlight the trends in each data set. The molecular radius for RhB (0.52 nm) was determined by adjusting its value in the Stokes-Einstein equation to minimize the sum of the squared errors between the literature data and the values determined in the present experiments.

RhB is expected to exhibit 1D diffusion within the AAO membranes, yielding slower autocorrelation decays. The decays obtained from the 10 nm and 20 nm nanopores (see Figure 3.4d, blue and red curves) were slower as expected, but were also too broad to arise from 1D diffusion by a single mechanism alone. Instead, autocorrelation data acquired from within the nanopores were found to fit best to a model incorporating two different 1D diffusion modes. The two components are characterized here as fast and slow 1D diffusion. Eq. 3.3 provides the exact expression used to fit these autocorrelation decays. The two terms in the square brackets model diffusion in 1D for the two separate components. Derivation of Eq. 3.3 follows the original work of Elson and Magde,[71] but for the case of 1D diffusion. An appropriate change in the z-boundary condition is also required; in this case, the concentration fluctuations go to zero at infinite distance. The single-component analog of Eq. 3.3 has already been widely employed in the literature to model 1D diffusion.[62,69,70] The justification for inclusion of a second component is similar to that of a previous FCS study of 2D diffusion by dye-labeled proteins in 50 nm deep microfluidic channels, as described below.[36]

$$G(\tau) \approx A_o + \frac{1}{N}\left[\left(A_f\left(1+\left(\frac{\tau}{\tau_{D_f}}\right)\left(\frac{1}{\gamma^2}\right)\right)^{-1/2} + A_s\left(1+\left(\frac{\tau}{\tau_{D_s}}\right)\left(\frac{1}{\gamma^2}\right)\right)^{-1/2}\right)\right] \qquad 3.3$$

In Eq. 3.3, A_o is a constant (≈ 0), N is again the average number of molecules in the detection region, A_f and A_s represent the fractional contributions of fast and slow diffusion to each autocorrelation decay, τ_{D_f} and τ_{D_s} are the average residence times of the molecules in the detection region for molecules exhibiting fast and slow diffusion, and $\gamma = w_z/w_r \approx 4$, as described above. Note that γ is obtained from the radial (w_r) and axial (w_z) dimensions of the microscope focal volume alone and, besides its dependence on refractive index of the material (see Methods), does not depend upon the physical structure (i.e. pore size) of the anodic alumina membrane. The use of a 1D diffusion model in Eq. 3.4 is justified by the size of the pores (10 nm and 20 nm diameters, 50 μm length) relative to $w_r \approx 250$ nm, and $w_z \approx 1$ μm. Dye motions in the radial dimension (x,y) make negligible contributions to the observed fluorescence fluctuations, which are instead dominated by 1D dye motion along z.

Figure 3.4d shows fits of the autocorrelation data from ethanol-filled 10 nm and 20 nm AAO nanopores to Eq. 3.3 (dashed curves) and their 95% confidence intervals (dotted curves). In this case, the data were fit between 10^{-4} s and 3 s. While the fastest fluctuations ($\sim 10^{-6}$ s) observed in bulk solution were also present in these data, their contributions have been left out of the model. The approximation in Eq. 3.3 is valid because the fastest fluctuations are orders of magnitude faster than those produced by 1D dye diffusion.

The data plotted in Figure 3.4d yield D_f and D_s values of 172 ± 25 μm^2/s and 3.3 ± 0.2 μm^2/s, respectively, for RhB in the 10 nm nanopores, while values of 237 ± 22 μm^2/s and 5.1 ± 0.3 μm^2/s were obtained from the 20 nm nanopores. The D_f values are approximately two-fold smaller than D_b in bulk ethanol. In contrast, the D_s values are about two orders of magnitude

smaller than D_b. These results provide clear evidence that fast and slow RhB diffusion within the solvent-filled AAO nanopores are moderately and strongly hindered, respectively, with respect to bulk diffusion.

3.3.3 Solvent Composition and Pore Size Dependence

The origins of the two RhB diffusion mechanisms and their impacts on dye diffusion dynamics were further explored by acquiring data from several different membranes filled with RhB-doped ethanol or 2%, 5%, 10%, or 33% (by volume) mixtures of water and ethanol. In each case, FCS data were collected from the nanopores and from bulk solution just below the membranes. A total of 10-12 independent experiments were performed on each sample for each of the five solvent compositions. All data were analyzed as described above.

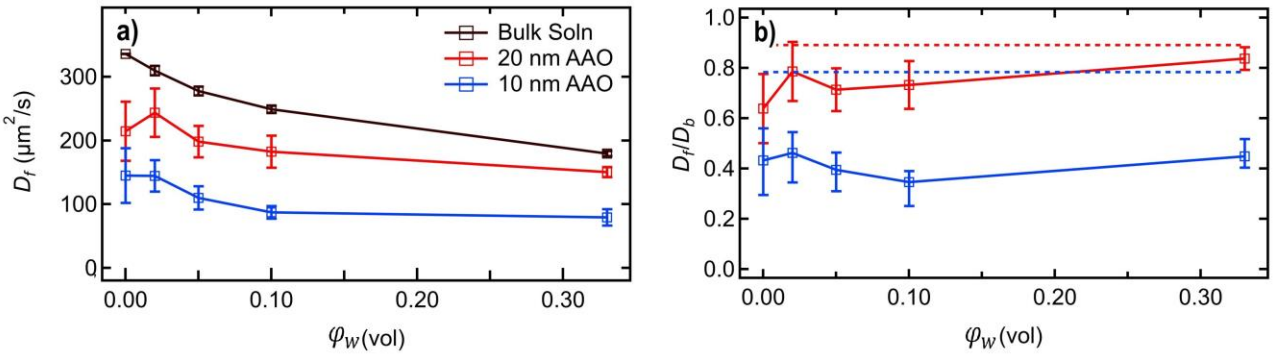

Figure 3.6 Mean values of D_b and D_f for RhB diffusion in bulk solution and in 10 nm and 20 nm AAO nanopores (symbols) as a function of the volume fraction water, φ_w, in the mixture. b) Ratio of the fast and bulk diffusion coefficients for RhB, D_f/D_b, in the nanopores as a function of φ_w (symbols) and predicted ratios (dashed lines) from a model for hydrodynamic drag (Eq. 3.4). The error bars show the 95% confidence intervals of each value from 10-12 replicate measurements.

Figure 3.6a plots mean D_b values (black data points) from bulk solution along with mean D_f values from within the 10 nm (blue data points) and 20 nm (red data points) nanopores as a function of the volume fraction of water, φ_w, in the solvent mixture. As noted above, the D_f

values were moderately smaller than D_b in all cases. Figure 3.6b provides plots of D_f/D_b to better depict the trends. The 10 nm AAO nanopores yielded the smallest D_f values, with somewhat larger values obtained from the 20 nm pores, revealing a clear pore-size dependence to the rate of fast diffusion, even though the pore diameter is at least an order of magnitude larger than the dye itself. These results provide strong support for the conclusion that fast RhB diffusion is moderately hindered within the solvent-filled nanopores.

The D_f data for both 10 nm and 20 nm pores also show clear trends with solvent composition. These closely mimic the composition dependence of D_b (see Figure 3.6a) suggesting that fast RhB diffusion within the nanopores occurs by a bulk-like Brownian mechanism. However, the residual dependence on solvent composition shown in the D_f/D_b plots of Figure 3.6b indicates that the diffusion mechanism is actually somewhat more complicated.

Figure 3.7a plots mean D_s values as a function of φ_w for RhB in the AAO membranes. As with D_f, the D_s values are also pore size dependent, with smaller values obtained from the 10 nm nanopores and larger values from the 20 nm pores. The plots of D_s/D_b shown in Figure 3.7b demonstrate that the D_s values are a small fraction of D_b across the full range of conditions investigated, providing additional evidence that slow RhB diffusion is strongly hindered within the nanopores. Interestingly, the plots of D_s and D_s/D_b exhibit distinctly different dependences on solvent composition than the corresponding plots for D_f (see Figure 3.6). Namely, the D_s values increased monotonically with φ_w, while the D_f values mostly decreased.

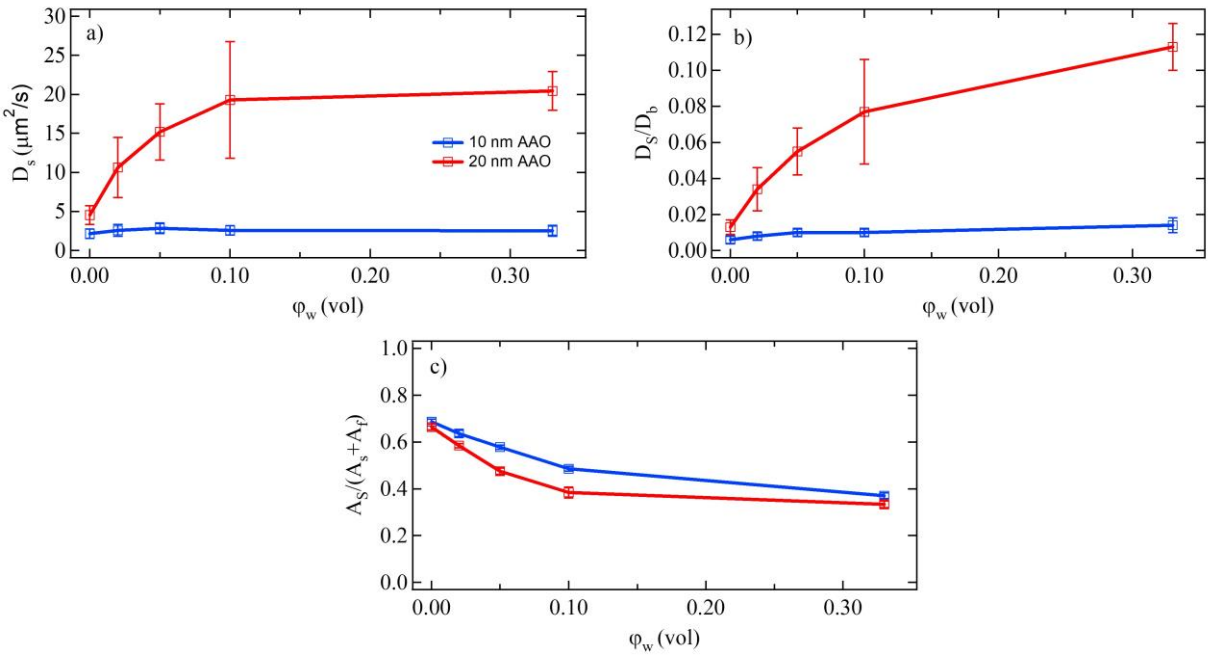

Figure 3.7 a) Slow diffusion component, D_s, for RhB in 10 nm and 20 nm AAO nanopores as a function of φ_w in the mixture. b) Ratio of the slow and bulk diffusion coefficients for RhB, D_s/D_b, in the nanopores as a function of φ_w. c) Relative amplitude of the slow component of the autocorrelation decays as a function of φ_w. The error bars show the 95% confidence intervals of each value from 10-12 replicate measurements.

Figure 3.7c plots the mean relative amplitude, $A_s/(A_s + A_f)$, of the slow RhB diffusion component. These results reveal that slow dye diffusion is somewhat more common in the 10 nm nanopores than in the 20 nm pores and that it also becomes less common with increasing φ_w in the nanoconfined solvent mixtures. These observations are distinctly different from what is expected for simple Brownian motion in 1D.

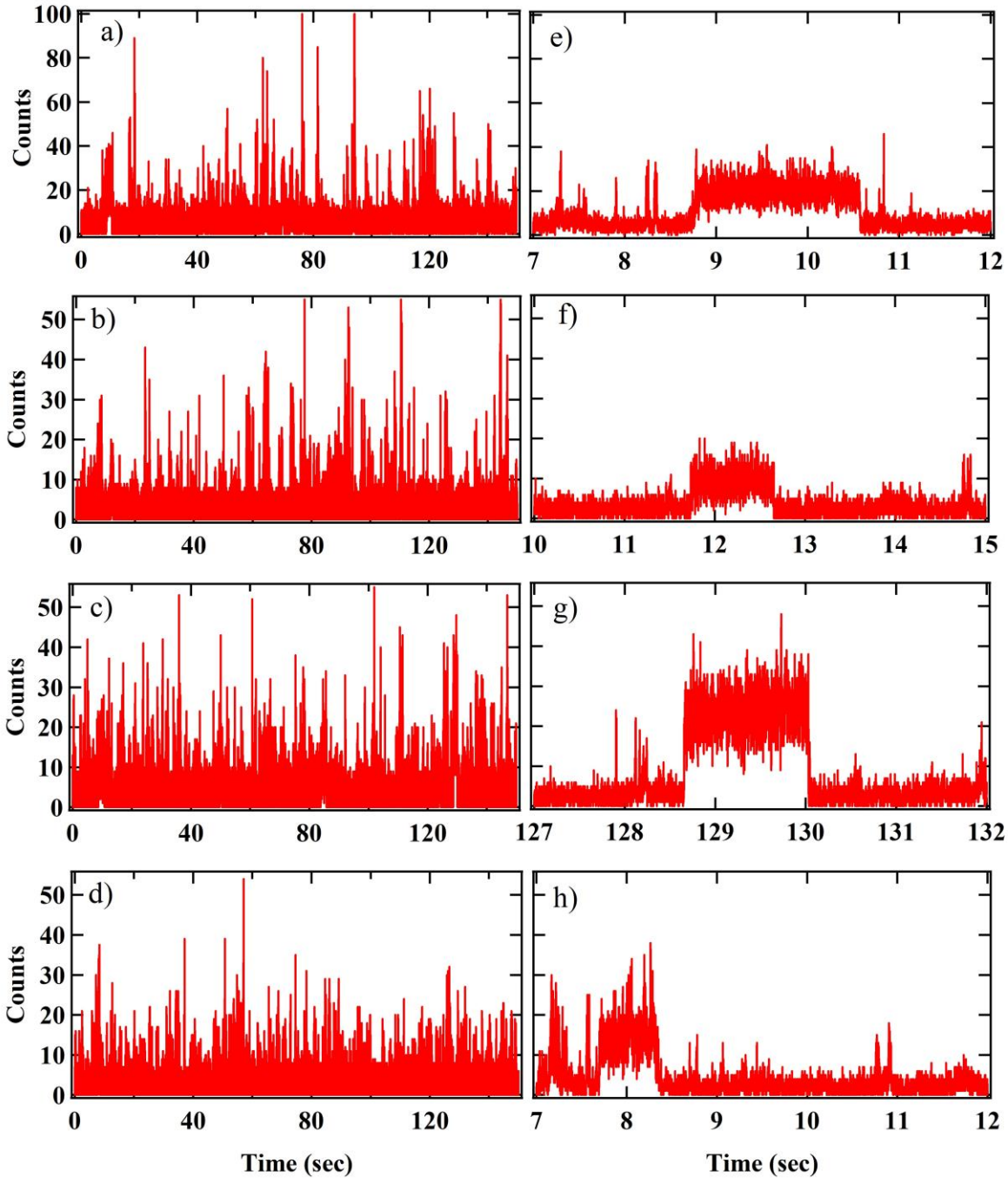

Figure 3.8 Representative time transients showing some of the longest burst events observed, which are attributed to RhB adsorption on the AAO nanopore surface. Data are shown for a) 10 nm AAO membrane in pure ethanol, b) 10 nm AAO membrane in φ_w = 0.1, c) 20 nm AAO membrane in pure ethanol, and d) 20 nm AAM membrane in φ_w = 0.1. The plots in the left column show the full transient while those on the right show expanded regions of the same transients depicting long burst events. All transients have 1 ms time resolution.

The mechanism of slow diffusion within the nanopores was further investigated by carefully inspecting the time transient data over shorter time scales. Figure 3.8 plots representative transients from both the 10 nm and 20 nm nanopores for solutions having $\varphi_w = 0.0$ and 0.1. Expanded segments highlighting regions 5 s in length are shown in the right column of Figure 3.8. These reveal the presence of relatively long fluorescence bursts of ~ 1 s duration. Such bursts were relatively common in all time transients, regardless of φ_w. In most cases they are characterized by a short rise in fluorescence that is followed by a long period of nearly-constant fluorescence (within shot noise limits). They usually end with a short drop in signal, with a return to background levels. Both the rise and fall in the fluorescence usually occur over a few bin times. Note that shorter events (i.e., << 1 s) that are less easily identified are also believed to appear throughout these data. These observations are most consistent with diffusion of individual molecules into the detection volume where they adsorb to the pore surface. They later desorb and diffuse out of the detection region. A similar slowing of biomolecule and nanoparticle diffusion due to surface adsorption within anodic alumina nanopores has been reported previously.[65,131] The current results are also similar to those reported by Wirth and coworkers for dye molecules diffusing near modified planar silica surfaces.[128,132] In these latter studies, fluorescence bursts exhibiting long periods of constant signal levels were also detected. In contrast to the present data, these bursts commonly ended in a more abrupt drop to background in a single bin time, and were attributed to rare strong adsorption of the dye to the surface, with the events ending in the return of fast solution-phase diffusion. The FCS data acquired in these previous studies were fit to a different model than Eq. 3.3. Due to the greater frequency of apparent adsorption events in the present studies, and because these usually end with a resumption of relatively slow diffusion, Eq. 3.3 is believed to be the better model. It

should also be noted that all experiments in the present studies were performed at very low dye concentrations (2 nM RhB) where neither aggregation of the dye nor saturation of surface adsorption sites are expected.

3.3.4 Raman Scattering Spectroscopy

Raman spectroscopy was employed as a means to confirm the exchange of solvent mixtures within the pores and to uncover any possible differences in the structures of the bulk and nanoconfined solvents. Figure 3.9a-c plot Raman spectra obtained from bulk ethanol solution, ethanol confined within a 20 nm AAO membrane and solvent-free 20 nm AAO membrane in the 370 cm^{-1} to 2100 cm^{-1} spectral range, respectively. Spectra were also acquired at higher Raman shifts (i.e., 2900 cm^{-1} to 4000 cm^{-1}, data not shown). The lower frequency Raman spectra reveal peaks from C-C-O and C-O vibrational modes (880 cm^{-1} - 1105 cm^{-1}) and for CH_2 and CH_3 deformation modes (1280 cm^{-1} - 1460 cm^{-1}).[133] Spectra obtained from within the AAO membranes include additional peaks in 400-750 cm^{-1} and 1000-1100 cm^{-1} spectral regions. The exact origins of these peaks are uncertain but could comprise peaks from the anodic alumina itself or from anionic impurities incorporated into the membranes during anodization.[134]

The peak assigned to the C-C-O vibration at ~ 888 cm^{-1} was fit as a means to verify that the solvent composition within the AAO membrane nanopores is similar to that in bulk solution. This analysis was also expected to reveal any detectable changes in solvent structure upon its incorporation within the nanopores. The Raman peaks were all fit to Voigt profiles. Figure 3.9d,e plots both Raman shifts and peak areas for the C-C-O vibration in bulk solution (black squares) and in the 10 nm and 20 nm nanopores (blue and red squares, respectively) as a function of φ_w.

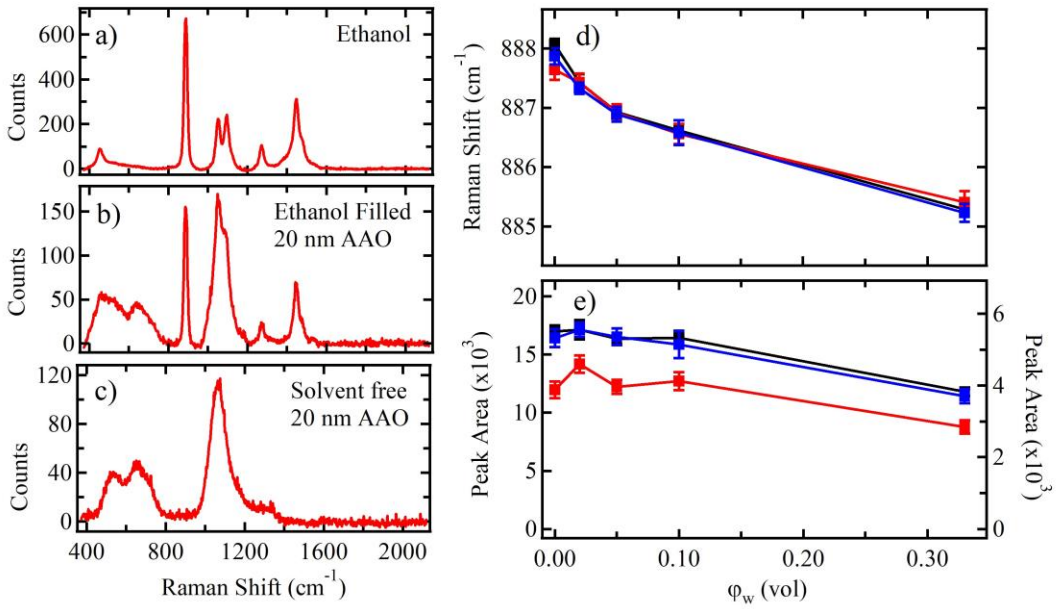

Figure 3.9 Raman scattering spectra for a) bulk ethanol solution and b) ethanol-filled 20 nm AAO nanopores and c) solvent free 20 nm AAO nanopores. Analysis of Raman data showing d) Raman shift for the CCO vibrational mode at 888 cm^{-1} and e) peak area for the CCO mode as a function of volume fraction water in ethanol/water mixtures. The left axis gives peak area in bulk solution while the right axis gives peak area in the AAO membranes. Error bars show 95% confidence intervals. The spectra have been subtracted background using a polynomial fit to the baseline.

The peak positions (Figure 3.9d) reveal a gradual change in vibrational frequency that has been assigned previously to changes in the hydrogen bonding network of the solvent mixture as water is added.[135,136] No apparent differences in the Raman shift for this mode are observed between the bulk and nanoconfined solvents. Besides shifts in the scale of the peak areas shown in Figure 3.9e, which are most likely due to differences in the pore densities of the specific AAO membranes employed, no clear differences are observed between bulk solution and solvents confined to the 10 nm and 20 nm nanopores. These data are most consistent with similar solvent mixture compositions in both bulk solutions and within the nanopores.

3.4 Discussion

3.4.1 Trends in D_f with Solution Composition and Pore Size

The data plotted in Figure 3.6a demonstrate that the solvent-composition-dependent trends in D_b and D_f are strongly correlated for both pore sizes. It is clear that bulk-like composition-dependent changes in the viscosity of the confined solvent mixtures play an important role in determining the rate of fast RhB diffusion. However, the residual dependence on solvent composition depicted in Figure 3.6b points to additional contributing factors.

It is possible that the mixture composition within the nanopores differs from that in bulk solution, resulting in further changes in the local viscosity. Indeed, molecular dynamics simulations of 1 nm slit-like AAO pores have shown that the water content of ethanol/water mixtures is significantly enhanced compared to bulk liquid.[38] However, any enhancement of the water content within the relatively large 10 nm and 20 nm nanopores employed here may be too small to produce the observed effects. Raman scattering experiments comparing ethanol Raman spectra obtained from bulk solution and nanopore-confined mixtures revealed no detectable differences in composition.

It has also been shown that hydrogen bonding in ethanol/water mixtures is composition dependent.[40,137] These effects may differ in nanoconfined liquids and may also lead to changes in local solvent viscosity. Again, the Raman scattering experiments provided no evidence of such effects, with both bulk and nanoconfined mixtures yielding similar spectra.

Changes in solution viscosity within the nanopores may also arise from the formation of a stagnant solvent layer near the pore surface. This stagnant layer would impart additional drag on both solvent and solute molecules, slowing their motions. A pictorial model for this mechanism is given in Figure 3.10a where the dashed lines represent the transition from freely mobile

solvent to the stagnant layer. The impact of a stagnant layer on the measured diffusion coefficient is most commonly modeled by the Renkin equation.[138] The form of the Renkin equation employed here describes molecular motions within the pores alone, as defined in Eq. 3.4.

$$\frac{D_r}{D_b} = 1 - 2.104\left(\frac{r_{RhB}}{r_p}\right) + 2.09\left(\frac{r_{RhB}}{r_p}\right)^3 - 0.95\left(\frac{r_{RhB}}{r_p}\right)^5 \qquad 3.4$$

Here, r_{RhB} represents the effective radius of the RhB molecule, and r_p the radius of the AAO nanopores. The hydrodynamic radius of RhB was estimated to be 0.52 nm from D_b in a series of solvent mixtures (see Figure 3.5), while r_p = 5 nm and 10 nm for the two AAO membranes.

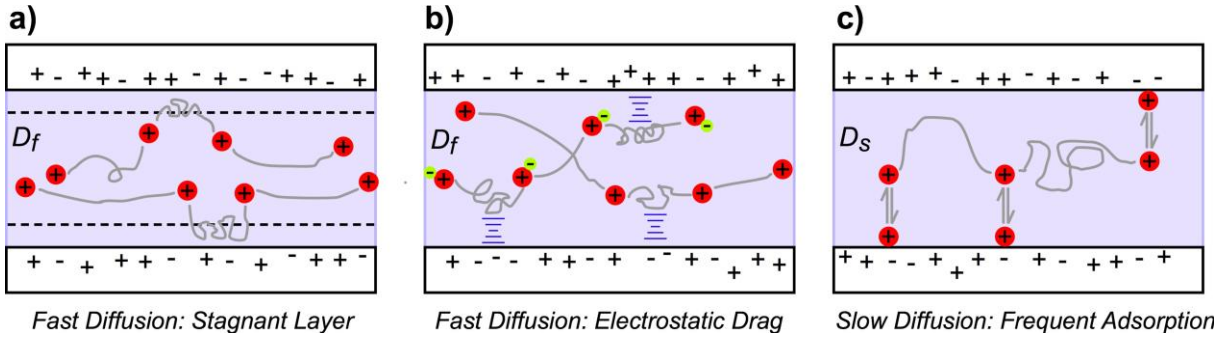

Figure 3.10 Models for the dominant effects believed to yield the observed reductions in D_f and D_s within the AAO nanopores relative to D_b, and their composition dependences. a) Hydrodynamic drag imparted by a thin, stagnant layer of solvent (dashed lines, not to scale) near the pore walls. b) Electrostatic drag due to interactions between the cationic form of RhB and anionic impurities in the AAO or its counter ion and cationic sites on the pore walls. c) Reversible adsorption of the dye at the pore surfaces, possibly due to ion pairing or hydrogen bonding.

Estimates of D_r/D_b, where D_r is the diffusion coefficient from the Renkin model, are plotted in Figure 3.6b (dashed lines). The Renkin model reveals that confinement of RhB within the AAO pores is expected to cause a detectable slowing of its diffusion. However, the observed reduction in D_f/D_b is significantly larger than predicted. Furthermore, the Renkin equation provides no explanation for the composition dependence of D_f. While hydrodynamic drag likely

plays a role in the observed reduction in D_f relative to D_b, it clearly does not explain the full effect.

Electrostatic interactions between the charged dye (or its counter ion) and oppositely charged sites on the pore surfaces provide another possible explanation for the observed reduction in D_f relative to D_b (see Figure 3.10b). While AAO membranes are usually reported to carry a small positive charge at pH < 7,[139,140] it is also well known that anodic membranes incorporate anions during the anodization process.[134,141] Electrostatic interactions would impart an additional drag on dye motions and are expected to occur over relatively large distances in the absence of added electrolytes. Similar effects have been reported previously by Daniels, et al. for diffusion of charged dyes near planar silica surfaces.[142] Notably, the charged dyes do not adsorb to oppositely charged sites on the pore surfaces in this model, but rather are simply slowed by their electrostatic interactions. While the exact origins of the reduction in D_f relative to D_b and its composition dependence remain uncertain, it is believed that both hydrodynamic drag and electrostatic interactions likely play a role.

3.4.2 Trends in D_s with Solution Composition and Pore Size

The slow diffusive motions of RhB portrayed in Figure 3.7 are also likely impacted by the hydrodynamic and electrostatic effects mentioned above for D_f. However, the much greater reduction in D_s relative to D_b, and its completely different dependence on mixture composition, indicate that other factors are more important. As suggested by the time transient data in Figure 3.8, slow RhB diffusion is instead most likely limited by frequent, reversible adsorption of RhB to the pore walls. While the exact nature of the interactions between RhB and the pore surfaces remain unknown, it is possible that the surfaces incorporate anionic sites as noted above [134,141] The pore surfaces are also likely rich in hydroxide moieties.[106] The former would serve as sites

where cationic RhB could electrostatically bind to the surface, while the latter could act as donor sites for hydrogen bonding with the dye. Both models provide possible explanations for the observed increase in D_s and the decrease in $A_s/(A_s + A_f)$ with increasing φ_w (Figure 3.7c). The increased solvent dielectric constant at larger φ_w would lead to better screening of the charged dye from charged surface sites, and decreased contributions from electrostatic adsorption. Likewise, the increased water content would also provide greater competition for hydrogen bonding sites on the pore surfaces. Furthermore, as has been shown in both experimental and computational studies of water-ethanol mixtures confined within AAO nanopores, water is expected to form a layer near the pore surface even at relatively low φ_w,[34,40] providing nanoconfinement-induced reductions in the occurrence of any such RhB-surface interactions. The slowest diffusive motions of the RhB dye within the AAO nanopores is thus attributed to a desorption-mediated mechanism similar to that reported in several previous publications that explored dye diffusion near planar oxide surfaces.[143-146] A very similar mechanism has been proposed for slow protein diffusion in slit-like nanochannels,[36] and has been employed previously in the interpretation of biomolecule and nanoparticle diffusion in nanoporous anodic alumina.[65,131] Future wide-field video microscopy studies of these materials are expected to provide additional evidence in support of this model.

3.5 Conclusions

Single molecule detection and FCS methods have been used to explore the rates and mechanisms of RhB diffusion within AAO membrane nanopores filled with a series of ethanol/water mixtures. Experiments were performed as a function of pore size, employing AAO membranes having 10 nm and 20 nm diameter cylindrical pores, and as a function of solvent composition in mixtures ranging from pure ethanol to 33% (by volume) water and

ethanol. The FCS results revealed the occurrence of two distinct diffusion mechanisms for RhB confined within the nanopores that were interpreted as fast and slow 1D diffusion. These processes were characterized by their mean diffusion coefficients, D_f and D_s, both of which were significantly smaller than the mean RhB diffusion coefficient, D_b, measured in bulk solutions of the same composition. The slow diffusion process yielded mean D_s values that were 10-100-fold smaller than the associated mean D_f values. Both D_f and D_s exhibited clear dependences on pore size but distinctly different dependences on solvent mixture composition. The D_f values exhibited a composition dependence that closely mimicked that of D_b, largely decreasing with increasing water fraction. Hindered diffusion in this case was attributed to the slowing of dye motions by increased hydrodynamic drag caused by a stagnant layer of solvent near the pore walls and by relatively long-range electrostatic interactions between the charged dye and oppositely charged sites on the pore surfaces. In contrast, the D_s values increased with water fraction while the contributions of slow diffusion to the autocorrelation functions decreased across the same series of mixtures. Relatively frequent, reversible adsorption of the RhB dye to the pore surfaces was concluded to be the dominant factor in determining the observed D_s values, with reversible adsorption occurring by electrostatic interactions between the charged dye and oppositely charged sites on the pore surfaces or by hydrogen bonding between the dye and surface hydroxides. These interactions may be moderated in mixtures of greater water fraction, due to formation of a water layer on the pore surfaces. The results and observations of these studies provide valuable new insights into how solutes and solvents behave under nanoconfinement within AAO membrane nanopores.

Chapter 4 - Adsorption and Solvation Modulate Rhodamine B Diffusion in Ethanol/Water-Filled Anodic Alumina Nanopores

Adapted with permission from: Rashidi, H.; Nathani, A.; Wang, X.; Servis, M. J.; Ito, T.; Higgins, D. A. *J. Phys. Chem. C* **2024**, *128*, 14326-14336, Copyright 2024 American Chemical Society. (https://doi.org/10.1021/acs.jpcc.4c03189).

4.1 introduction

Nanoporous membranes are now being widely investigated for use in advanced chemical separations.[147-149] Once fully developed, these materials may help overcome performance limits imposed by the well-known permeability versus selectivity trade-off.[150] In order to realize the full potential of these materials, the unique behaviors frequently exhibited by solvents and solutes under nanoconfinement must be better understood.[151-154] Indeed, a plethora of interesting phenomena arise when molecules are confined within nanopores.[153] For example, the freezing points and glass transition temperatures of solvents are often depressed under confinement.[155,156] Solvent and solute dynamics have been shown to slow under these same conditions.[105,157] The chemical compositions of nanoconfined mixture have also been reported to differ from those of bulk solution.[37,38] These compositional variations may reflect differential partitioning of mixture components into the pores but may also arise from phase separation and layering of solvents near the pore walls. Such effects have been broadly predicted in simulations[38,39] and experimentally confirmed.[40,41] These surface layers may either promote or limit behaviors important to chemical separations, including the partitioning of solutes into nanopores[42] and/or their adsorption to pore

surfaces.[43] Interestingly, oriented solvent layers also exhibit dielectric (i.e., polarity) properties that differ from those of bulk liquids.[43,158]

A complete understanding of the molecular-level mechanisms by which solutes diffuse within nanoporous materials and interact with or adsorb to pore surfaces is critically important to optimization and implementation of emerging membrane separations. Unfortunately, the rates and mechanisms of solute diffusion and surface adsorption under nanoconfinement remain difficult to predict. Thermally excited random (e.g., Brownian) motion within nanopores may occur at the Stokes−Einstein-predicted rate, or it may be slowed by the appearance of stagnant solvent layers at the pore surface.[138] Molecular motion may also be modified by relatively long-range electrostatic interactions,[142,159,160] or by short-range hydrogen bonding and van der Waals interactions. The latter require that solutes closely approach and collide with pore surfaces, yet the rate of solute collisions with nanopore walls also depends on the degree and dimensionality of confinement.[153] The relative contributions of these factors are certain to depend upon solvent composition, solute chemistry, and the exact nature of solute and pore surface solvation. A complete understanding of these phenomena requires extensive experimentation, theoretical modeling, and computer simulations. [62,69,71]

In this chapter, fluorescence correlation spectroscopy (FCS) is used to investigate the mass transport dynamics of rhodamine B (RhB) dye molecules confined within uniform 10 and 20 nm diameter nanopores of anodic aluminum oxide (AAO) membranes. The membranes are filled with ethanol/water mixtures ranging from pure ethanol to pure water in order to explore the dependence of dye diffusion on mixture composition. The experimental geometries used in FCS experiment are shown in Figure 4.1. FCS experiments allow for diffusive dye motions to be characterized on time scales ranging from microseconds to seconds, allowing for rapid motions

of the dye to be detected within vertically oriented nanopores[65,70,131] while also revealing the interruption of these motions by adsorption of the dye to the pore surfaces on longer time scales. The results of these studies support the conclusions of our recent report[160] in which RhB mass transport within AAO nanopores was found to follow a two-component one dimensional (1D) diffusion mechanism over a limited range of ethanol/water mixtures (0−33 vol % water). This mechanism includes fast bulk-like diffusion and slow near-surface diffusion attributable to solute adsorption to the pore surfaces. RhB solubility data are acquired and are used to better understand the FCS data and the role played by interactions between the solvated dye and solvated pore surfaces in governing RhB surface adsorption and slow diffusion.

4.2 Methods

4.2.1 Materials

Rhodamine B (RhB) dye was obtained from Sigma-Aldrich and was used as received. Its concentration was maintained at 2 nM in all confocal FCS experiments. High purity water was obtained from Fisher Scientific (HPLC grade), while pure (200 proof) ethanol was obtained from Sigma-Aldrich (HPLC grade). Both were used as received. Experiments were performed under a series of specific ethanol/water mixtures as defined below, with mixture compositions ranging from pure ethanol to pure water.

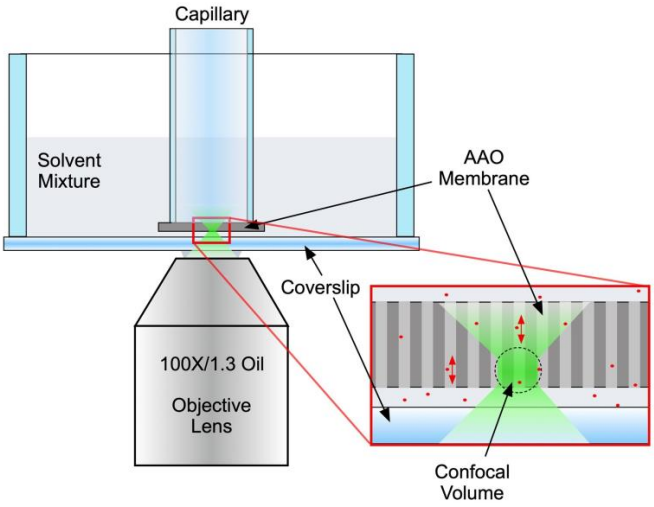

Figure 4.1 Experimental setup employed in confocal FCS experiments on vertically oriented AAO pores. An expanded view of the AAO membrane (not to scale) is shown at the lower right of panel. The red dots represent individual RhB molecules.

Nanoporous anodic aluminum oxide (AAO) membranes were obtained from InRedox, LLC as circular disks (10 mm in diameter) and were cut into four pieces for use in individual FCS experiments. As reported by the manufacturer, the membranes incorporate uniform, cylindrical 10 ± 2, 20 ± 3 and 30 ± 6 nm diameter nanopores that are oriented perpendicular to the face of each membrane and extend across the full 50 μm membrane thickness. Membrane porosity is quoted to be 12 ± 2% for 10 and 20 nm pore sizes, and 35 ± 5% for 30 nm AAO with pore densities of 1.6×10^{11} pores/cm^2 for 10 nm AAO and 5.8×10^{10} pores/cm^2 for both 20 and 30 nm nanopores. Previously reported scanning electron microscopy images are consistent with these claims.[160] All data in the present work were acquired from the same membrane face employed in the earlier report.[160] Solution-filled AAO nanopores were obtained by first immersing the membranes in pure ethanol. They were then placed under reduced pressure (<100 Torr) for 60−90 min, using an oil-free vacuum pump (KNF Lab Filtration Pump). The membranes were maintained under ethanol for at least 1 day prior to use. For FCS experiment, as shows at Figure 4.1, each membrane was transferred to an optical cell that was subsequently

positioned on a confocal microscope (see below). The solution cell comprised a 14 mm diameter glass tube that was attached to a microscope coverslip (FisherFinest, Premium) using either glass super glue or Parafilm. Once transferred to the cell, the membrane was immediately immersed under one of the RhB doped ethanol/water mixtures. It was maintained under the same solution for a period of at least 30 min prior to the start of each experiment. Whenever the solution composition was changed, at least 30 min was allowed for equilibration with the new mixture before the next experiment was initiated. The membrane was oriented horizontally above the microscope objective so that the long axes of the pores were parallel to the optical axis of the microscope. The capillary shown in Figure 4.1 was used to hold the membrane in place and was rigidly attached to a 3D micrometer stage (not shown).

4.2.2 Measurements

Fluorescence time transient data for use in FCS experiments[71] were acquired on a confocal microscope that has been described previously.[160] Briefly, the sample was mounted above an oil immersion objective (Nikon Plan Fluor, 100×, 1.3 NA, see Figure 4.1) on an inverted light microscope (Nikon TE-200). The sample was illuminated by directing 532 nm laser light through the objective lens to achieve a focused, diffraction-limited spot within the sample. The same objective was used to collect RhB fluorescence in reflection. A dichroic beam splitter (Chroma 550 DCLP) was used to direct the laser light into the back aperture of the objective and to block residual laser light reflected by the sample, while transmitting the collected fluorescence. An incident optical power of 10 μW, measured prior to reflection from the beam splitter, was used in all experiments, giving a power density of $\sim 4 \times 10^3$ W/cm^2 in the sample. This power was chosen to provide high signal-to-noise ratio data while avoiding photobleaching of the dye. The collected fluorescence was imaged through a 50 μm diameter pinhole (Thorlabs), then passed

through a bandpass filter (Chroma, 580/40m), and focused onto a single-photon counting avalanche photodiode detector (APD, PerkinElmer SPCM-AQ-141R). Electrical pulses output by the APD were counted using a National Instruments counter/timer board (PCIe-6612)[126] operated in the time-stamping mode. A 25 MHz clock was employed as the timer. The detection area of the confocal microscope was carefully calibrated using RhB diffusion in bulk solution,[160] yielding a $1/e^2$ radius of 260 nm. Data collection and analysis were performed using National Instruments Labview software, C++ code, and Igor Pro macros, all of which were written in house.[146]

The optical cell in FCS experiments was positioned on a 1.25 cm thick aluminum mounting plate that was attached to the microscope base, limiting focus drift to ca. ± 1 μm over >1 h. Once mounted in the cell and immersed under solution, the lower membrane surface has typically found 10−20 μm above the coverslip surface. A maximum coverslip-membrane distance of ∼40 μm was allowed in these experiments to avoid distortion of the confocal region caused by spherical aberrations when focusing at greater depths.[95,101,127] Fluorescence data were acquired from bulk solution by positioning the microscope focus 5 μm below the lower membrane surface. Data were acquired from within the AAO nanopores by moving the microscope focus 5 μm above the lower membrane surface.

4.3 Results and Discussion

4.3.1 Fluorescence Time Transients

An initial view of RhB diffusion and adsorption within the AAO nanopores was obtained from fluorescence time transients acquired on the confocal microscope. Data were collected from within each membrane by focusing the microscope 5 μm above the lower AAO surface (see Figure 4.1), while data from bulk solution were acquired by focusing 5 μm below the membrane.

Solutions spanning the full range of ethanol/water mixtures from pure ethanol to pure water were employed. All incorporated 2 nM RhB dye. Figure 4.2 plots representative time transients obtained from both 10 and 20 nm AAO membranes. Time transients from ethanol- and water-filled nanopores in the absence of dye are also included. Prominent bursts of fluorescence are observed in the time transients from within the AAO pores. These bursts are primarily due to 1D diffusion of individual RhB molecules through the detection volume. The time transients also incorporate evidence of RhB adsorption to the pore surfaces. Surface adsorption events appear as bursts of nominally constant fluorescence that last for tens of milliseconds or longer, as has been shown in our initial report,[160] and in earlier work characterizing molecular adsorption on planar surfaces. Shorter adsorption events are also certain to be present but are difficult to distinguish from bursts due to RhB diffusion.

Surface adsorption of RhB also contributes to an approximately constant "background" in each transient.[69] While membrane autofluorescence, light scattering, and detector dark counts may be a factor, the observed background is usually higher in the presence of dye (see Figure 4.2). This contribution may arise from relatively few molecules adsorbed within the confocal detection volume. However, as those in the detection volume are prone to photobleaching, the approximately constant background instead likely reflects an average background produced by many weakly emitting adsorbed molecules in distant regions. Distant molecules are weakly excited by the incident laser beam and may also emit at a lower quantum yield relative to molecules in solution.[69]

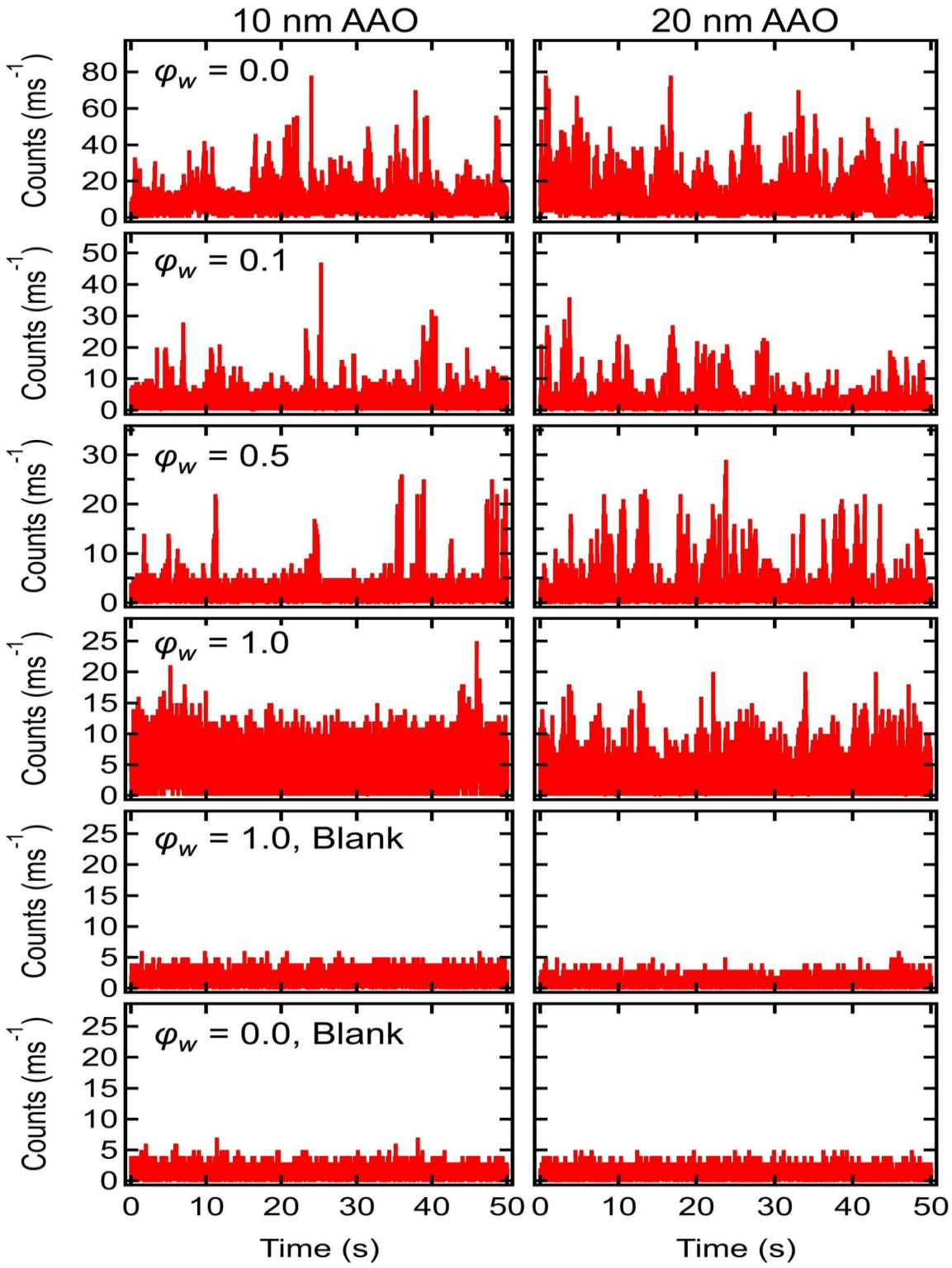

Figure 4.2 Representative time transients showing fluorescence bursts due to diffusion of RhB dye (at 2 nM) through the confocal detection volume, across the range of mixtures studied. The pairs at the bottom show time transients acquired from blank solutions in the absence of RhB. All transients are plotted with bin times of 1 ms.

Time transients like those given in Figure 4.2 often reveal evidence of RhB adsorption to the pore surface.[160] Adsorption of the dye to the pore surfaces is expected to dramatically slow its diffusive motions, leading to a reduction in the concentration of diffusing molecules and enhanced background from surface adsorbed molecules. The complex behavior of the average background levels shown in Figure 4.3 reflect the mixture composition dependence of RhB adsorption within the AAO nanopores.

The integrated signal and integrated background count rates in each transient were determined iteratively by statistically sorting the count rate data. Initial guesses of the signal and background count rates were manually selected. The signal level at each bin time was then assigned as signal or background using statistical methods, assuming the count rates are normally distributed about their mean values. As two different distributions are expected in the data, corresponding to background counts and signal counts, two different metrics were employed in assigning each data point as background or signal. The time transients employed in this analysis were all binned to a time resolution of 10 ms. Count rates determined to be at $\geq 97^{th}$ percentile of the background distribution were assigned as signal. Count rates determined to be at $\geq 35^{th}$ percentile of the signal distribution were also assigned as signal. All others were assigned as background. New mean background and signal count rates were calculated with each iteration through the data. Steady-state conditions in which < 1% of the pixel assignments changed with each subsequent pass through the data were typically achieved after 10 iterations, although 15 iterations were usually employed.

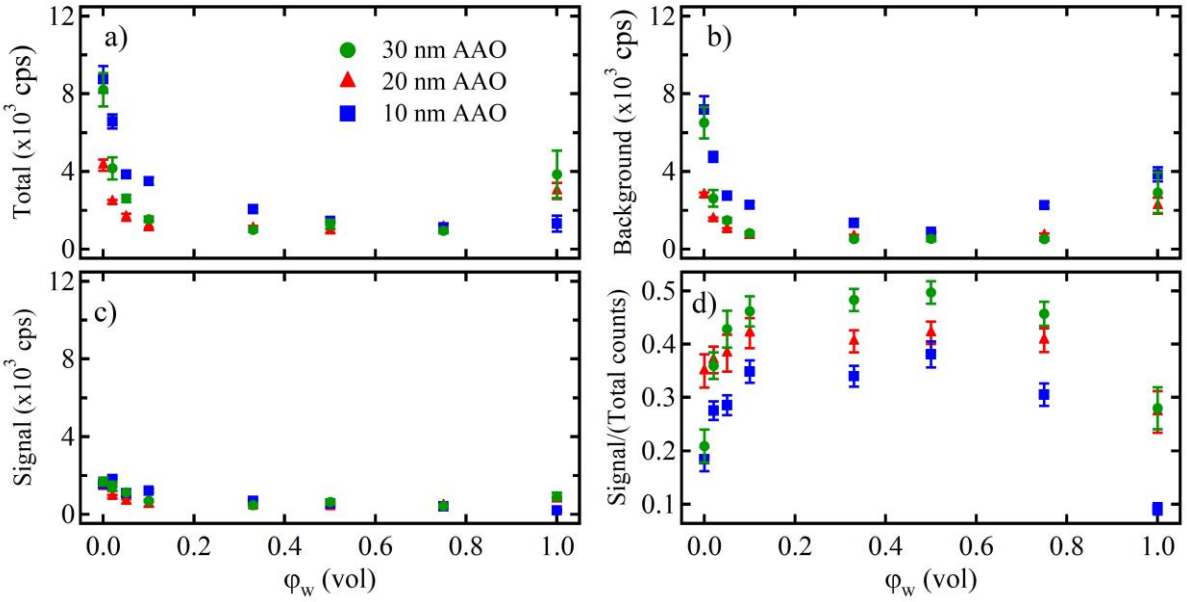

Figure 4.3 Signal and background analysis of confocal fluorescence time transient data acquired from RhB diffusing within AAO membranes. a) Integrated (total) fluorescence count rate in each transient. b) Background count rate determined by the iterative statistical sorting procedure described in the text. c) Signal count rate determined by the iterative statistical sorting procedure. d) Signal to total fluorescence count rate ratio in each transient.

The total count rate plotted in Figure 4.3a represents the total fluorescence observed in each transient (i.e., background + signal). The background count rate plotted in Figure 4.3b shows the total counts assigned as background derived from the sorting procedure described above. The total signal count rate was obtained by the same method and is plotted in Figure 4.3c. The ratio of signal to the total fluorescence count rate is plotted in Figure 4.3d. As shown in Figure 4.3, it is noteworthy that the signal count rates were approximately independent of pore size, while the background count rates were almost uniformly larger for the 10 nm nanopores. Furthermore, the background count rates were also strongly dependent upon ethanol/water mixture composition, with the highest background levels observed in pure ethanol. High background counts were also observed as the water content increased. The lowest count rates were observed for ethanol/water mixtures of intermediate composition. These observations are

consistent with the assignment of the background counts to fluorescence from RhB molecules adsorbed to the pore surfaces.

The results presented in Figure 4.3 reveal that the background varies significantly with mixture composition. It is largest in pure ethanol ($\varphi_w = 0.0$), relatively strong in pure water ($\varphi_w = 1.0$) and smallest in mixtures of intermediate composition. It is also relatively larger in the 10 nm nanopores. These results are consistent with relatively strong RhB adsorption to the pore surfaces in pure ethanol and pure water and much weaker adsorption in ethanol/water mixtures of intermediate composition. In the 30 nm nanopores, the higher background compared to the 20 nm nanopores could result from increased dye adsorption on the pore surfaces. This may be due to the longer etching time for the 20 nm nanopores, which could lead to the incorporation of more impurities, such as negative ions, on the pore surfaces. In contrast to the background data, the integrated signal from the fluorescence bursts (i.e., primarily diffusing molecules) is much less dependent on mixture composition and pore size (see Figure 4.3c). The latter suggests that while the concentration of adsorbed molecules varies with mixture composition, the concentration of diffusing RhB molecules within the pores is relatively constant.

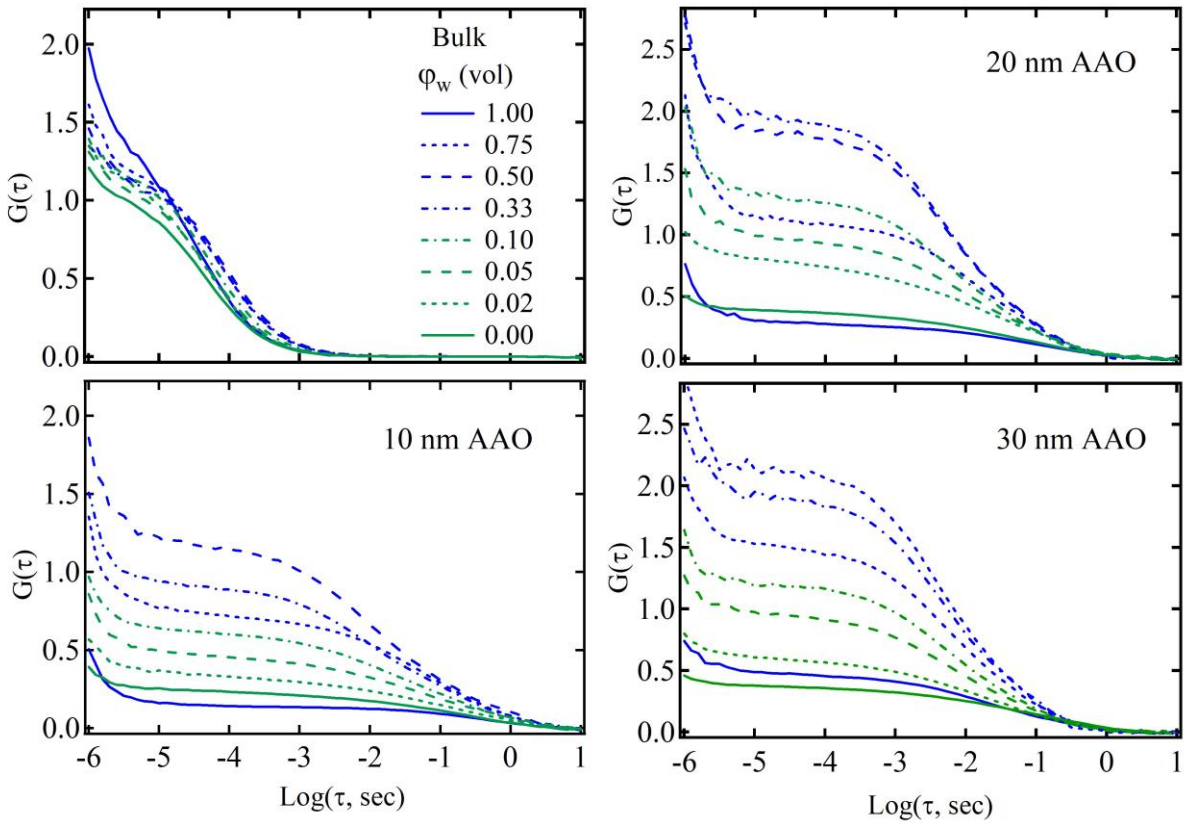

Figure 4.4 Representative autocorrelation functions for RhB in a) bulk solution, b) 10 nm diameter AAO nanopores, and c) 20 nm diameter AAO nanopores d) 30 nm diameter AAO nanopores. The results reveal a gradual rise in the autocorrelation amplitude from φ_w = 0.0, with a peak near φ_w = 0.5, and a subsequent decrease towards φ_w = 1.0. The autocorrelation decays are fastest in bulk solution (a) and slower in the AAO nanopores, with the 10 nm nanopores exhibiting the slowest decays, consistent with slowest RhB diffusion.

4.3.2 Fluorescence Correlation Spectroscopy (FCS)

Autocorrelation of the confocal time transient data (Figure 4.2) was used to quantitatively assess the rate of RhB diffusion as a function of mixture composition and pore size. Figure 4.4 plots representative autocorrelation functions, $G(\tau)$, obtained from bulk solution and from inside 10, 20 and 30 nm AAO membranes. Autocorrelation of the time transient data was accomplished via Eq. 4.1.

$$\boldsymbol{G(\tau) = \frac{\langle I(t)I(t+\tau)\rangle}{\langle I(t)\rangle^2} - 1} \qquad 4.1$$

Here, $I(t)$ and $I(t+\tau)$ represent the time transient data and a delayed version of the same. The triangular brackets indicate that the time-averaged value is employed.

As shown in Figure 4.4, a fast decay occurs in each autocorrelation function near ~ 10^{-6} s. The associated signal fluctuations are too fast to arise from molecular diffusion. They may instead reflect triplet blinking by the dye[129] or after-pulsing of the APD.[161] As neither is relevant to measurements of dye diffusion, this component is ignored in the remainder of the discussion. The decay near 10^{-4} s in Figure 4.4a is attributable to 3D diffusion of RhB in bulk solution. Its variation with solution composition arises solely from changes in mixture viscosity,[130] as described in our previous report.[160]

Autocorrelation data acquired from within the AAO membranes are shown in Figure 4.4b-d. These reveal significant variations in the autocorrelation amplitude with mixture composition. In all nanopores, the amplitude is largest in mixtures of intermediate ethanol/water content (i.e., $\varphi_w \sim 0.5$) and smallest in pure ethanol and pure water (solid lines in Figure 4.4b-d). This is in good agreement with the ratio of signal to the total fluorescence count rate shown in Figure 4.3.d. The autocorrelation decays obtained from RhB molecules within the membranes also occur on much longer time scales (i.e., 10^{-3}–0.1s) and are much broader than those in bulk solution, demonstrating that diffusion within the pores does not occur by a simple Fickian mechanism. Lastly, decays obtained from the 10 nm nanopores generally occur on longer time scales and are broader than those from the 20 and 30 nm nanopores, demonstrating that confinement of the dye contributes to both the slowing and complexity of its diffusion. Interestingly, the decay profiles from the 20 nm and 30 nm nanopores did not show any significant differences, confirming the loss of pore size dependence for nanopores larger than 20 nm.

The trends revealed in the autocorrelation decays from the inside of the membranes were quantitatively characterized by fitting them into a two-component model for 1D diffusion. This model is given in Eq. 4.2 and includes both fast (*f*) and slow (*s*) diffusive components.[160]

$$\boldsymbol{G(\tau)} \approx \boldsymbol{A_o} + \boldsymbol{B}\left[\boldsymbol{A_f}\left(\mathbf{1}+\left(\frac{\tau}{\tau_{D_f}}\right)\left(\frac{\mathbf{1}}{\gamma^2}\right)\right)^{-1/2} + \boldsymbol{A_s}\left(\mathbf{1}+\left(\frac{\tau}{\tau_{D_s}}\right)\left(\frac{\mathbf{1}}{\gamma^2}\right)\right)^{-1/2}\right] \quad 4.2$$

Here, A_o is a constant (≈ 0) and B defines the amplitude of the autocorrelation decay. In the literature, B is commonly used to obtain the average number of dye molecules, N, diffusing within the confocal volume, i.e., $N = 1/B$.[71,98,99] However, this is only valid in the absence of other contributions to the signal.[69,98,162] A_f and A_s represent the fractional contributions of fast and slow diffusion to the autocorrelation decay, while D_f and D_s are their mean diffusion times, respectively. The τ_D values are related to the apparent diffusion coefficients for fast and slow diffusion, D_f and D_s, by $D=w^2/4\tau_D$. Here, w is the calibrated1/e^2 radius of the confocal detection volume (260 nm in these studies). Lastly, γ (≈ 4)[101] is the ratio of the longitudinal and lateral dimensions of the confocal volume.

4.3.3 Autocorrelation Amplitude

As noted above, B in Eq. 4.2 is commonly used as a measure of the concentration of diffusing species in FCS measurements.[71,98,99] However, in the present studies, the nominally constant background fluorescence produced by adsorbed dye molecules complicates this analysis.[69,98,162] As discussed in the previous section, in the FCS studies assumed that $B=1/N$ is a condition valid in ideal situations where no background signal is present. However, this study has a non-negligible background, which affects the autocorrelation amplitude. Therefore, it is crucial to assess how this background influences the autocorrelation amplitude and adjust the analysis accordingly.

To find the relationship between the autocorrelation amplitude, *B*, and the average numbers of diffusing and adsorbed molecules, N_d and N_a, respectively, found in the detection volume, in the presence of background from detector dark counts, R_D, and light scattering, R_s, by the sample. This derivation is similar to prior work from our laboratory.[162] The autocorrelation amplitude is defined as follows:

$$\boldsymbol{B = G(0) = \frac{\langle (\delta I(t))^2 \rangle}{\langle I(t) \rangle^2}} \qquad 4.3$$

where Eq. 4.3 is equivalent to Eq. 4.1 at $\tau = 0$, and $\delta I(t)$ represent the fluctuations in the time transient data occurring as a result of dye diffusion through the detection volume. The fluorescence fluctuations due to dye diffusion are defined as follows:

$$\boldsymbol{\langle (\delta I(t))^2 \rangle = \left(q_d \sqrt{N_d}\right)^2} \qquad 4.4$$

when the number of diffusing molecules in the detection volume is Poisson distributed in time. In Eq 4.4, q_d describes the detection efficiency of the diffusing molecules, which includes its excitation efficiency, its quantum yield for emission, the incident laser power, etc. Note that neither permanently adsorbed molecules, nor detector dark counts or scattering from the membrane contribute to the fluctuations. In contrast, to Eq. 4.4, which is based solely upon the contributions of diffusing molecules, the mean fluorescence intensity is given by:

$$\boldsymbol{\langle I(t) \rangle = q_d N_d + q_a N_a + R_D + R_S} \qquad 4.5$$

where N_a is a constant representing the average number of adsorbed molecules in the detection volume, R_D is the mean number of detector dark counts contributing to the time transient in the shortest bin time employed (i.e., 10^{-6} s in Figure 4.4), and R_s is the mean number of scattered photons detected at a given laser power in the shortest bin time employed. Inserting Eqs. 4.4 and 4.5 into 4.3, Eq 4.6 are obtained:

$$\boldsymbol{B} = \frac{\boldsymbol{q_d{}^2 N_d}}{(\boldsymbol{q_d N_d + q_a N_a + R + S})^2} \qquad 4.6$$

Here, N_d and N_a are the average number of diffusing and adsorbed molecules detected, respectively. The parameters q_d and q_a represent the detection efficiencies of these molecules, and R and S the background contributions from detector dark counts and light scattering from the membrane. Unfortunately, none of these terms can be neglected in the present experiments. However, as discussed in above sections (see Figures 4.2 and 4.3), it is clear that the background from adsorbed molecules (i.e., q_aN_a) makes a dominant contribution to B. Therefore, variations in B are largely attributable to the dependence of N_a on mixture composition and pore size. In contrast, the smaller contributions of diffusing molecules (i.e., q_dN_d) to B remain relatively constant.

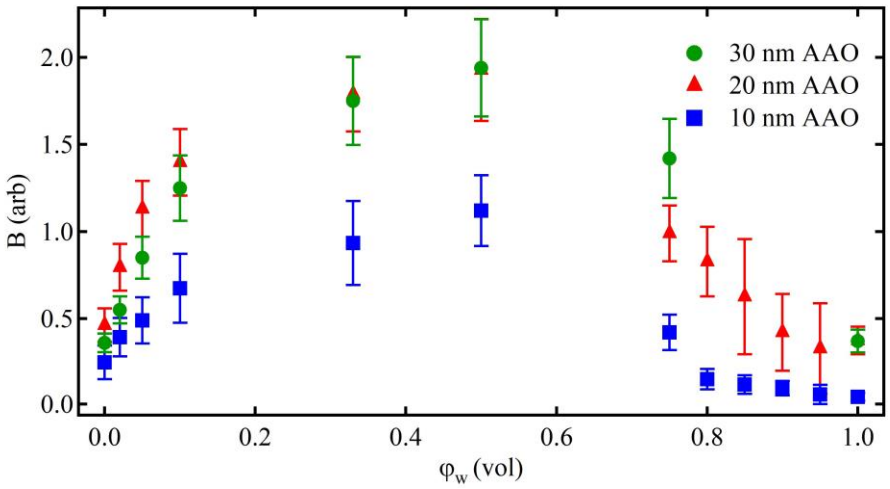

Figure 4.5 Autocorrelation amplitude B. The error bars show the 95% confidence intervals.

Figure 4.5 plots B for both 10, 20 and 30 nm AAO nanopores as a function of mixture composition. These data show that B is nearly two-fold smaller in the 10 nm nanopores over much of the ethanol/water mixture range, consistent with a greater concentration of adsorbed RhB molecules in the 10 nm nanopores. Furthermore, these data indicate that the concentration

of adsorbed molecules is greatest in pure ethanol and pure water, and smaller in the intermediate mixtures. Since the RhB concentration in bulk solution was held constant at 2 nM throughout these studies, changes in its adsorption strength are the likely cause of these variations. Thus, the data in Figure 4.5 suggests that RhB adsorption strength is influenced by both mixture composition and pore size for nanopores ranging from 10 nm to 20 nm, with the pore size dependence diminishing beyond 20 nm.

4.3.4 Solubility measurements

The solubility of RhB in ethanol/water mixtures was investigated because of its apparent importance in governing both the concentration of adsorbed RhB molecules and the rate at which molecules diffuse by the slow mechanism (see Figure 4.10).

RhB solubility was determined by both NMR[104] and classical gravimetric methods.[163] In the gravimetric studies, a series of 800 µL solutions of pure ethanol, pure water, and ethanol/water mixtures of φ_w = 0.20, 0.40, 0.60, and 0.80 volume fraction water were prepared in clean, disposable vials. Into each vial was added 700 mg of RhB. These were vigorously shaken and sonicated for 30 min to dissolve the RhB. The solutions were then allowed to sit for ~ 5 h to reach equilibrium solubility. They were next centrifuged for 2 h to separate any undissolved solids and then allowed to sit overnight. The following day, each supernatant solution was carefully removed and transferred to another vial without disturbing the solids. The supernatant solutions were subsequently weighed on an analytical balance and were next placed in an oven and gradually heated to 100 ºC for several hours for initial drying at atmospheric pressure. Afterwards, they were transferred to a vacuum oven (Isotemp Vacuum Oven, Fisher Scientific, < 1 torr) and left under dynamic vacuum overnight at 120 °C. The vials were then allowed to come to room temperature under vacuum. Lastly, they were removed from the oven

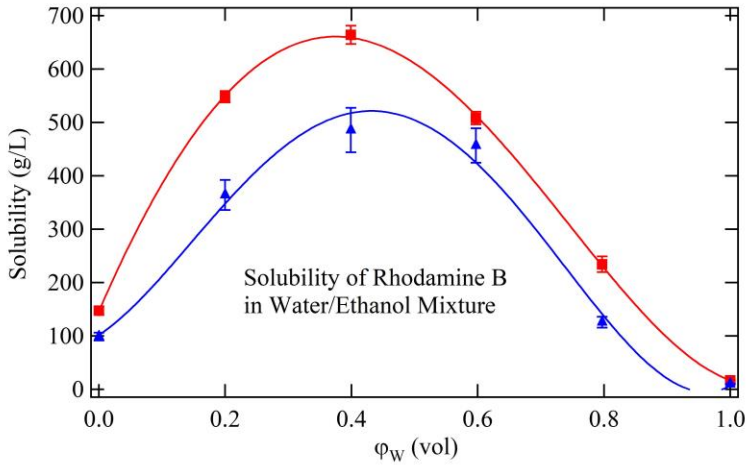

Figure 4.6 RhB solubility, *S*, in ethanol/water mixtures as a function of volume fraction of water, $\boldsymbol{\varphi_w}$. RhB solubility was determined both by a gravimetric procedure and by NMR. The greater solubility depicted by the gravimetric data in some measurements may result from difficulties in evaporating all of the solvents from the supernatant.

and weighed to determine the mass of RhB dissolved in each solution. RhB solubility, *S*, was determined from Eq. 4.7.

$$\boldsymbol{S} = \frac{\boldsymbol{m_{RhB} \times \rho_{mix}}}{\boldsymbol{m_{sup} - m_{RhB}}} \qquad 4.7$$

In Eq. 4.7, m_{RhB} is the mass of the dry RhB collected, m_{sup} is the mass of the supernatant, and ρ_{mix} is the density of each ethanol/water mixture. The density of each solution was obtained from the literature.[130] NMR studies[104] were used to confirm RhB solubility determined by the gravimetric method. NMR solubility data are plotted along with *S* from the gravimetric studies in Figure 4.6.

The gravimetric and NMR solubility data clearly demonstrate that RhB is most soluble in ethanol/water mixtures of intermediate composition and least soluble in pure ethanol and pure water. Indeed, mixtures of ethanol and water have been shown previously to result in enhanced solubility for many different solutes.[164] Figure 4.7 shows correlations between *B* (Eq. 4.2) and *S* in the 10, 20 and 30 nm nanopores. The values of *S* used in Figure 4.7 were obtained by interpolation of the data in Figure 4.6.

All experiments used a balance with a precision of 0.0001 grams to measure the dye weight and the pure solution before mixing, based on the pure solvent mixture. In this study, variations in the mixture volume were not considered, which could lead to an increase of approximately 3.5% in solubility for the intermediate mixtures.

A simple expression for the RhB surface adsorption coefficient, K, modeling both the observed pore-size and mixture composition dependences, is given in Eq. 4.8.

$$\boldsymbol{K = \frac{k_c P}{k_d}} \qquad 4.8$$

Here, k_c is the rate constant for RhB collisions with the pore walls, P is the probability that each collision results in an adsorption event, and k_d is the rate constant for RhB desorption. The collision rate constant depends on pore radius, r, with $k_c \propto D/r^2$. A greater collision rate at constant D within smaller pores would thus result in a larger K, as is consistent with the pore size dependences of B and N_a described above. Both P and k_d are expected to depend on RhB solubility in a given mixture, with greater RhB solubility leading to a smaller P and larger k_d. Unfortunately, the exact dependences of P and k_d on dye solubility are difficult to predict at present.

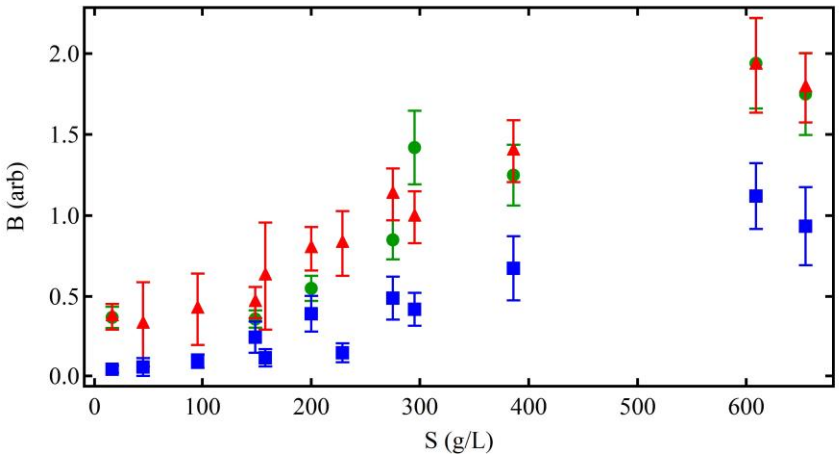

Figure 4.7 Correlation between B and S for 10, 20 and 30 nm AAO nanopores. The solubility values were obtained by interpolation from the curve in Figure 4.6. The error bars show the 95% confidence intervals on each measurement.

Experimental evidence for the role of solubility in governing RhB diffusion was obtained by comparing RhB solubility in a series of bulk ethanol/water mixtures to the FCS parameters. RhB solubility was measured by both gravimetric and NMR-based methods, Figure 4.6 plots gravimetric RhB solubility across the range of mixtures studied. These data demonstrate that RhB is most soluble in mixtures of intermediate composition, with peak solubility observed near φ_w = 0.4. The dye is least soluble in pure water and also relatively less soluble in pure ethanol. Figure 4.7 shows a clear correlation between B and RhB solubility, which implies that RhB adsorption to the pore surfaces becomes weaker as the dye becomes more soluble in the ethanol/water mixtures.

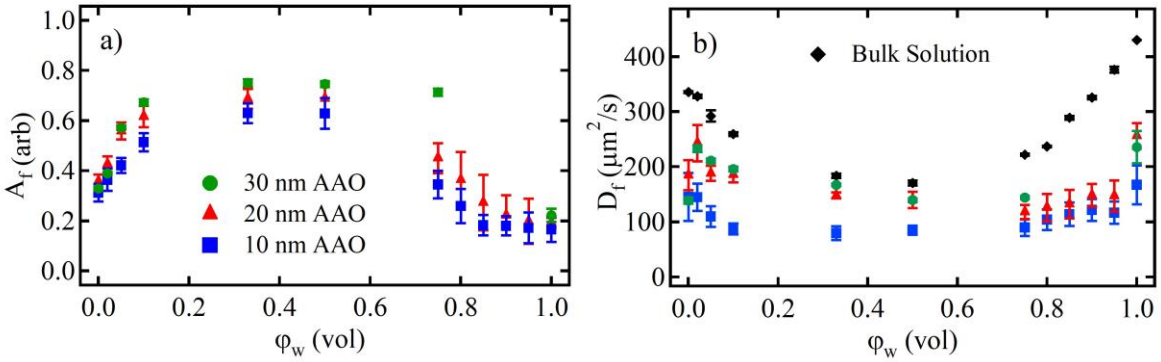

Figure 4.8 a) A_f for RhB in 10, 20 and 30 nm AAO nanopores as a function of water volume fraction in each mixture. b) D_f and D_b for RhB in the 10, 20 and 30 nm nanopores and in bulk solution, respectively. The error bars show the 95% confidence intervals on each measurement.

4.3.5 Fast Diffusion Mechanism

Figure 4.8a plots the autocorrelation decay amplitude, A_f, for the fast diffusion mechanism within the 10, 20 and 30 nm AAO nanopores as a function of mixture composition. The composition dependence of A_f closely follows those of B and RhB solubility described above, indicating that diffusion by the fast mechanism becomes relatively more common as RhB solubility increases. Figure 4.8b plots D_f for fast RhB diffusion in the 10 and 20 nm nanopores, along with its diffusion coefficient in bulk solution, D_b. These data reveal that D_f is generally

smaller than D_b, but otherwise follows a similar composition-dependent trend, revealing that D_f is determined primarily by solution viscosity, η, where $D \propto 1/\eta$ by the Stokes-Einstein equation. These results and observations are consistent with those of our initial report for a much narrower range of mixtures.[160] They strongly support the assignment of fast RhB diffusion to bulk-like diffusion in the central cavity of the AAO nanopores.

4.3.6 Slow Diffusion Mechanism

Figure 4.9 plot A_s, for RhB in 10, 20 and 30 nm AAO nanopores as a function of mixture composition, which, A_s ($A_s = 1-A_f$) is included to best show how contributions of the slow diffusion mechanism vary with pore size and mixture composition. The value of A_s is clearly anticorrelated with RhB solubility, consistent with greater RhB adsorption to the pore surfaces in pure ethanol and pure water, and reduced adsorption in intermediate mixtures. It also shows that slow diffusion becomes less common in larger nanopores.

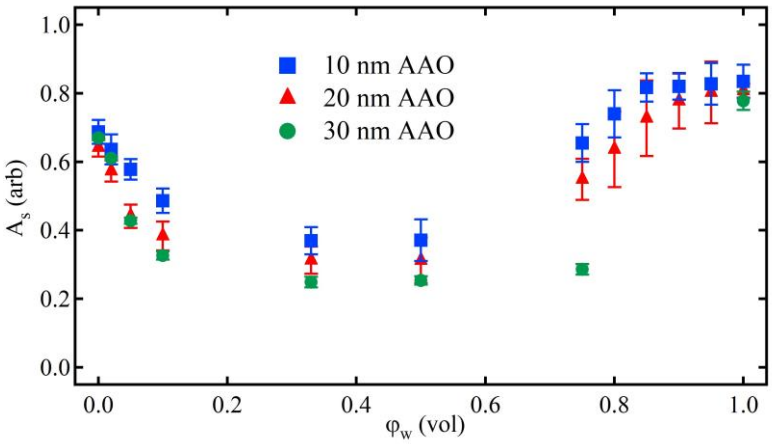

Figure 4.9 A_s, for RhB in 10, 20 and 30 nm AAO nanopores as a function of water volume fraction in each mixture. The error bars show the 95% confidence intervals on each measurement.

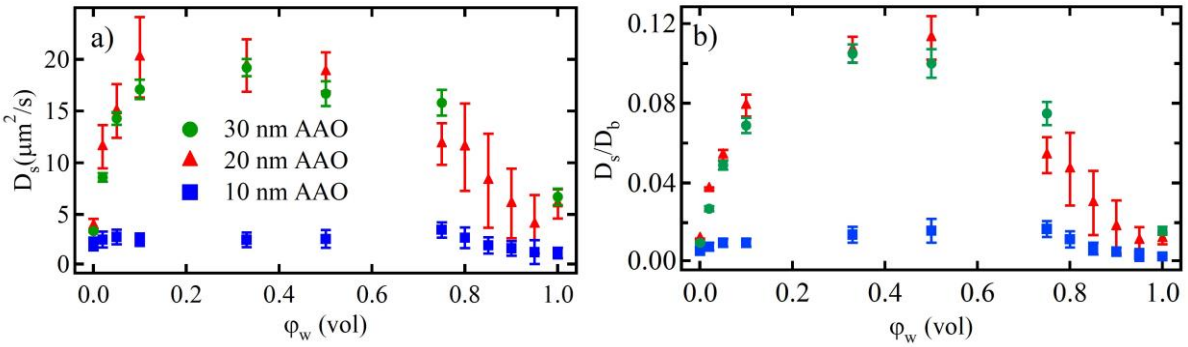

Figure 4.10 a) D_s for RhB in the 10, 20 and 30 nm nanopores. b) D_s/D_b for RhB in the nanopores. The error bars show the 95% confidence intervals on each measurement.

Figure 4.10 plots, D_s, and D_s/D_b for RhB in 10, 20 and 30 nm AAO nanopores as a function of mixture composition. The values obtained for D_s compare well with diffusion coefficients measured previously by single molecule methods in slightly larger AAO nanopores,[69] but are 10-100-fold larger than reported for an anionic dye in pores of similar size, as measured by flux methods.[39]

Interestingly, the plots of D_s and D_s/D_b show trends that closely mimic RhB solubility (compare Figures 4.6 and Figure 4.10a,b) and differ dramatically from those expected based on mixture viscosity (see Figure 4.8b). The similarities in the former are consistent with a dominant role for surface adsorption in determining the rate of diffusion by the slow mechanism. This assignment is further supported by the much smaller D_s values measured for RhB diffusion in the 10 nm nanopores compared to those in the 20 and 30 nm nanopores, where D_s remains nearly constant. As noted above, an increase in K (Eq. 4.8) is expected in smaller nanopores.

As a result of these observations, slow diffusion is assigned to a near-surface desorption-mediated mechanism[165-167] in which the pore surface collision rate and dye solubility both play important roles in determining the strength of RhB adsorption to the pore walls. Again, solubility likely affects the probability of surface adsorption and the rate of desorption. In desorption-mediated diffusion, the dye may remain immobile while adsorbed to the pore surface,

becoming mobile only when it desorbs into solution. Diffusion by the dye would then occur only by the fast mechanism, as defined by D_f. The value of D_s in this case represents an apparent diffusion coefficient limited not by dye motion but rather by the (small) fraction of total available time the molecule spends diffusing in solution. This model closely follows the behaviors described in a number of publications reporting the observation of desorption-mediated diffusion at macroscopic planar surfaces.[143-146,165-167] The present results suggest that solute diffusion by a desorption-mediated mechanism may also be common within nanoporous materials.

It should also be noted that both the pore surface charge and the charge on the dye are likely to vary with mixture composition. Therefore, charge effects may also contribute to the observed composition dependence of D_s. However, as the dielectric constant for ethanol-water mixtures decreases monotonically from pure water to pure ethanol,[168] the strength of any electrostatic interactions is expected to also vary monotonically across the range of mixtures studied. As the trends observed (see Figure 4.10) are markedly different, any such charge effects may be negligible.

4.3.7 Molecular dynamics simulations

To further investigate the role of RhB solubility in surface adsorption and slow diffusion, our collaborator at Argonne National Lab (ANL)[169] performed molecular dynamics (MD) simulations for ethanol/water mixtures confined within an alumina nanoslit and for RhB solvation in bulk solutions. The simulations revealed excess water at the alumina surface due to favorable interactions with polar Al-OH sites. However, in bulk ethanol/water mixtures, RhB is preferentially solvated by ethanol in all mixtures investigated, with water selectively interacting with the dye's oxygen and nitrogen heteroatoms, and its carboxylic acid and ammonium groups.

These findings suggest that RhB adsorption to the alumina surface in intermediate ethanol/water mixtures requires significant reorganization of its solvation shell. As experimental observations corroborate, this energy barrier competes with attractive surface interactions, resulting in RhB's mobility within these mixtures. In contrast, pure ethanol or water allows for better alignment of solvation at the surface, enhancing adsorption and reducing diffusion.

4.4 Conclusions

In summary, confocal fluorescence correlation spectroscopy have been employed to better understand the mechanisms of RhB mass transport within 10, 20 and 30 nm diameter AAO nanopores filled with ethanol/water mixtures ranging in composition from pure ethanol to pure water. The results provide support for the previous assignment of RhB diffusion to a two-component mechanism comprising fast and slow 1D diffusion in a more limited study.[160] Fast diffusion is attributed to viscosity-dependent bulk-like Brownian motion within the nanopores, while slow diffusion may involve a desorption-mediated mechanism in which the dye remains immobile while adsorbed to the pore walls and only moves upon desorption into solution.[165-167] Adsorption of RhB to the pore surface was revealed through the analysis of confocal fluorescence time transient data, which was in good agreement with the wide-field fluorescence videos also performed in our group.[169] Interestingly, the density of adsorbed dye, as reflected by the autocorrelation amplitude, B, and the apparent diffusion coefficient for slow diffusion, D_s, exhibited clear mixture-dependent correlations with RhB solubility. RhB surface adsorption was most significant in pure ethanol and pure water, where the dye was less soluble, while RhB diffusion was more prevalent in ethanol/water mixtures of intermediate composition, in which it was more soluble. D_s was also found to be smallest in the pure liquids and largest in mixtures of intermediate composition. The MD simulations of our collaborator related to this research also

revealed that the dye was solvated primarily by ethanol across much of the range of mixtures investigated, while the pore surface was covered by a layer of water.[169] Dye-pore collisions were also likely to be important. Contributions by the slow diffusion mechanism became more significant and D_s was smaller in the 10 nm nanopores than in the 20 and 30 nm nanopores where D_s remains nearly constant. Taken together, the experimental and simulation results provide strong evidence that dye-pore collisions and solvation-dependent dye surface adsorption are important factors governing RhB diffusion in solvent mixtures under nanoconfinement. These results will aid in the development of nanoporous membrane based separations in solvent mixtures where membrane permeability and separation selectivity are particularly difficult to optimize. [62,170]

Chapter 5 - Fluorescence Correlation Spectroscopy Studies of Dye Diffusion on Fresh and Aged Post-Consumer and Virgin Polyethylene Terephthalate

Adapted with permission from: Rashidi, H.; Shafiee, O.; Higgins, D. A. *Anal. Chem.* **2023**, *95*, 11849-11853, Copyright 2023 American Chemical Society. (https://doi.org/10.1021/acs.analchem.3c02283).

All contact angle and AFM measurements for virgin plastic were conducted by Omid Shafiee.

5.1 Introduction

Plastic materials that have escaped from waste streams or have been carelessly discarded are now ubiquitous in the environment.[171] When exposed to sunlight, air, and mechanical abrasion by the actions of wind and waves, large plastic objects slowly break down into ever-smaller pieces, eventually forming what are known as secondary.[172-174] In addition to mechanical breakdown, their chemical composition also slowly evolves as they are oxidize in earth's atmosphere. While there is little consensus on the exact definition of microplastics, the one published by Frias and Nash is adopted here,[175] in which they comprise “any synthetic solid particle or polymeric matrix, with regular or irregular shape and with size ranging from 1 μm to 5 mm of either primary or secondary manufacturing origin···”.

The chemical and physical properties of microplastics are of significant environmental and ecological concern. The smallest microplastics are readily ingested by both aquatic and terrestrial life. On their own, ingested microplastics are often thought to be of little importance

because they may pass harmlessly through the body.[176] However, numerous recent studies report that microplastics readily sorb and may later release toxic organic substances, thus serving as an efficient vector for their transport.[177-181] Toxic organic pollutants known to be sorbed by microplastics include insecticides and herbicides, polychlorinated biphenyls, perfluorinated compounds, dioxins, furans, polyaromatic hydrocarbons, pharmaceuticals, dyes, and the metabolites and natural degradation products of all of these.[172,180,182,183] The risks of exposure to microplastics and the toxic chemicals they may carry will only grow as plastic waste becomes ever more prevalent in the environment.[176]

Studies of sorption by microplastics are common in the literature.[184-188] Many show that uptake of organic compounds changes as the plastics age.[189,190] Published work includes investigations of the sorption mechanism (i.e., isotherm), strength, and kinetics.[183,185, 191-193] And most have been performed by methods that only provide bulk or heavily averaged results. Few have used microscopic methods that explore the molecular level details of the interactions between organic molecules and microplastic surfaces. As a result, much remains to be learned about how different organics interact with plastic surfaces. For example, it remains unclear whether trace organic pollutants permanently adsorb to specific reactive sites directly from solution or whether they are first weakly associated, diffusing across the surface until they encounter a strong adsorption site. In fact, a broad range of behaviors is expected, depending on the exact chemical structure of the pollutant and the chemistry of the plastic surface. An improved fundamental understanding of the interactions between organic pollutants and both fresh and aged microplastics is ultimately required to fully grasp their environmental, ecological, and health consequences. The implementation of new experimental tools in their study is required to fully address the varied risks they may pose.

Fluorescence imaging microscopy affords a valuable means to detect the sorption of organic molecules by microplastics.[194 -196] However, these methods have not yet been used to probe the full details of the sorption mechanism and its consequences. Namely, data revealing whether the molecules are permanently adsorbed on the plastics or whether they remain mobile are lacking. Again, significantly mechanistic variability is expected depending on the chemical composition of the microplastic surface and the chemical structure of the pollutants in question. For example, some may strongly chemisorb to microplastic surfaces directly from solution at specific reactive sites. Others may form a weakly physiosorbed layer in which the molecules remain associated with the plastic surface but mobile as the surface slowly oxidizes, only later finding a site with the proper chemistry to result in strong physisorption. There remains a complete dearth of information on the mechanisms of molecular interactions with plastic surfaces at this level.

The method of fluorescence correlation spectroscopy (FCS) is particularly well suited to such studies.[71,197,198] FCS involves recording the fluorescence in time as dye molecules diffuse in and out of the diffraction-limited focal volume of a confocal microscope. The time transients thus obtained provide valuable evidence of molecular surface adsorption and molecular diffusion and the means to quantify the diffusion rate. Autocorrelation functions derived from the time transients provide insights into the likely mechanisms of diffusion. Importantly, FCS allows for surface adsorption and diffusion to be explored at trace concentrations similar to those at which pollutants are found in the natural environment.[199]

In this chapter, FCS is used for the first time to study the accumulation and diffusion of rhodamine B (RhB) on the surface of post-consumer and virgin synthetic secondary polyethylene terephthalate (PET) microplastics immersed in water. PET is widely used in drinking water

bottles and disposable food packaging due to its good intrinsic barrier properties.[200] Although PET is considered highly recyclable, it comprises a significant fraction of plastic waste found in the environment.[178] RhB serves as an analogue for toxic organic substances that may accumulate on microplastics in freshwater environments. It was selected for use because it is both water soluble and highly fluorescent, while also incorporating functional groups and heteroatoms (O and N) similar to many organic pollutants, their metabolites, and their degradation products.[201] Dyes like RhB are also known to be released into the environment and to accumulate on microplastics.[183] The present study investigated the interactions of Rhodamine B (RhB) with fresh and artificially aged PET microplastics, including virgin and post-consumer samples. Artificial aging was achieved by exposing the plastics to the reactive atmosphere within a UV-ozone chamber.[190] Chemical characterizations for fresh and aged PET microplastics were obtained from sessile drop water contact angle measurements, atomic force microscopy, and vibrational spectroscopy.

5.2 Materials

Synthetic secondary microplastics were prepared by cutting pieces from two sources: the primary source being virgin biaxially oriented PET plastic sheets (Goodfellow Cambridge), and the other source consisting of post-consumer PET plastic derived from common food packaging materials. The thickness of virgin and post-consumer PET plastics was 100 μm and 250 μm respectively, which both plastics were optically clear and colorless. Pieces ~2 mm × 3 mm in lateral dimension were prepared for ease of handling. In this context, these samples are classified as “synthetic” secondary microplastics because they have been artificially prepared in the lab from larger plastic materials.

The microplastic pieces thus obtained were first cleaned by sonicating for ~10 min in warm soap water. They were next rinsed with copious quantities of deionized (18 MΩ cm) water and subsequently sonicated for an additional ~10 min in warm deionized water. Afterward, they were dried under a stream of nitrogen gas. Fresh microplastics were used as obtained after cleaning. Artificially aged microplastics were prepared by exposing the clean pieces to the reactive atmosphere within a UV-ozone chamber (Novascan Technologies PSD-UVT), providing UV–C (254 nm) illumination at atmospheric pressure and an ambient temperature of 23°C. Plastics were commonly aged for times ranging from 0.5 to 4 min but were sometimes aged as long as 12 min.

5.3 Results and Discussion

5.3.1 Confocal Raman spectroscopy

Confocal Raman spectra were acquired to verify the composition of the PET plastic and to explore any changes in the chemical composition with aging. These data were obtained on a home-built confocal Raman microscope that was constructed upon an inverted light microscope (Nikon TE-300). Raman scattering was induced by directing 1 mW of collimated laser light at 532 nm into the microscope. Within the microscope, the light was reflected from a dichroic mirror (Chroma DCLP 550) and into the back aperture of a high numerical aperture (NA) oil immersion objective (Nikon Apo-TIRF, 100X, 1.49 NA). The objective focused the laser light through the immersion oil, a cover glass, and water to a spot of diffraction-limited size on the sample surface. Each piece of PET sample was held within the cell using a vertically mounted glass capillary. The capillary was used to maintain the microscope's focus on the plastic surface throughout each experiment. The sample was immersed in deionized water and reproducibly positioned ~ 10 ± 2 μm above the microscope coverglass, which separated the microplastic

sample from the immersion oil. The scattered light was collected by the same objective, directed back through the dichroic mirror, and subsequently focused by the internal tube lens of the microscope into a 50 μm diameter pinhole placed in the primary image plane of the instrument. It was then directed through a 532 nm holographic notch filter (Kaiser Optical) and into an imaging spectrograph (Acton Research, 300i). Within the spectrograph, the scattered light was dispersed by a 1200 line/mm diffraction grating and subsequently imaged onto the photosensitive surface of a thermoelectrically cooled, electron-multiplying CCD camera (Andor, Newton DU-970P-BV). The wavelength axis was calibrated using both a neon lamp and literature results for PET plastic Raman scattering.

Raman spectra were acquired by integrating the signal for a total of 25 min. The aforementioned 50 μm pinhole allowed for selective detection of the scattered light with a depth resolution of ~ 825 nm along the laser propagation direction. As the microscope was focused on the surface of the sample, the Raman scattering thus represents the integrated signal from the first ~ 400 nm of depth within the sample. Figure 5.1 shows representative Raman spectra obtained from fresh and artificially aged PET microplastics. Figure 5.1a shows the spectrum of virgin biaxially oriented PET, while Figure 5.1b displays the spectrum of post-consumer PET. Both samples exhibit similar peaks and patterns. The slight noise observed in the post-consumer PET spectrum can be attributed to impurities introduced during packaging preparation. Table 5.1 provides a list of the observed peaks and compares them to results reported in the literature.[202] Vibrational mode assignments for the individual peaks are also provided.

These data confirm that the samples employed are PET plastics. However, this method is not revealed clear changes in the spectra with aging. The challenges in detecting chemical changes are attributed to modification of only a thin surface layer.

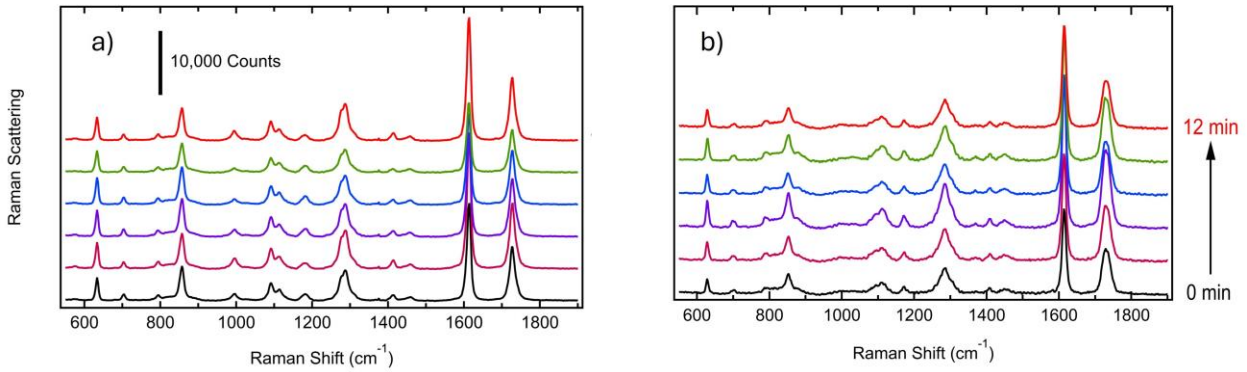

Figure 5.1 Confocal Raman spectra from a) virgin and b) post-consumer synthetic secondary PET microplastics as a function of aging time. The spectra were acquired after 0, 1, 2, 4, 8, and 12-min aging times. The spectrum has been background corrected and offset vertically to better show each spectrum.

Table 5.1 Comparison of Raman spectra obtained from the synthetic secondary PET microplastics being investigated and literature data[202].

Lit. Band (cm^{-1}) [202] and Intensity*	Band (cm^{-1}) and Intensity	Lit. Assignment[202]
1726 – vs	1727 – vs	C=O stretch
1614 – vs	1613 – vs	Ring C=C stretch
1460 – w	1455 – w	Glycol C-H deformation
1416 – w	1413 – w	Ring C-C stretch
1373 – vw	1375 – vw	Gycol CH_2 wagging
------	1312 - w, sh	
1288 – s	1289 – s	Mixed ring-C=O stretch, O-C stretch, ring CH in-plane bend
------	1283 - m, sh	
1184 – w	1181 – m	Ring CH in-plane bend
1115 – m	1112 – m	Mixed ring CH in-plane bend, glycol C-O stretch
1094 – m	1092 – m	Mixed ring CH in-plane bend, glycol C-O stretch, COC and CCO bend, C-C stretch
998 – w	995 – w	Mixed mode glycol C-C stretch, O-CH_2 stretch and ring torsion
893 – w	------	Glycol CH_2 rocking
858 – s	856 – s	Ring C-C breathing
795 – w	795 – w	Ring CH out-of-plane
703 – w	703 – w	Ring C-C-C out-of-plane bend
632 – m	633 – s	Ring C-C-C in-plane bend

*Peak intensity designations: very strong (vs), strong (s), medium (m), weak (w), very weak (vw), shoulder (sh).

5.3.2. Attenuated Total Internal Reflection Infrared Spectroscopy

Diamond-prism based attenuated total internal reflection Fourier transform infrared (ATR-FTIR) spectroscopy was performed on a Cary 630 benchtop FTIR spectrometer (Agilent)

with a single-bounce ATR accessory. Background spectra (64 scans) were acquired with the clean diamond prism exposed to dry nitrogen gas. Sample spectra were acquired under dry nitrogen gas with each PET sample pressed face down over the diamond prism using the built-in pressure clamp. A total of 512 scans were averaged during the collection of the sample spectra. All spectra were acquired at 2 cm^{-1} resolution.

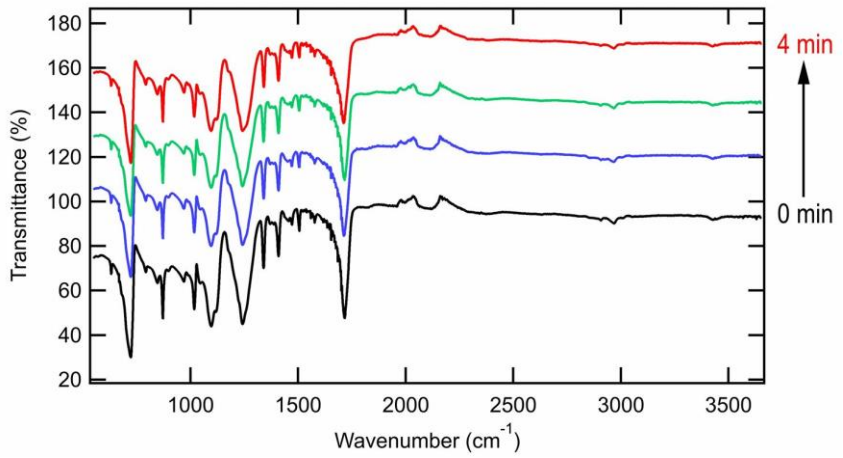

Figure 5.2 ATR-FTIR spectra from virgin PET microplastics. The spectra were acquired under dry nitrogen. The spectra have been vertically offset to better show each one.

Table 5.2 Comparison of ATR-FTIR spectra obtained from fresh synthetic secondary PET microplastics being investigated with literature data.[203]

Lit. Band (cm^{-1})[203] and Intensity*	Band (cm^{-1}) and Intensity	Lit. Assignment[202]
3560 – w	3540 – vw	OH stretch
3440 – w	3427 – w	C=O overtone
3082 – w	3081 – vw	Ring C-H stretch
3055 – w	3057 – vw	Ring C-H stretch
2970 – m	2970 – m	Asymmetric glycol C-H stretch
2908 – m	2907 – w	Symmetric glycol stretch
1724 – vs	1711 – vs	C=O stretch
1504 – mw	1505 – m	Ring stretch
1410 – s	1409 – s	Combination band550
1343 – s	1340 – s	Ring-C=O stretch
1263 – vs	1243 – vs	Carbonyl C-O stretch
1120 – s	1120 – s	Glycol C-O stretch, crystalline
1100 – s	1096 – s	Combination band with glycol C-O stretch, amorphous
1020 – s	1017 – s	Ring C-H in-plane bend
875 – m	871 – s	Ring C-H out-of-plane bend
727&733 – s	723 – vs	Ring C-H out-of-plane bend

*Peak intensity designations: very strong (vs), strong (s), medium (m), weak (w), very weak (vw), shoulder (sh).

Figure 5.2 shows representative ATR-FTIR spectra obtained from fresh and aged virgin PET plastics. Table 5.2 provides a list of selected peaks observed for the PET samples and compares them to results reported in the literature.[203] Vibrational mode assignments for the individual peaks are also provided. Some peaks are excluded from the list due to challenges identifying them in the presence of peaks attributed to residual water vapor. As with the Raman data (Figure 5.1), no clear changes beyond possible variations in peak intensity were observed in the spectra after aging in the UV-ozone chamber for up to 8 min.

5.3.3 Contact Angle Measurements

Sessile drop water contact angle measurements were employed to detect changes in PET surface chemistry with aging which did not reveal Raman and ATR-FTIR experiments. These measurements were made using a home-built droplet imaging apparatus that employed a CCD camera and zoom lens.[146] Freely available software within the ImageJ platform was used to determine the water contact angles from the images obtained.[204] In these measurements, 2.0 μL droplets of deionized water were deposited on each sample and immediately imaged. The results are shown in Figure 5.3 for a series of fresh and aged samples. Both virgin and post-consumer PET plastic exhibit similar trends in hydrophobicity and hydrophilicity. These reveal that the clean, fresh samples are modestly hydrophobic, exhibiting water contact angles of >60°. As the plastics were aged from 0.5 to 4 min, the contact angle gradually dropped to around 30°, reflecting an increase in their hydrophilicity. The contact angle remained approximately unchanged from 4 to 12 minutes of aging, with only a slight decrease observed in post-consumer PET, likely due to impurities introduced during the packaging process. These results are consistent with those from the literature.[205] The enhanced wettability of the aged PET plastic is attributed to the oxidation of its surface.

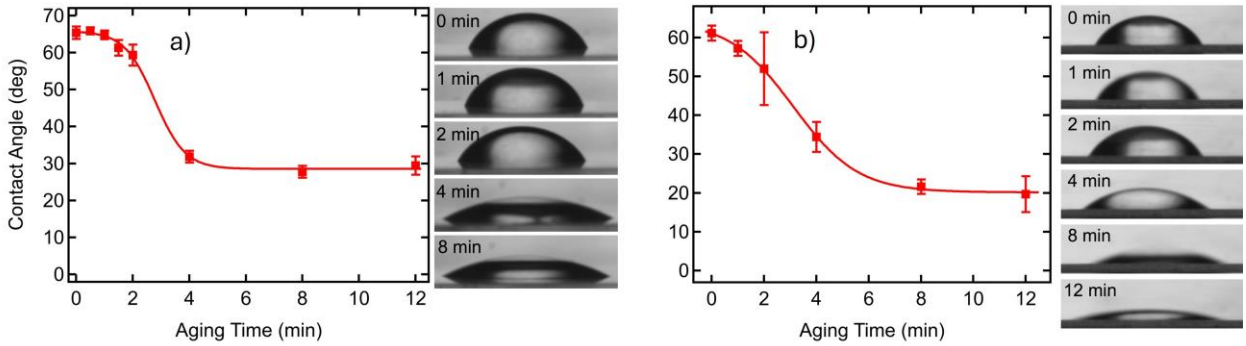

Figure 5.3 Sessile drop water contact angle (filled squares) on a) virgin and b) post-consumer synthetic secondary PET microplastics as a function of the aging time. The solid line has been appended to show the trend in the data. The error bars depict standard deviations from three independent measurements. Representative images of each water droplet are shown on the right. These measurements were conducted by Omid Shafiee.

5.3.4 Intermittent-Contact Mode Atomic Force Microscopy

Changes to the surface of the microplastics with age were further explored by tapping mode atomic force microscopy (AFM). AFM images of the fresh and aged microplastic samples were acquired to further explore the changes to their surfaces upon aging in the UV-ozone chamber. A Digital Instruments Multimode AFM with Nanoscope IIIa electronics was employed in these studies. Intermittent-contact mode imaging was employed using conical probes (NanoScience Instruments, Aspire) mounted to cantilevers having a resonance frequency of 170 kHz and a spring constant of 50 N/m. For each sample, a minimum of three images of different sample regions ~ 4-5 μm square in size and separated by several hundred microns were acquired. Images were obtained for both fresh samples and those aged. Figures 5.4 and 5.5 show images of post-consumer and virgin PET microplastic samples, respectively, illustrating their appearance over different aging times. Figure 5.6 plots the mean RMS roughness of post-consumer and virgin PET microplastics as a function of aging time derived from these images and their replicates.

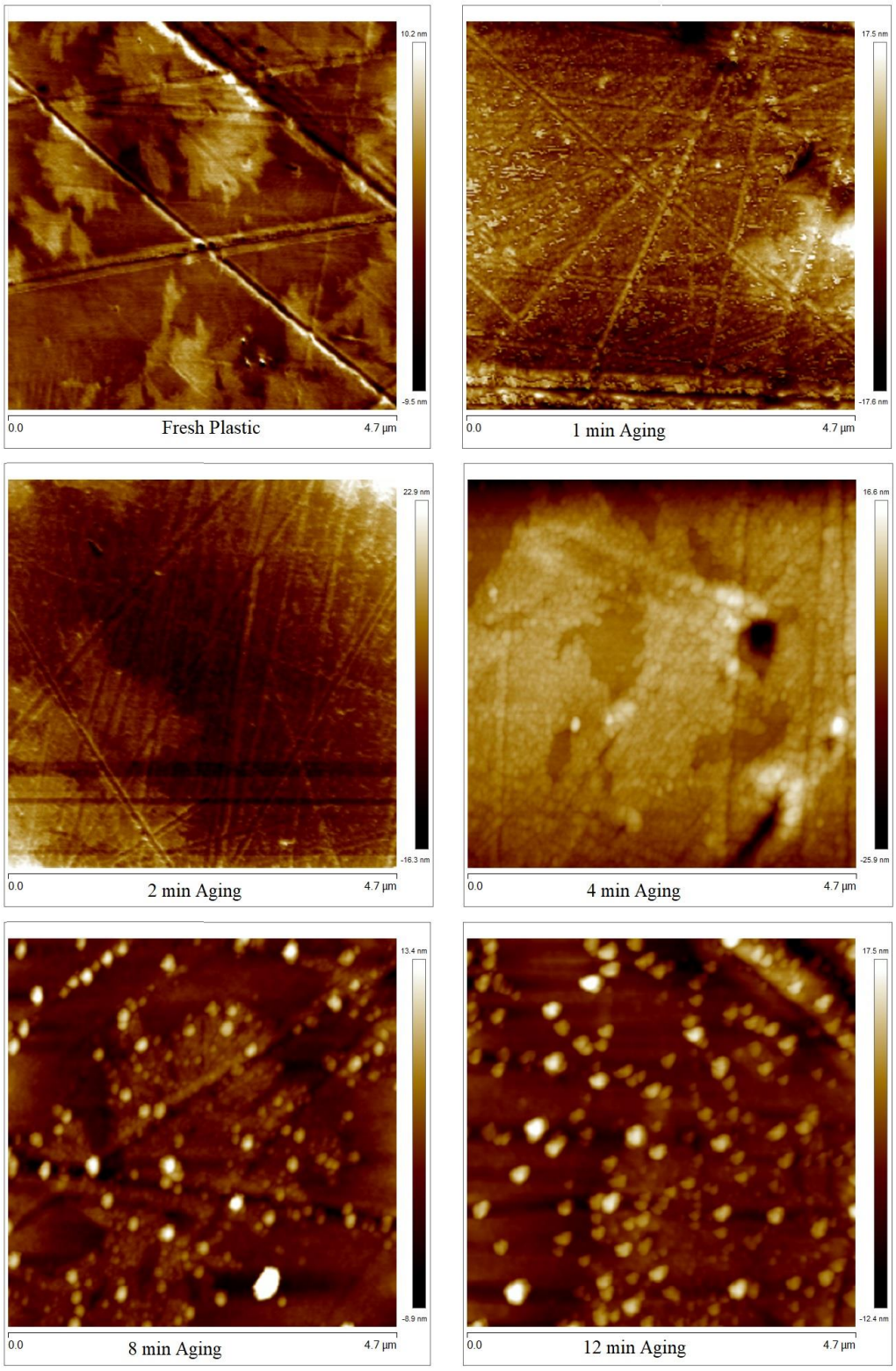

Figure 5.4 Intermittent-contact mode AFM images of the post-consumer PET microplastic surfaces for fresh, 1,2,4,8 and 12 min artificially aged samples.

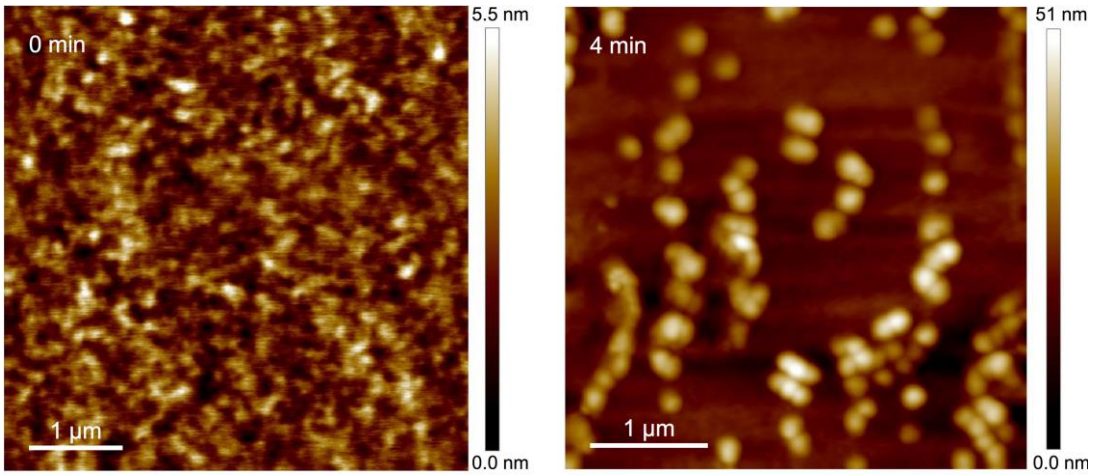

Figure 5.5 Representative intermittent-contact mode AFM images of the virgin PET microplastic surfaces for both fresh and 4 min artificially aged samples. These images were collected by Omid Shafiee.

The average RMS roughness determined over ~20 μm^2 regions of samples and the results for post-consumer PET microplastics are not show the clear trends (see Figure 5.6b), while the virgin PET microplastics reveal the average RMS roughness of 1 nm for fresh samples, with roughness growing to ~7 nm for samples aged for 2 min or longer. Images of the fresh samples revealed small irregular features, while the aged samples were dominated by larger round protrusions. Linear features a few nanometers deep are also occasionally observed in all samples; these are attributed to the manufacturing process. The observed changes in the surface are similar to those reported previously for PET plastic aging.[206,207] The chemical composition of the protrusions that appear with aging have been attributed to oxidized polymer in the past.[206]

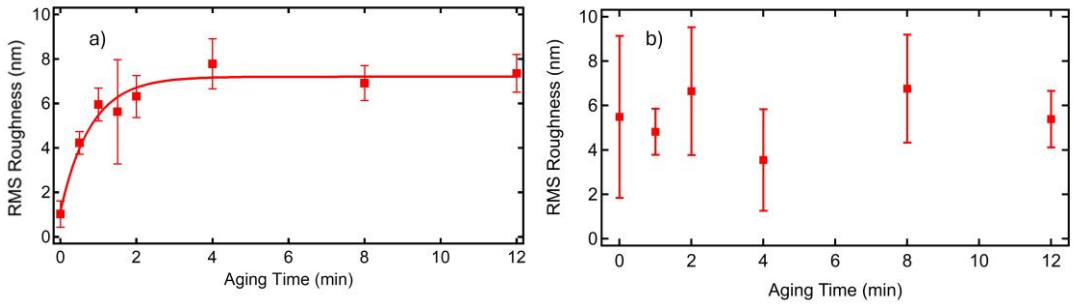

Figure 5.6 The mean RMS roughness for both fresh and artificially aged samples of a) Virgin and b) Post-consumer PET microplastics was derived from the AFM images shown in Figures 5.4 and 5.5, as well as their replicates (not shown). RMS roughness values were calculated across the entire image area (~20 μm²) in each case. Error bars represent the standard deviations for each measurement, and the solid line is included to indicate the overall trend**.**

5.3.5 Fluorescence Correlation Spectroscopy (FCS)

FCS experiments were conducted on a confocal fluorescence microscope that has been described previously, in detail.[160] This instrument is built upon an inverted light microscope (Nikon TE-200). Fresh and aged microplastic samples were placed in a glass cell that was mounted above the oil immersion objective (Nikon Plan Fluor, 100X, 1.3 NA). The samples were immediately immersed under deionized water containing 5 nM RhB. The bottom surface of the cell comprised a microscope coverslip (FisherFinest Premium) through which all optical measurements were made. Although PET plastic has a density of 1.30–1.40 g/cm^3,[208] it was necessary to hold each piece in place within the cell using a vertically mounted glass capillary. The capillary was used to ensure that the microscope focus was maintained on the plastic surface throughout each experiment. It also helped to avoid variations in the detection volume caused by optical aberrations when focusing at different depths above the coverslip. [95,101,127]

RhB fluorescence was excited by 2.5 μW and 10 μW (measured prior to entry into the microscope) samples of 532 nm laser light for virgin and post-consumer respectively. Upon entering the microscope, the laser light was first reflected from a dichroic beam splitter (Chroma 550 DCLP) and then directed into the back aperture of the aforementioned objective.

Fluorescence emitted by the dye was collected by the same objective and was subsequently passed back through the dichroic beamsplitter and into the detection path of the microscope. The collected fluorescence was next directed through a 50 μm diameter pinhole placed in the primary image plane of the microscope. Upon emerging from the pinhole, the fluorescence was collected and refocused via a pair of achromatic lenses through a bandpass filter (Chroma, 580/40m) and onto the photosensitive element of a single-photon-counting avalanche photodiode (APD). Pulses from the APD were counted using a counter/timer board operated in the time-stamping mode.[126] Time transients of arbitrary time resolution ranging from 1 μs to ~10 s were obtained from the time-stamping data using C++ code written in house.

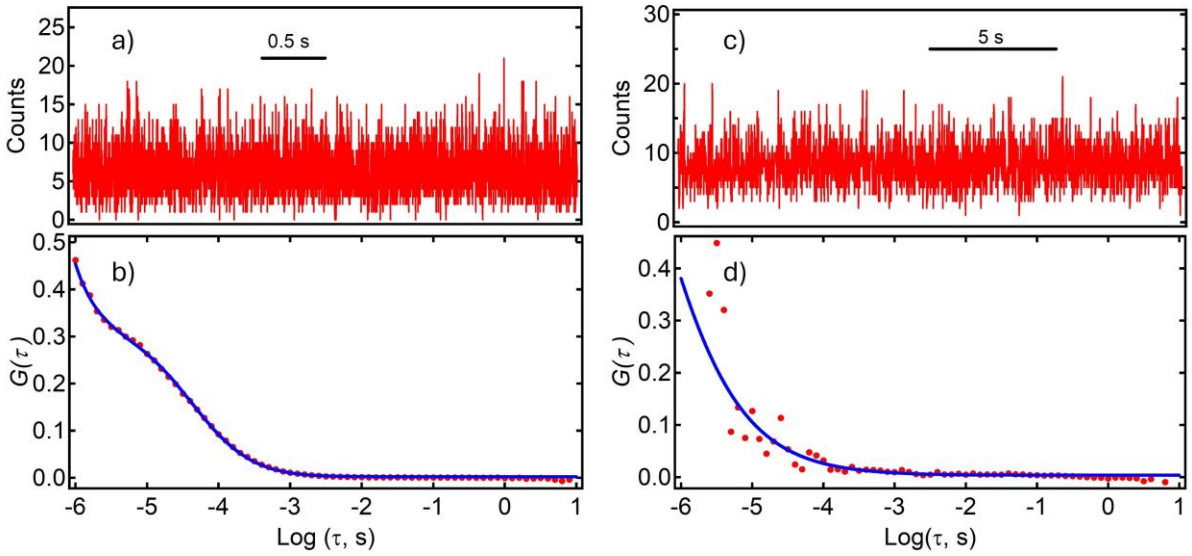

Figure 5.7 a) Time transient segment showing the fluorescence signal fluctuations observed at 1 ms time resolution for 5 nM RhB in aqueous solution. The incident laser power at 532 nm was 10 μW. b) Average autocorrelation function (red dots) obtained from ten replicate measurements, and it fits the appropriate analog of Eq. 5.2 for free Fickian diffusion in three dimensions. c) Time transient segment showing background counts observed at 10 ms time resolution from a fresh microplastic surface in the absence of RhB. The incident laser power at 532 nm was 2.5 μW. d) Average autocorrelation function (red dots) obtained from ten replicate measurements, and it's fit to Eq. 5.2.

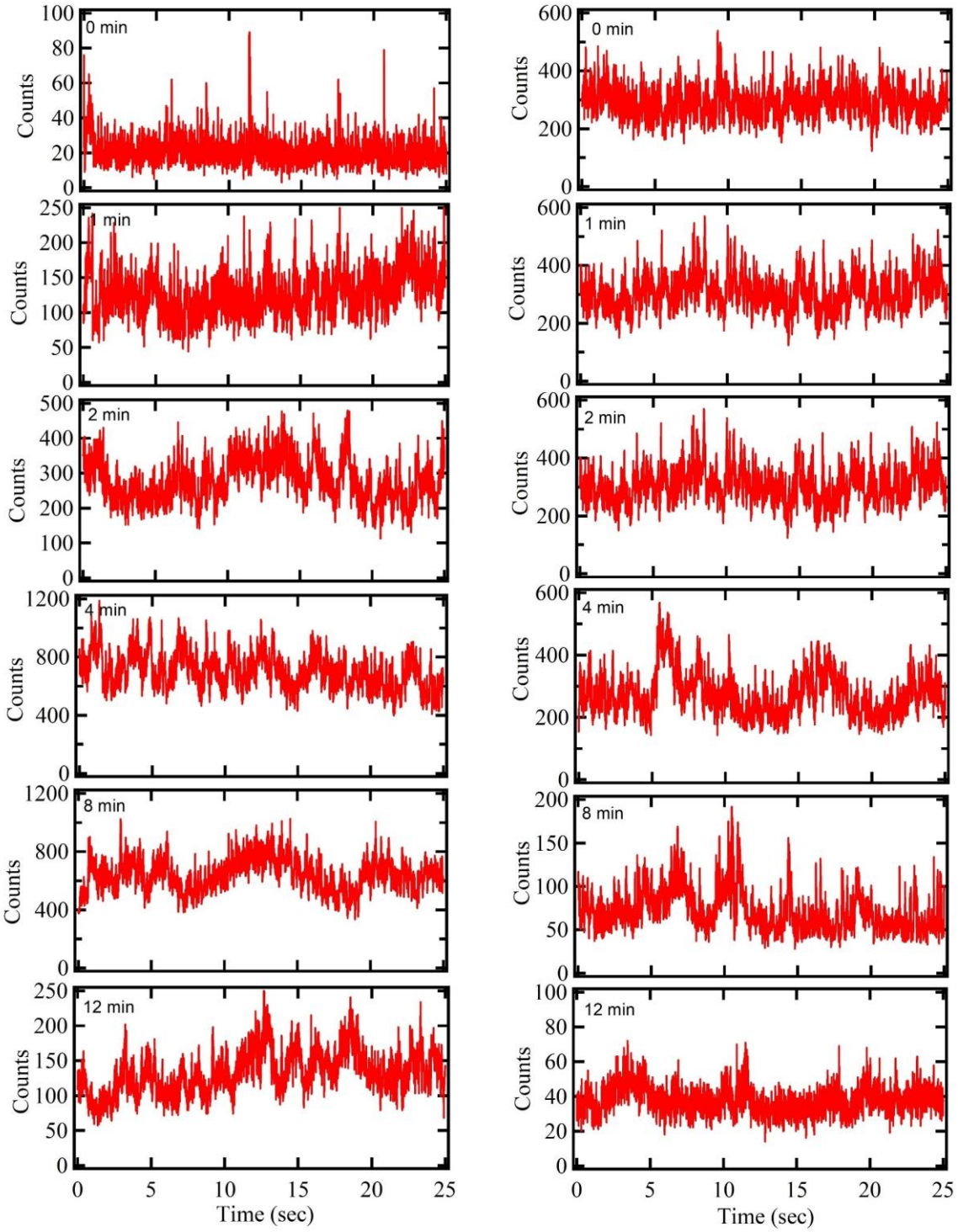

Figure 5.8 Fluorescence time transient segments (counts per 10 ms) acquired from virgin (left column) and post-consumer (right column) PET microplastics as a function of aging time on a confocal fluorescence microscope. The fluctuations are due to passage of surface-associated RhB dye through the confocal detection region.

Figure 5.8 shows representative fluorescence time transients obtained when the microscope was focused on the microplastic surface in a 5 nM RhB solution. These show significant fluctuations in the fluorescence from the plastic surface occurring on tens of milliseconds and longer time scales. In contrast, similar fluorescence time transients acquired from bulk solution 5 μm below the microplastic surface show much weaker fluctuations that occur on submillisecond time scales, as expected for free solution-phase RhB diffusion as shown in Figure 5.7a. Background fluorescence obtained from the microplastic surfaces in the absence of dye was negligible when compared to that of all but fresh plastic samples as shown in Figure 5.7c. These observations are consistent with adsorption and relatively slow diffusion of the dye across the microplastic surface. PET plastics are known to be glassy and nonporous.[209] As such, significant sorption of the dye within PET plastics is not expected to occur.

Figure 5.9 plots representative mean autocorrelation decays obtained from the surfaces of fresh and aged PET microplastics in the presence of 5 nM aqueous RhB. The autocorrelation functions were obtained by averaging results from several (i.e., ∼30) individual data sets. These were subsequently normalized to their mean values between τ = 5–15 μs to best reveal the monotonic increase in decay times observed as the plastics were aged. The trend is consistent with the slowing of the dye diffusion. The fast decay around 10^{-6} s may be due to triplet blinking of the dye[129] and is irrelevant to these studies.

The autocorrelation decays were fit in order to deduce the nature of the diffusion mechanism and to quantitatively determine the diffusion time. The decays were found to fit well to Eq 5.2, which approximately models anomalous two-dimensional diffusion.[210]

$$\boldsymbol{G(\tau) = A + \frac{B}{\left(1+\left(\tau/\tau_D\right)^{\alpha}\right)}} \qquad 5.1$$

In Eq 5.2, A represents a constant offset in the autocorrelation function and is usually very close to zero, B the amplitude of the diffusive decay, τ_D the diffusion time, and α the coefficient of anomalous diffusion, with $\alpha = 1$ for Fickian diffusion, $\alpha < 1$ for anomalous subdiffusion, and $\alpha > 1$ for anomalous superdiffusion. Figure 5.9b,d depicts a representative fit (solid blue line) of autocorrelation decay data (red dots) to Eq 5.2. All autocorrelation decays were fit from 10^{-5} to 1s, with the fits plotted from 10^{-6} to 2.5 s. The fitting residuals are plotted in the lower part of Figure 5.9b,d and reveal the fitted curves deviates from the experimental data by <5% over the majority of the fitted range.

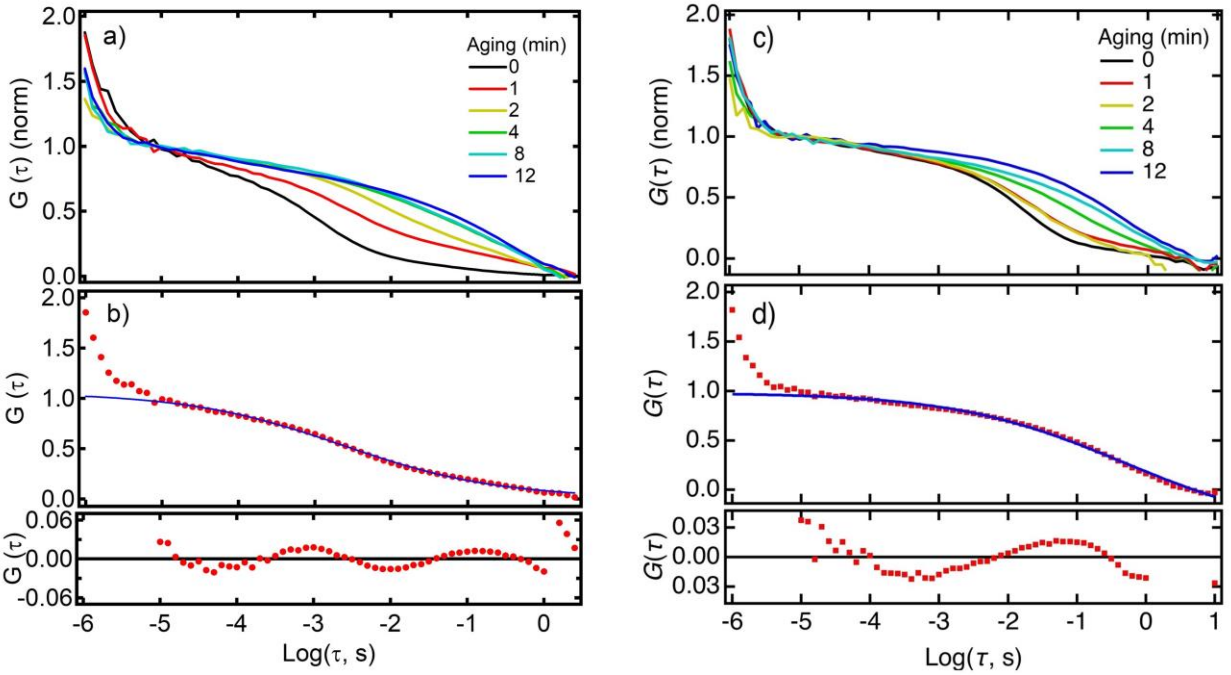

Figure 5.9 a) Autocorrelation decays obtained from RhB diffusion on the surface of virgin PET microplastics as a function of aging time. b) Representative fit (top, blue line) of autocorrelation data (red dots) for a 1 min aged sample to Eq 5.2 from 10^{-5} to 1 s and the fitting residuals (bottom, red dots). c) Autocorrelation decays obtained from RhB diffusion on the surface of post-consumer PET microplastics as a function of aging time. d) Representative fit for 4 min aged post-consumer plastics same as described in part b. The autocorrelation data in (a) and (d) have been normalized based on $G(\tau)$ from $\tau \sim 5$–15 μs to better show the trend in the data.

The usual assumption in FCS experiments is that $G(0) = 1/N$, where N is the mean number of molecules in the detection volume. [98,99] Unfortunately, this assumption is not strictly valid in the presence of immobile, surface adsorbed molecules.[162] Furthermore, the sharp rise and poor signal-to-noise ratio in $G(\tau)$ near $\tau \sim 10^{-6}$ s (see Figure 5.9) make estimation of *G(0)* challenging. Nevertheless, a semiquantitative assessment based on the (unnormalized) autocorrelation decays for virgin microplastics from several replicate experiments reveals that $1/G(0) \sim 5$ for RhB on fresh plastic and $1/G(0) \sim 20$ on 4 min aged plastic, consistent with increased RhB adsorption as the samples are aged. The latter value corresponds to an approximate surface density of 3.6×10^{10} molecules/cm^2. This value represents an upper bound estimate of the actual surface coverage of mobile molecules and is ~0.03% of a monolayer, assuming 1 molecule/nm^2 represents a complete monolayer.

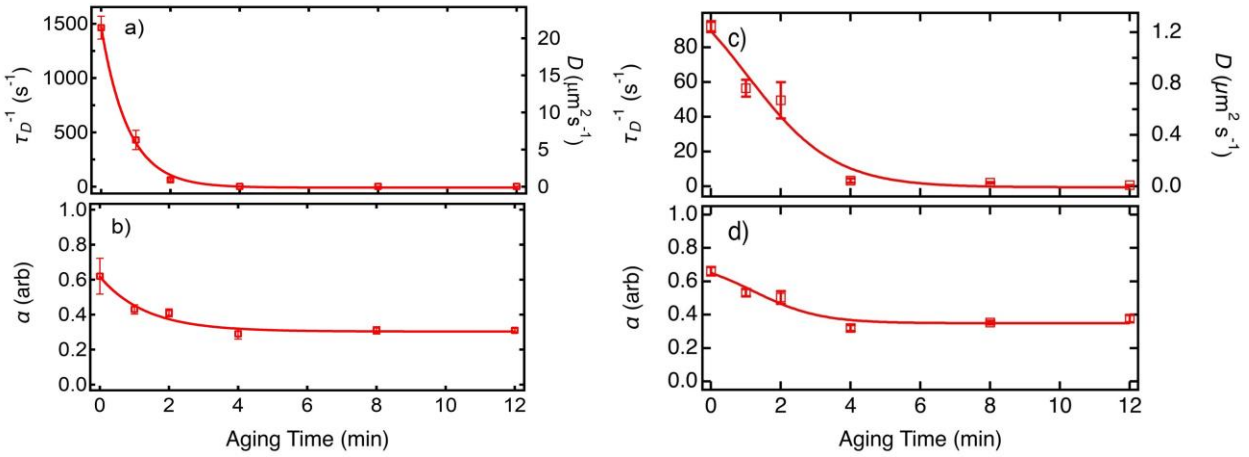

Figure 5.10 a) Mean rate of diffusion (τ_D^{-1}) and mean diffusion coefficient, *D*, as a function of aging time for virgin microplastics. b) Mean coefficient of anomalous diffusion as a function of aging time for virgin microplastics. c) and d) present similar data as in (a) and (b), respectively, but for post-consumer microplastics. The data plotted were obtained by fitting the autocorrelation decays to Eq 5.2. The error bars depict 95% confidence intervals determined from ~90 replicates. Data at 0, 1, 2, 4, 8 and 12 min aging represent averages from three independent experiments, while the others were repeated twice.

Figure 5.10a and b plot mean τ_D^{-1} and α values, as well as the mean diffusion coefficient, *D*, as a function of aging time for virgin microplastics. Similarly, Figure 5.10c and d show the same parameters plotted for post-consumer microplastics. These figures provide insight into the diffusion behavior as a function of aging for both types of microplastics. Here, $D = w^2/4\tau_D$, where w^2 is the calibrated detection area.[160] The mean *D* value for surface-associated RhB on fresh PET microplastics is approximately 20 times smaller for virgin PET and about 300 times smaller for post-consumer PET compared to its diffusion in bulk solution.[160] This significant reduction indicates that the interactions between RhB and the PET surface greatly slow down the dye's mobility, especially in post-consumer PET. In both cases, the rate of diffusion decreases significantly as the plastics undergo aging. After 4 minutes of aging, the *D* becomes approximately 8000 times smaller than in bulk solution, and this value remains unchanged mainly beyond this point, indicating a stabilization in the reduction of RhB's mobility on the aged plastic surfaces. In addition, the mean α values reveal that RhB motion occurs via anomalous subdiffusion. Furthermore, α becomes smaller as the plastics are aged.

5.4 Conclusions

Taken together, the evidence for surface oxidation provided by the water contact angle data and AFM images, the increase in concentration of surface-associated dye, and the dramatic slowing of RhB diffusion reflect greatly enhanced interactions between the dye and the plastic surface with increased age. The observed changes could arise from either enhanced ionic interactions between the charged RhB dye and anionic surface sites or enhanced hydrogen bonding between the dye and surface-associated hydrogen bonding sites. The exact chemical nature of these interactions will be addressed in future work.

The results presented here demonstrate that RhB molecules adsorbed on the surface of fresh PET microplastics remain mobile, consistent with weak surface association. The concentration of surface-associated molecules increases dramatically as the plastics age, while their mobility decreases precipitously, consistent with much stronger interactions between the dye and the oxidized surface. A more detailed understanding of these phenomena is required to properly assess the risks of exposure to microplastics and the toxic organic substances that they accumulate and transport.

Chapter 6 - General Conclusions and Future Directions

6.1 General Conclusions

This dissertation employed fluorescence correlation spectroscopy (FCS) methods to investigate the rates and mechanisms of Rhodamine B (RhB) diffusion within nanopores of anodic alumina (AAO) membranes filled with various ethanol/water mixtures and at the PET microplastic surface at fresh and different aging times under doped RhB water solutions.

The experiments were conducted as a function of pore size, using AAO membranes with 10, 20 and 30 nm cylindrical pores and solvent composition ranging from pure ethanol and water/ethanol mixtures through pure water. The autocorrelation plots obtained from FCS experiments inside the AAO membranes fit well to a one-dimensional (1D), two-component model. This revealed the existence of two distinct diffusion mechanisms for RhB confined within the nanopores, which were interpreted as fast and slow one-dimensional diffusion processes. Both diffusion coefficients (fast and slow) were significantly smaller than the bulk diffusion coefficient in solutions of the same composition. The slow diffusion process produced 10-100 times smaller values than faster ones. Both diffusion mechanisms showed strong dependencies on pore size and solvent composition but in distinctly different ways.

The fast diffusion coefficient closely mimicked the behavior of bulk solutions, and were consistent with viscosity-dependent Brownian motion within the nanopores. This motion has the highest value in the pure solvents and the smallest in the mixtures with intermediate ethanol content. The reduction of this mechanism compared to the bulk solution was attributed to increased hydrodynamic drag, likely caused by a stagnant solvent layer near the pore walls, as well as long-range electrostatic interactions between the charged RhB molecules and oppositely charged sites on the pore surfaces.

In contrast, the slow diffusion mechanism showed different behaviors and trends compared to the fast diffusion mechanism. The diffusion coefficient in this case was smallest in the pure solvents and largest in mixtures with intermediate ethanol content. It was concluded that reversible adsorption of RhB to the pore surfaces, driven by electrostatic interactions or hydrogen bonding between the dye and surface hydroxides, dominated the observed slow diffusion. These interactions may be moderate in mixtures with higher water content due to the formation of a water layer on the pore surfaces.

The density of adsorbed RhB, indicated by the autocorrelation amplitude and the apparent slow diffusion coefficient, showed clear correlations with RhB solubility across the full range of solvent compositions. Adsorption was most pronounced in pure ethanol and pure water, where RhB solubility was lowest, while diffusion was more significant in intermediate ethanol/water mixtures where the dye was more soluble. The contribution of slow diffusion to the autocorrelation amplitude showed the highest values in pure solvent and the smallest in the intermediate mixtures.

Slow diffusion became more pronounced in the 10 nm nanopores compared to the 20 and 30 nm pores, suggesting that smaller pore size significantly influences diffusion dynamics under nanoconfinement while this dependency diminishes for larger pore sizes. This likely increased the frequency of dye-pore collisions, indicating that surface interactions may be a crucial factor in RhB transport.

Overall, these experimental results for AAO membranes demonstrate that both dye-pore collisions and solvation-dependent surface adsorption play critical roles in governing RhB diffusion in solvent mixtures under nanoconfinement. These insights have significant practical implications, aiding in the development of nanoporous membrane-based separations, especially

in solvent mixtures where optimizing membrane permeability and separation selectivity is particularly challenging.

In the PET microplastic research, evidence of surface oxidation was obtained from water contact angle measurements and AFM images, along with an increased concentration of surface-associated dye and a marked slowing of RhB diffusion. These findings indicate that the interactions between the dye and the plastic surface strengthen as the microplastics age. The observed changes likely arise from enhanced ionic interactions between the charged RhB dye and anionic surface sites or stronger hydrogen bonding between the dye and surface-associated functional groups.

The results show that RhB molecules adsorbed on the surface of fresh PET microplastics remain relatively mobile, suggesting a weak surface association. However, as microplastics age, the concentration of surface-bound molecules rises sharply while their mobility decreases significantly. This indicates stronger interactions between the dye and the increasingly oxidized surface over time.

6.2 Future Directions

The remarkable properties of AAO membranes make them highly versatile, with potential applications in fields such as filtration, catalysis, sensing, and drug delivery. To fully harness these advantages, conducting in-depth studies that investigate how molecular behavior changes when confined within nanopores, particularly in different environments and with various solutes, is essential.

One interesting avenue for future research is nanoconfinement in water/propanol mixtures near azeotrope points. Given our observations of increased fast diffusion in water/ethanol mixtures containing approximately 2% water content within the membrane which

is near the azeotrope point and the absence of a solid explanation for this behavior, exploring whether a similar phenomenon occurs in the water/propanol mixture—which also forms an azeotrope—may provide valuable insights into solvent behavior under confinement. This research could provide insights into how solutes, particularly dyes or other molecules, behave when nanoconfined in environments where phase behavior plays a key role. Understanding this could be vital for optimizing separation processes, particularly in chemical engineering and environmental applications.

Next, the effect of ionic strength and probe charges is another crucial variable to investigate, which is the effect of ionic strength in solution and how different charged probe molecules (neutral, positive, and negative) behave within the nanopores. Ionic strength influences electrostatic interactions between the solute and the pore walls, altering diffusion rates, adsorption phenomena, and molecular mobility. Studying the behavior of neutral, positively charged, and negatively charged probes can gain valuable insights into how charge interactions impact molecular confinement and transport.

Another possible study is the diffusion mechanisms of different dyes in surface-modified AAO membranes. AAO membranes can be chemically modified to alter their surface properties, such as charge, hydrophilicity, or functional group attachment. Exploring how these surface modifications affect the diffusion of different dye molecules can reveal critical details about solute-pore interactions. For instance, surface modifications can either enhance or hinder the movement of certain dyes, depending on factors like electrostatic attraction, hydrophobicity, or steric hindrance. A detailed study of these interactions could contribute to optimizing membranes for dye separation, pollutant removal, or molecular sensing applications, where precise control over solute behavior is crucial.

Understanding how nanoconfinement influences molecular behavior, particularly in complex solvent mixtures or with varying surface charges, can open new possibilities for engineering AAO membranes for specialized applications. This could include the development of highly selective filtration membranes for use in industrial separations, the design of advanced sensors capable of detecting specific molecules in environmental monitoring, or the creation of tailored drug delivery systems that control the release of therapeutics at a nanoscale level.

By studying AAO membranes in such diverse conditions and with varying molecular probes, it can gain a comprehensive understanding of the diffusion mechanisms and interactions that govern molecular transport under nanoconfinement. This will help unlock the full potential of AAO membranes for real-world applications.

References

1. Kockmann, N. Distillation Fundamentals and Principles, **2014**, 1-43.

2. Grimes, S. Secrets of the God Makers: Re-Thinking the Origins of Greco-Egyptian Alchemy. *Syllecta Classica*. **2018**. *29*(1), 67-89.

3. Timothy, C. F.; Bruce S. H. Industrial Chemical Separation Historical Perspective, *Fundamentals, and Engineering Practice*. **2003**, 23-48.

4. Yan, L.; Hong S.; Li ML.; Li YS. Application of the Al2O3–PVDF nanocomposite tubular ultrafiltration (UF) membrane for oily wastewater treatment and its antifouling research. *Separation and Purification Technology*. **2009**, *66* (2), 347–352.

5. Al Aani, S.; Mustafa, T. N.; Hilal, N. Ultrafiltration membranes for wastewater and water process engineering: a comprehensive statistical review over the past decade. *J Water Process Eng*. **2020**, *35*, 101241.

6. Drewes, J. E.; Reinhard, M.; Fox, P. Comparing microfiltration-reverse osmosis and soil-aquifer treatment for indirect potable reuse of water. *Water Research*. **2003,** *37* (15), 3612-3621.

7. Qi, L.; Li, B.; Wang, H.; Cheng, R.; Zeng, F.; Zheng, X. Effect of aeration on the critical flux of immersed ultrafiltration membrane for drinking vwater treatment. *International conference on remote sensing, environment and transportation engineering*. **2011** Proc. no. 50808051 3116–3119.

8. Ahn, K. H.; Song, K. G. Treatment of domestic wastewater using microfiltration for reuse of wastewater. *Desalination.* **1999**, *126*, 1, 7-14.

9. Ismail, A. F.; Matsuura, T. Membrane technology for water and wastewater treatment, *energy and environment.* **2016**, ISBN9780429225673, 171–192.

10. Meng, S.; Zhang, M.; Yao, M.; Qiu, Z.; Hong, Y.; Lan, W.; Xia, H.; Jin, X. Membrane Fouling and Performance of Flat Ceramic Membranes in the Application of Drinking Water Purification. *Water*. **2019**, *11*, 2606.

11. Pozderović, A.; Moslavac, T.; Pichler, A. Concentration of aqueous solutions of organic components by reverse osmosis: II. Influence of transmembrane pressure and membrane type on concentration of different alcohol solutions by reverse osmosis. *J Food Eng.* **2006**, *77*(4), 810–817.

12. Ozcan, A.; laudio Perego, C.; Salvalaglio, M.; Parrinello, M.; Yazaydin, O. Concentration gradient driven molecular dynamics: a new method for simulations of membrane permeation and separation. *Chem Sci*. **2017**, *20*, 8(5), 3858–3865.

13. Sarkar, B. Enhanced cross-flow ultrafiltration of apple juice using electric field. *J. Food Process.* **2014**, *39*, 1372–1384.

14. Mokhtar, G.; Naoyuki, F. Microfiltration, nano-filtration and reverse osmosis for the removal of toxins (LPS endotoxins) from wastewater. *J Membr Sci Technol*. **2012**, *2*, 3.

15. Jedidi, I.; Cretin, M.; Cerneaux, S.; AL Saidi, M.S.; Al- Isaee, S.; Cot, D.; Abdelmouleh, M. Detailed manufacturing process of a tubular carbon microfiltration membrane for industrial wastewater treatment. *J Porous Mater*. **2022**, *29*, 291–306.

16. Moresi, M.; Ceccantoni, B.; Presti, S. Lo. Modelling of ammonium fumarate recovery from model solutions by nanofiltration and reverse osmosis. *J Memb Sci.* **2002**, *209* (2), 405–420.

17. Belkacem, M.; Bekhti, S.; Bensadok, K. Groundwater treatment by reverse osmosis. *Desalination*. **2007**, *206* (13), 100–106.

18. Mohamed, M. G.; El-Mahdy, A. F. M.; Kotp M. G.; Kuo, S. W. Advances in porous organic polymers: syntheses, structures, and diverse applications. *Mater. Adv*, **2022**, *3*, 707–733.

19. Song, Y.; Zhu C.; Ma, S. Advanced porous organic polymer membranes: Design, fabrication, and energy-saving applications. *EnergyChem*. **2022**, *4*, 100079.

20. Kayvani Fard, A.; McKay, G.; Buekenhoudt, A.; Al Sulaiti, H.; Motmans, F.; Khraisheh, M.; Atieh, M. Inorganic Membranes: Preparation and Application for Water Treatment and Desalination. *Materials (Basel)*, **2018,** *5*, 11(1),74.

21. Pera-Titus, M. Porous Inorganic Membranes for CO2 Capture: Present and Prospects. *Chem. Rev*. **2014**, *114*, 2, 1413–1492.

22. Laîné, J. M.; Vial, D.; Moulart, P. Status after 10 years of operation: overview of UF technology today. *Desalination*, **2000**, *131* (1–3), 17–25.

23. Thommes. M.; Kaneko, K.; Neimark, A.V.; Olivier, J.P.; Rodriguez-Reinoso, F.; Rouquerol, J.; Sing, K. S.W. Physisorption of gases, with special reference to the evaluation of surface area and pore size distribution (IUPAC Technical Report). *Pure Appl. Chem*. **2015,** *87* (9-10), 1051–1069.

24. Wang, X.; Chen, Y.; Zhou, Z.; Yang, Y.; Li, X. Three-dimensional type multi-spinning-nozzle spinneret plate for electrospinning. China, **2014**, Patent No. CN203451652U.

25. DuChanois, R. M.; Epsztein, R.; Trivedi, Janvi A.; Elimelech, M. Controlling pore structure of polyelectrolyte multilayer nanofiltration membranes by tuning polyelectrolyte-salt interactions. *Journal of Membrane Science*, **2019**, *581*, 413-420.

26. Deen, W.M. Hindered transport of large molecules in liquid-filled pores. *AIChE J.* **1987**, *33*,14091425.

27. Bowen, W.R.; Mohammad, A.W. Characterization and prediction of nanofiltration membrane performance—a general assessment. *Chemical Engineering Research and Design*. **1998**, *76*, 885893.

28. Cheng, W.; Liu, C.; Tong, T.; Epsztein, R.; Sun, M.; Verduzco, R.; Ma, J.; Elimelech, M. Selective removal of divalent cations by polyelectrolyte multilayer nanofiltration membrane: role of polyelectrolyte charge, ion size, and ionic strength, *J. Membr. Sci.* **2018**, *559*, 98–106.

29. Yaroshchuk, A.E. Non-steric mechanisms of nanofiltration: superposition of Donnan and dielectric exclusion, *Separ. Purif. Technol*. **2001**, *22*, 143–158.

30. Epsztein, R.; DuChanois, R. M.; Ritt, C.L.; Noy, A.; Elimelech, M. Towards single species selectivity of membranes with subnanometre pores. *Nat Nanotechnol.* **2020**, *15*, 426–436.

31. Cassady, H.J.; Cimino, E.C.; Kumar, M.; Hickner, M. A. Specific ion effects on the permselectivity of sulfonated poly (ether sulfone) cation exchange membranes, *J. Membr. Sci*. **2016**, *508*, 146–152.

32. Patel, D. C.; Luo, R.G. Protein adsorption dissociation constants in various types of biochromatography. *Studies in Surface Science and Catalysis*. **1999**, *120*, 829-845.

33. Krishna, R. Uphill diffusion in multicomponent mixtures. *Chem. Soc. Rev.* **2015**, *44*, 2812-2836.

34. Alba-Simionesco, C.; Coasne, B.; Dosseh, G.; Dudziak, G.; Gubbins, K. E.; Radhakrishnan, R.; Sliwinska-Bartkowiak, M. Effects of Confinement on Freezing and Melting. *J. Phys.: Condens. Matter*. **2006**, *18*, R15−R68.

35. Thompson, W. H. Solvation Dynamics and Proton Transfer in Nanoconfined Liquids. Annu. Rev. *Phys. Chem.* **2011**, *62*, 599−619.

36. Durand, N. F. Y.; Dellagiacoma, C.; Goetschmann, R.; Bertsch, A.; Märki, I.; Lasser, T.; Renaud, P. Direct Observation of Transitions Between Surface-Dominated and Bulk Diffusion Regimes in Nano channels. *Anal. Chem.* **2009**, *81*, 5407−5412.

37. Mhanna, R.; Catrou, P.; Dutta, S.; Lefort, R.; Essafri, I.; Ghoufi, A.; Muthmann, M.; Zamponi, M.; Frick, B.; Morineau, D. Dynamic Heterogeneities in Liquid Mixtures Confined in Nanopores. *J. Phys. Chem. B* **2020**, *124*, 3152−3162.

38. Phan, A.; Cole, D. R.; Striolo, A. Preferential Adsorption from Liquid Water−Ethanol Mixtures in Alumina Pores. *Langmuir*. **2014**, *30*, 8066−8077.

39. Guo, X.-Y.; Watermann, T.; Sebastiani, D. Local Microphase Separation of a Binary Liquid under Nanoscale Confinement. J. Phys. Chem. B **2014**, *118*, 10207−10213.

40. Rao, M. B.; Sircar, S. Liquid-Phase Adsorption of Bulk Ethanol Water Mixtures by Alumina. Adsorpt. *Sci. Technol*. **1993**, *10*, 93−104.

41. Elamin, K.; Jansson, H.; Kittaka, S.; Swenson, J. Different Behavior of Water in Confined Solutions of High and Low Solute Concentrations. *Phys. Chem. Chem. Phys*. **2013**, *15*, 18437−18444.

42. Tsuru, T.; Kondo, H.; Yoshioka, T.; Asaeda, M. Permeation of Nonaqueous Solution through Organic/Inorganic Hybrid Nano porous Membranes. *AIChE J.* **2004**, *50*, 1080−1087.

43. Fowlkes, J. D.; Collier, C. P. Single-Molecule Mobility in Confined and Crowded Femtolitre Chambers. *Lab Chip.* **2013**, *13*, 877−885.

44. Varol, H. S.; Kaya, D.; Contini, E.; Gualandi, C.; Damiano Genovese, D. Fluorescence methods to probe mass transport and sensing in solid-state nanoporous membranes. *Mater. Adv.* **2024**, *5*, 8351-8383.

45. Konev, D. V.; Istakova, O. I.; Vorotyntsev, M. A. Electrochemical Measurement of Interfacial Distribution and Diffusion Coefficients of Electroactive Species for Ion-Exchange Membranes: Application to Br2/Br- Redox Couple. *Membranes (Basel)*. **2022**, *26*, 12(11), 1041.

46. Laucirica, G.; Terrones, Y. T.; Cayon, V.; Cortez, M. L.; Toimil-Molares, M. E.; Trautmann, C.; Marmisolle, W.; Azzaroni, O. Biomimetic solid-state nanochannels for chemical and biological sensing applications. *Trends in Analytical Chemistry*. **2021**, *144*, 116425.

47. Oldham, K. B.; Zoski, C. G.; Chapter 2 Mass Transport to Electrodes. *Comprehensive Chemical Kinetics.* **1986**, *26*, 79-143.

48. Liu, X.; Cheng, S.; Liu, H.; Hu, S.; Zhang, D.; Ning, H. A Survey on Gas Sensing Technology. *Sensors* **2012**, *12*, 9635-9665.

49. Rodriguez, G. A.; Weiss, S. M. Nanoporous silicon biosensors for DNA sensing. *Porous Silicon for Biomedical Applications.* **2014**, 304-333.

50. Makra, I.; Terejánszky, P.; Gyurcsányi, P. E. A method based on light scattering to estimate the concentration of virus particles without the need for virus particle standards. *MethodsX*. **2015**, *2*, 91-99.

51. Minton A. P. Recent applications of light scattering measurement in the biological and biopharmaceutical sciences. *Anal Biochem*. **2016**, *15*, 501, 4-22.

52. Turick, C.E.; Shimpalee, S.; Satjaritanun, P.; Weidner, J.; Greenway, S. Convenient non-invasive electrochemical techniques to monitor microbial processes: current state and perspectives. *Appl Microbiol Biotechnol.* **2019**, *103*, 8327–8338.

53. Perry, D.; Mamlouk, M. Probing mass transport processes in Li-ion batteries using electrochemical impedance spectroscopy. *Journal of Power Sources*. **2021**, *514*, 230577.

54. Charoen-amornkitt, P.; Suzuki, T.; Tsushima, S. Ohmic resistance and constant phase element effects on cyclic voltammograms using a combined model of mass transport and equivalent circuits. *Electrochimica Acta.* **2017**, *258*, 433-441.

55. Forman, E. M.; Trujillo, M. A.; Ziegler, K. J.; Bradley, S. A.; Wang, H.; Prabhakar, S.; Vasenkov, S. Self-Diffusion of Heptane Inside Aggregates of Porous Alumina Particles by Pulsed Field gradient NMR. *Microporous and Mesoporous Materials*. **2016**, *229*, 117-123.

56. Takahara, S.; Nakano, M.; Kittaka, S.; Kuroda, Y.; Mori, T.; Hamano, H.; Yamaguchi, T. Neutron Scattering Study on Dynamics of Water Molecules in MCM-41. *J. Phys. Chem. B* **1999**, *103*, 5814− 5819.

57. Takahara, S.; Sumiyama, N.; Kittaka, S.; Yamaguchi, T.; Bellissent-Funel, M.-C. Neutron Scattering Study on Dynamics of Water Molecules in MCM-41. 2. Determination of Translational Diffusion Coefficient. *J. Phys. Chem. B* **2005**, *109*, 11231−11239.

58. Hungerford, G.; Rei, A.; Ferreira, M. I. C.; Tregidgo, C.; Suhling, K. Molecular Diffusion within Sol-Gel Derived Matrices Viewed via Fluorescence Recovery After Photobleaching. *Photochem. Photobiol. Sci.* **2007**, *6*, 825−828.

59. Weiss, A. M.; Saraidarov, T.; Reisfeld, R. Confocal Microscopy for Characterization of Porous Sol-Gel Glasses Incorporating Luminescent Dyes. *Opt. Mater.* **2001**, *16*, 15−20.

60. Okamoto, K.; Shook, C. J.; Bivona, L.; Lee, S. B.; English, D. S. Direct Observation of Wetting and Diffusion in the Hydrodynamic Interior of Silica. *Nanotures. Nano Lett.* **2004**, *4*, 233−239.

61. Tran-Ba, K.-H.; Higgins, D. A.; Ito, T. Fluorescence Recovery after Photobleaching and Single-Molecule Tracking Measurements of Anisotropic Diffusion within Identical Regions of a Cylinder-Forming Diblock Copolymer Film. *Anal. Chem*. **2015**, *87*, 5802−5809.

62. Higgins, D. A.; Park, S. C.; Tran-Ba, K.-H.; Ito, T. Single Molecule Investigations of Morphology and Mass Transport Dynamics in Nanostructured Materials. Annu. Rev. Anal Chem. **2015**, *8*, 193−216.

63. Wu, H.; Schwartz, D. K. Nanoparticle Tracking to Probe Transport in Porous Media. *Acc. Chem. Res.* **2020**, *53*, 2130−2139.

64. Neria, R. M.; Kisley, L. Single-Molecule Imaging in Commercial Stationary Phase Particles Using Highly Inclined and Laminated Optical Sheet Microscopy. *Anal. Chem.* **2023**, *95*, 2245−2252.

65. Ma, C.; Yeung, E. S. Entrapment of Individual DNA Molecules and Nanoparticles in Porous Alumina Membranes. *Anal. Chem.* **2010**, *82*, 654−657.

66. Shroff, H.; White, H.; Betzig, E. Photoactivated Localization Microscopy (PALM) of adhesion complexes. *Curr Protoc Cell Biol*. **2013** Chapter 4:4, 21,1-4,21, 28.

67. Manley, S.; Gillette, J.; Patterson, G.; Shroff, H.; Hess, H. F.; Betzig, E.; Lippincott-Schwartz, J. High-density mapping of single-molecule trajectories with photoactivated localization microscopy. *Nat Methods.* **2008**, *5*, 155–157.

68. Rust, M. J.; Bates, M.; Zhuang, X. Sub-diffraction-limit imaging by stochastic optical reconstruction microscopy (STORM). *Nat Methods*. **2006,** 3(10):793-5.

69. Hohlbein, J.; Steinhart, M.; Schiene-Fischer, C.; Benda, A.; Hof, M.; Hubner, C. G. Confined Diffusion in Ordered Nanoporous Alumina Membranes. *Small.* **2007**, *3*, 380−385.

70. Chen, F.; Neupane, B.; Li, P.; Su, W.; Wang, G. Investigating Axial Diffusion in Cylindrical Pores Using Confocal Single-Particle Fluorescence Correlation Spectroscopy. *Electrophoresis.* **2016**, *37*, 2129−2138.

71. Elson, E. L.; Magde, D. Fluorescence Correlation Spectroscopy. I. Conceptual Basis and Theory. *Biopolymers.* **1974**, *13*, 1−27.

72. Park, S.C.; Ito, T.; Higgins, D. A. "Dimensionality of Diffusion in Flow-Aligned Surfactant-Templated Mesoporous Slica: A Single Molecule Tracking Study of Pore Wall Permeability", *J. Phys. Chem. C*, **2015**, *119*, 26101-26110.

73. Park, S.C.; Ito, T.; Higgins, D. A. "Single Molecule Tracking Studies of Flow-Aligned Mesoporous Silica Monoliths: Aging-Time Dependence of Pore Order", *J. Phys. Chem. B*, **2013**, *117*, 4222-4230.

74. Pramanik, R.; Ito, T.; Higgins, D.A. "Single Molecule Wobbling in Cylindrical Mesopores", *J. Phys. Chem. C*, **2013**, *117*, 3668-3673.

75. Pramanik, R.; Ito, T.; Higgins, D. A. Molecular Length Dependence of Single Molecule Wobbling within Surfactant- and Solvent-Filled Silica Mesopores. *J. Phys. Chem. C* **2013**, *117*, 15438− 15446.

76. Kumarasinghe, R.; Ito, T.; Higgins, D. A. Nanoconfinement and Mass Transport in Silica Mesopores: the Role of Charge at the Single Molecule and Single Pore Levels. *Anal. Chem*. **2020**, *92*, 1416− 1423.

77. Kumarasinghe, R.; Higgins, E. D.; Ito, T.; Higgins, D. A. Spectroscopic and Polarization-Dependent Single-Molecule Tracking Reveal the One-Dimensional Diffusion Pathways in Surfactant Templated Mesoporous Silica. *J. Phys. Chem. C* **2016**, *120*, 715−723.

78. Kirstein, J.; Platschek, B.; Jung, C.; Brown, R.; Bein, T.; Brauchle, C. Exploration of Nanostructured Channel Systems with Single-Molecule Probes. *Nat. Mater*. **2007**, *6*, 303 310.

79. Zuerner, A.; Kirstein, J.; Doeblinger, M.; Bräuchle, C.; Bein, T. Visualizing Single Molecule Diffusion in Mesoporous Materials. *Nature*. **2007**, *450*, 705-708.

80. Jung, C.; Kirstein, J.; Platschek, B.; Bein, T.; Budde, M.; Frank, I.; Müllen, K.; Michaelis, J.; Bräuchle, C. Diffusion of Oriented Single Molecules with Switchable Mobility in Networks of Long Unidimensional Nanochannels. *J. Am. Chem. Soc.* **2008**, *130*, 1638-1648.

81. Ruehle, B.; Davies, M.; Lebold, T.; Bräuchle, C.; Bein, T. Highly Oriented Mesoporous Silica Channels Synthesized in Microgrooves and Visualized with Single-Molecule Diffusion. *ACS Nano.* **2012**, *6*, 1948-1960.

82. Jung, C.; Kirstein, J.; Platschek, B.; Bein, T.; Budde, M.; Frank, I.; Muellen, K.; Michaelis, J.; Bräuchle, C. Diffusion of Oriented Single Molecules with Switchable Mobility in Networks of Long Unidimensional Nanochannels. *J. Am. Chem. Soc.* **2008**, *130*, 1638-1648.

83. Rial, R. C. Biofuels versus climate change: Exploring potentials and challenges in the energy transition. *Renewable and Sustainable Energy Reviews.* **2024**, 114369.

84. Annual ethanol fuel production worldwide **2023** | Statista

85. Mekala, M.; Neerudi, B.; Are,P. R.; Surakasi, R.; Manikandan, G.; Kakara, V. R.; Dhumal, A.A. Water Removal from an Ethanol-Water Mixture at Azeotropic Condition by Adsorption Technique Adsorption. *Science & Technology*. **2022**, Article ID 8374471.

86. Bandaru, K.; Jana, A. A hybrid heat integration scheme for bioethanol separation through pressure-swing distillation route. *Separ. Purif. Technol.* **2015**, *142*, 307–315.

87. Gomis, V.; Pedraza, R.; Frances, O.; Font, A.; Asensi, J. C. Dehydration of ethanol using azeotropic distillation with isooctane. *Ind Eng Chem Res.* **2007**; *46*, 4572–6.

88. Gomis, V.; Font, A.; Pedraza, R.; Saquete, MD. Isobaric vapour–liquid and vapour–liquid–liquid equilibrium data for the system water + ethanol + cyclohexane. *Fluid Phase Equilib*, **2005**, *235*, 7–10.

89. Black, C.; Ditsler D. E. Dehydration of aqueous ethanol mixtures by extractive distillation. *Adv Chem Ser*. **1972**, *115*, 1–15.

90. Karimi, S.; Yaraki, M.T.; and Karri, R.R. A comprehensive review of the adsorption mechanisms and factors influencing the adsorption process from the perspective of bioethanol dehydration. *Renew. Sustain. Energy Rev.* **2019**, *107*, 535–553.

91. Kaminski, W.; Marszalek, J.; Ciolkowska, A. Renewable energy source—dehydrated ethanol. *Chem Eng J*. **2008,** *135*, 95–102.

92. Tsuyumoto, M.; Teramoto, A.; Meares, P. Dehydration of ethanol on a pilot-plant scale, using a new type of hollow-fibre membrane. *J Membr Sci.* **1997**, *133*, 83–94.

93. Kumar, S.; Singh, N.; Prasad, R. Anhydrous ethanol: A renewable source of energy, *Renewable and Sustainable Energy. Reviews.* **2010**, *14*, 1830–1844.

94. Rigler, R.; Mets, U.; Widengren, J.; Kask, P. Fluorescence correlation spectroscopy with high count rate and low background: analysis of translational diffusion. *Eur Biophys J Biophys Lett*. **1993**, *22*, 169-175.

95. Enderlein, J.; Gregor, I.; Patra, D.; Dertinger, T.; Kaupp, U. B. Performance of Fluorescence Correlation Spectroscopy for Measuring Diffusion and Concentration. Chem. Phys. Chem. **2005**, *6*, 2324−2336.

96. Ries, J.; Schwille, P. Fluorescence correlation spectroscopy. *BioEssays*, **2012**, *34*, 361-368.

97. https://materials.gelsonluz.com.

98. Koppel, D. E. Statistical Accuracy in Fluorescence Correlation Spectroscopy. *Phys. Rev.* A **1974**, *10*, 1938−1945.

99. Haustein, E.; Schwille, P. Fluorescence Correlation Spectros copy: Novel Variations of an Established Technique. *Annu. Rev. Biophys. Biomol. Struct*. **2007**, *36*, 151−169.

100. Widengren, J.; Mets, U.; Rigler, R. Fluorescence Correlation Spectroscopy of Triplet States in Solution: A Theoretical and Experimental Study. *J. Phys. Chem. A* **1995**, *99*, 13368−13379.

101. Banachowicz, E.; Patkowski, A.; Meier, G.; Klamecka, K.; Gapinski, J. Successful FCS Experiments in Nonstandard Conditions. *Langmuir*. **2014**, *30*, 8945−8955.

102. Culbertson, M. J.; Williams, J. T. B.; Cheng, W. W. L.; Stults, D. A.; Wiebracht, E. R.; Kasianowicz, J. J.; Burden, D. L. Numerical Fluorescence Correlation Spectroscopy for the Analysis of Molecular Dynamics under Nonstandard Conditions. *Anal. Chem*. **2007**, *79*, 4031−4039.

103. Gendron, P.-O.; Avaltroni, F.; Wilkinson, K. J. Diffusion Coefficients of Several Rhodamine Derivatives as Determined by Pulsed Field Gradient-Nuclear Magnetic Resonance and Fluorescence Correlation Spectroscopy. *J. Fluoresc.* **2008**, *18*, 1093−1101.

104. Ghiviriga, I. Nuclear Magnetic Resonance Method for Measuring Water Solubility of Organic Compounds. *Anal. Chem*. **2023**, *95*, 2706-2712.

105. Jani, A. M. M.; Losic, D.; Voelcker, N. H. Nanoporous Anodic Aluminum Oxide: Advances in Surface Engineering and Emerging Applications. *Prog. Mater. Sci*. **2013**, *58*, 636−704.

106. Lee, W.; Park, S. J. Porous Anodic Aluminum Oxide: Anodization and Templated Synthesis of Functional Nanostructures. *Chem. Rev*. **2014**, *114*, 7487−7556.

107. Sammi, H.; Nair, R. V.; Sardana, Sardana, N. Recent advances in nanoporous AAO based substrates for surface-enhanced raman scattering; Materials Today: *Proceedings.* **2021**, *41*, 843–850.

108. Santos, A.; Kumeria, T.; Losic, D. Optically Optimized Photoluminescent and Interferometric Biosensors Based on Nanoporous Anodic Alumina: A Comparison; *Anal. Chem.* **2013**, *85*, 7904−7911.

109. Brevnov, D. A.; Barela, M. J.; Brooks, M. J.; Lo´pez, G. P.; Atanassov, P. B. Fabrication of Anisotropic Super Hydrophobic/Hydrophilic Nanoporous Membranes by Plasma Polymerization of C 4 F 8 on Anodic Aluminum Oxide, *J. Electrochem. Soc.* **2004**, *151* B484.

110. Lei, Y.; Cai, W.; Wilde, G.; Highly ordered nanostructures with tunable size, shape and properties: A new way to surface nano-patterning using ultra-thin alumina masks, *Prog. Mater Sci*. **2007**, *52*, 465–539

111. Farrer, R. A.; Fourkas, J. T. Orientational Dynamics of Liquids Confined in Nanoporous Sol-Gel Glasses Studied by Optical Kerr Effect Spectroscopy. *Acc. Chem. Res*. **2003**, *36*, 605−612.

112. Kovaleva, E. G.; Molochnikov, L. S.; Tambasova, D.; Marek, A.; Chestnut, M.; Osipova, V. A.; Antonov, D. O.; Kirilyuk, I. A.; Smirnov, A. I. Electrostatic Properties of Inner Nanopore Surfaces of Anodic Aluminum Oxide Membranes upon High Temperature Annealing Revealed by EPR of pH-Sensitive Spin Probes and Labels. *J. Membr. Sci.* **2020**, *604*, No. 118084.

113. Muthulakshmi, T.; Dutta, D.; Maheshwari, P.; Pujari, P. K. Evidence for Confinement Induced Phase Separation in Ethanol Water Mixture: a Positron Annihiliation Study. *J. Phys.: Condens. Matter*. **2018**, *30*, No. 025001.

114. Kittaka, S.; Kuranishi, M.; Ishimaru, S.; Umahara, O. Phase Separation of Acetonitrile-Water Mixtures and Minimizing of Ice Crystallites From There in Confinement of MCM-41. *J. Chem. Phys.* **2007**, *126*, No. 091103.

115. Kennard, R.; DeSisto, W. J.; Mason, M. D. Molecular Diffusivity Measurement Through an Alumina Membrane Using Time-Resolved Fluorescence Imaging. *Appl. Phys. Lett.* **2010**, *97*, No. 213701.

116. Dong, B.; Mansour, N.; Huang, T. X.; Huang, W.; Fang, N. Single Molecule Fluorescence Imaging of Nanoconfinement in Porous Materials. *Chem. Soc. Rev*. **2021**, *50*, 6483−6506.

117. Higgins, D. A.; Tran-Ba, K.-H.; Ito, T. Following Single Molecules to a Better Understanding of Self-Assembled One Dimensional Nanostructures. *J. Phys. Chem. Lett*. **2013**, *4*, 3095−3103.

118. Michaelis, J.; Bräuchle, C. Reporters in the Nanoworld: Diffusion of Single Molecules in Mesoporus Materials. *Chem. Soc. Rev*. **2010**, *39*, 4731−4740.

119. Cooper, J. T.; Peterson, E. M.; Harris, J. M. Fluorescence Imaging of Single-Molecule Retention Trajectories in Reversed-Phase Chromatographic Particles. *Anal. Chem*. **2013**, *85*, 9363−9370.

120. Kennard, R.; DeSisto, W. J.; Giririjan, T. P.; Mason, M. D. Intrinsic Property Measurement of Surfactant-Templated Mesopo rous Silica Films Using Time-Resolved Single-Molecule Imaging. *J. Chem. Phys*. **2008**, *128*, No. 134710.

121. Ito, S.; Fukuya, S.; Kusumi, T.; Ishibashi, Y.; Miyasaka, H.; Goto, Y.; Ikai, M.; Tani, T.; Inagaki, S. Microscopic Structure and Mobility of Guest Molecules in Mesoporous Hybrid Organosilica: Evaluation with Single-Molecule Tracking. *J. Phys. Chem. C* **2009**, *113*, 11884−11891.

122. Han, R.; Wang, G.; Qi, S.; Ma, C.; Yeung, E. S. Electrophoretic Migration and Axial Diffusion of Individual Nanoparticles in Cylindrical Nanopores. *J. Phys. Chem. C* **2012**, *116*, 18460−18468.

123. Liao, Y.; Yang, S. K.; Koh, K.; Matzger, A. J.; Biteen, J. S. Heterogeneous Single-Molecule Diffusion in One-, Two-, and Three Dimensional Microporous Coordination Polymers: Directional, Trapped, and Immobile Guests. *Nano Lett.* **2012**, *12*, 3080−3085.

124. Bhatta, H.; Enderlein, J.; Rosengarten, G. Fluorescence Correlation Spectroscopy to Study Diffusion Through Diatom Nanopores. *J. Nanosci. Nanotechnol.* **2009**, *9*, 6760−6766.

125. Zhong, Z.; Lowry, M.; Wang, G.; Geng, L. Probing Strong Adsorption of Solute onto C18-Silica Gel by Fluorescence Correlation Imaging and Single-Molecule Spectroscopy under RPLC Conditions. *Anal. Chem*. **2005**, *77*, 2303−2310.

126. Molteni, M.; Ferri, F. Commercial Counterboard for 10 ns Software Correlator for Photon and Fluorescence Correlation Spectroscopy. *Rev. Sci. Instrum.* **2016**, *87*, No. 113108.

127. Enderlein, J.; Gregor, I.; Patra, D.; Fitter, J. Art and Artefacts of Fluorescence Correlation Spetroscopy. *Curr. Pharm. Biotechnol*. **2004**, *5*, 155−161.

128. Wirth, M. J.; Swinton, D. J. Single-Molecule Probing of Mixed Mode Adsorption at a Chromatographic Interface. *Anal. Chem*. **1998**, *70*, 5264−5271.

129. Ha, T.; Enderle, T.; Chemla, D. S.; Selvin, P. R.; Weiss, S. Quantum Jumps of Single Molecules at Room Temperature. *Chem. Phys. Lett*. **1997**, *271*, 1−5.

130. Khattab, I. S.; Bandarkar, F.; Fakhree, M. A. A.; Jouyban, A. Density, Viscosity, and Surface Tension of Water+Ethanol Mixtures from 293-323 K. *Korean J. Chem. Eng.* **2012**, *29*, 812-817.

131. Zhao, L.; Zhong, Y.; Wei, Y.; Ortiz, N.; Chen, F.; Wang, G. Microscopic Movement of Slow-Diffusing Nanoparticles in Cylin drical Nanopores Studied with Three-Dimensional Tracking. *Anal. Chem*. **2016**, *88*, 5122−5130.

132. Wirth, M. J.; Swinton, D. J.; Ludes, M. D. Adsorption and Diffusion of Single Molecules at Chromatographic Interfaces. *J. Phys. Chem. B* **2003**, *107*, 6258−6268.

133. Emin, A.; Hushur, A.; Mamtimin, T. Raman Study of Mixed Solutions of Methanol and Ethanol. *AIP Adv*. **2020**, *10*, 065330.

134. Pashchanka, M. Controllable Reduction of Anionic Contamination in Degradable Amorphous Anodic Alumina Nanoporous Membranes. *ACS Appl. Nano Mater*. **2020**, *3*, 10531-10542.

135. Li, F.; Men, Z.; Li, S.; Wang, S.; Li, Z.; Sun, C. Study of Hydrogen Bonding in Ethanol-Water Binary Solutions by Raman Spectroscopy. *Spectrochim. Acta A* **2018**, *189*, 621-624.

136. Zupancic, B.; Grdadolnik, J. Solute-Induced Changes in the Water H-Bond Network of Different Alcohol-Aqueous Systems. *J. Molec. Liq.* **2021**, *341*, 117349.

137. Dolenko, T. A.; Burikov, S. A.; Dolenko, S. A.; Efitorov, A. O.; Plastinin, I. V.; Yuzhakov, V. I.; Patsaeva, S. V. Raman Spectroscopy of Water-Ethanol Solutions: The Estimation of Hydrogen Bonding Energy and the Appearance of Clathrate-Like Structures in Solutions. *J. Phys. Chem. A* **2015**, *119*, 10806−10815.

138. Renkin, E. M. Filtration, Diffusion, and Molecular Sieving through Porous Cellulose Membranes. *J. Gen. Physiol*. **1954**, *38*, 225− 243.

139. Yamaguchi, S.; Shimada, K.; Matsui, K. Spectroscopic Study of Fluorescein Immobilized on Anodic Porous Alumina in Aqueous Solutions of Different pH. *Dyes Pigments*. **2020**, *173*, No. 107944.

140. Pedimonte, B. J.; Moest, T.; Luxbacher, T.; von Wilmowsky, C.; Fey, T.; Schlegel, K. A.; Greil, P. Morphological Zeta-Potential Variation of Nanoporous Anodic Alumina Layers and Cell Adherence. *Acta Biomater*. **2014**, *10*, 968−974.

141. Pandey, B.; Cox, C. B.; Thapa, P. S.; Ito, T. Potentiometric Response Characteristics of Oxide-Coated Gallium Electrodes in Aqueous Solutions. *Electrochim. Acta*. **2014**, *142*, 378−385.

142. Daniels, C. R.; Reznik, C.; Landes, C. F. Dye Diffusion at Surfaces: Charge Matters. *Langmuir*. **2010**, *26*, 4807−4812.

143. Walder, R.; Nelson, N.; Schwartz, D. K. Single Molecule Observations of Desorption-Mediated Diffusion at the Solid-Liquid Interface. *Phys. Rev. Lett.* **2011**, *107*, No. 156102.

144. Skaug, M. J.; Mabry, J.; Schwartz, D. K. Intermittent Molecular Hopping at the Solid-Liquid Interface. *Phys. Rev. Lett.* **2013**, *110*, No. 256101.

145. Wang, D.; Wu, H.; Schwartz, D. K. Three-Dimensional Tracking of Interfacial Hopping Diffusion. *Phys. Rev. Lett.* **2017**, *119*, No. 268001.

146. Giri, D.; Ashraf, K. M.; Collinson, M. M.; Higgins, D. A. Single Molecule Perspective on Mass Transport in Condensed Water Layers over Gradient Self-Assembled Monolayers. *J. Phys. Chem. C* **2015**, *119*, 9418−9428.

147. Marchetti, P.; Jimenez Solomon, M. F.; Szekely, G.; Livingston, A. G. Molecular Separation with Organic Solvent Nanofiltration: A Critical Review. *Chem. Rev.* **2014**, *114*, 10735−10806.

148. Wang, Z.; Wu, A.; Ciacchi, L. C.; Wei, G. Recent Advances in Nanoporous Membranes for Water Purification. *Nanomater.* **2018**, 8 (2), 65.

149. Zhao, Y.; Tong, T.; Wang, X.; Lin, S.; Reid, E. M.; Chen, Y. Differentiating Solutes with Precise Nanofiltration for Next Generation Environmental Separations: A Review. *Environ. Sci. Technol.* **2021**, *55*, 1359−1376.

150. Park, H. B.; Kamcev, J.; Robeson, L. M.; Elimelech, M.; Freeman, B. D. Maximizing the Right Stuff: The Trade-Off Between Membrane Permeability and Selectivity. *Science.* **2017**, *356*, No. eaab0530.

151. Fayer, M. D.; Levinger, N. E. Analysis of Water in Confined Geometries and at Interfaces. Annu. Rev. *Anal Chem*. **2010**, *3*, 89−107.

152. Levinger, N. E. Water in Confinement. *Science.* **2002**, *298*, 1722− 1723.

153. Aluru, N. R.; Aydin, F.; Bazant, M. Z.; Blankschtein, D.; Brozena, A. H.; de Souza, J. P.; Elimelech, M.; Faucher, S.; Fourkas, J. T.; Koman, V. B.; et al. Fluids and Electrolytes under Confinement in Single-Digit Nanopores. *Chem. Rev*. **2023**, *123*, 2737−2831.

154. Thompson, W. H. Perspective: Dynamics of Confined Liquids. *J. Chem. Phys*. **2018**, *149*, 170901.

155. Zhang, J.; Liu, G.; Jonas, J. Effects of Confinement on the Glass Transition Temperature of Molecular Liquids. *J. Phys. Chem*. **1992**, *96*, 3478−3480.

156. Angarita, I.; Mazzobre, M. F.; Corti, H. R.; Longinotti, M. P. Revisiting the Glass Transition Temperature of Water-Glycerol Mixtures in the Bulk and Confined in Mesoporous Silica. *Phys. Chem. Chem. Phys.* **2021**, *23*, 17018−17025.

157. Richert, R. Dynamics of Nanoconfined Supercooled Liquids. *Annu. Rev. Phys. Chem*. **2011**, *62*, 65−84.

158. Fumagalli, L.; Esfandiar, A.; Fabregas, R.; Hu, S.; Ares, P.; Janardanan, A.; Yang, Q.; Radha, B.; Taniguchi, T.; Watanabe, K.; Gomila, G.; Novoselov, K. S.; Geim, A. K. Anomalously Low Dielectric Constant of Confined Water. *Science* **2018**, *360*, 1339−1342.

159. Blom, H.; Hassler, K.; Chmyrov, A.; Widengren, J. Electrostatic Interactions of Fluorescent Molecules with Dielectric Interfaces Studies by Total Internal Reflection Fluoresence Correlation Spectroscopy. Int. *J. Mol. Sci*. **2010**, *11*, 386−406.

160. Rashidi, H.; Howard, K. J.; Ito, T.; Higgins, D. A. Random Walks and Sticky Surfaces: Single Molecule Measurements of Solute Diffusion in Ethanol/Water-Filled Anodic Alumina Nanopores. *J. Phys. Chem. C* **2023**, *127*, 411−420.

161. Eid, J. S.; Muller, J. D.; Gratton, E. Data Acquisition Card for Fluctuation Correlation Spectroscopy Allowing Full Access to the Detected Photon Sequence. *Rev. Sci. Instrum*. **2000**, *71*, 361−368.

162. Ye, F.; Collinson, M. M.; Higgins, D. A. Molecular Orientation and Its Influence on Autocorrelation Amplitudes in Single-Molecule Imaging Experiments. *Anal. Chem.* **2007**, *79*, 6465−6472.

163. Wang, P.; Jiang, J.; He, L.; Li, J.; Liu, J.; Liu, X.; Luo, M.; Ma, Z.; Qiu, S.; Wu, H.; Zhao, Y. Solubility of Isomalt in the Water + Ethanol Solvent System at (288.15, 298.15, 308.15, and 318.15) K. *J. Chem. Eng. Data* **2013**, *58*, 364-369.

164. Qiu, J.; Albrecht, J.; Janey, J. Synergistic Solvation Effects: Enhanced Compound Solubility Using Binary Solvent Mixtures. *Org. Process Res. Dev*.**2019**, *23*, 1343-1351.

165. Bychuk, O. V.; O'Shaughnessy, B. Anomalous Surface Diffusion: A Numerical Study. *J. Chem. Phys.* **1994**, *101*, 772−780.

166. Bychuk, O. V.; O'Shaughnessy, B. Anomalous Diffusion at Liquid Surfaces. *Phys. Rev. Lett.* **1995**, *74*, 1795−1798.

167. Chechkin, A. V.; Zaid, I. M.; Lomholt, M. A.; Sokolov, I. M.; Metzler, R. Bulk-Mediated Diffusion on a Planar Surface: Full Solution. *Phys. Rev. E* **2012**, *86*, 041101.

168. Wyman, J. The Dielectric Constant of Mixtures of Ethyl Alcohol and Water from −5 to 40°. *J. ACS.* **1931**, *53*, 3292-3301.

169. Rashidi, H.; Nathani, A.; Wang, X.; Servis, M.J.; Ito, T.; Higgins, D.A. Adsorption and Solvation Modulate Rhodamine B Diffusion in Ethanol/Water-Filled Anodic Alumina Nanopores. *J. Phys. Chem. C* **2024**, *128*, 34, 14326–14336.

170. Ito, T. Single-Molecule Fluorescence Investigations of Solute Transport Dynamics in Nanostructured Membrane Separation Materials. *J. Phys. Chem. B* **2023**, *127*, 5733−5741.

171. Williams, A. T.; Rangel-Buitrago, N. The Past, Present, and Future of Plastic Pollution. *Mar. Pollut. Bull.* **2022**, *176*, 113429.

172. Alimi, O. S.; Budarz, J. F.; Hernandez, L. M.; Tufenkji, N. Microplastics and Nanoplastics in Aquatic Environments: Aggregation, Deposition, and Enhanced Contaminant Transport. *Environ. Sci. Technol.* **2018**, *52*, 1704-1724.

173. Yu, Q.; Hu, X.; Yang, B.; Zhang, G.; Wang, J.; Ling, W. Distribution, Abundance and Risks of Microplastics in the Environment. *Chemosphere.* **2020**, *249*, 126059.

174. Richarson, S. D.; Kimura, S. Y. Water Analysis: Emerging Contaminants and Current Issues. *Anal. Chem.* **2016**, *88*, 546-582.

175. Frias, J. P. G. L.; Nash, R. Microplastics: Finding a Consensus of the Definition. *Mar. Poll. Bull.* **2019**, *138*, 145-147.

176. SAPEA, A. Scientific Perspective on Microplastics in Nature and Society. SAPEA: Berlin, **2019**.

177. Yu, F.; Yang, C.; Zhu, Z.; Bai, X.; Ma, J. Adsorption Behavior of Organic Pollutants and Metals on Micro/Nanoplastics in the Aquatic Environment. *Sci. Tot. Environ.* **2019**, *694*, 133643.

178. Costigan, E.; Collins, A.; Hatinoglu, M. D.; Bhagat, K.; MacRae, J.; Perreault, F.; Apul, O. Adsorption of Organic Pollutants by Microplastics: Overview of a Dissonant Literature. *J. Haz. Mat. Adv.* **2022**, *6*, 100091.

179. Kwon, J.-H.; Chang, S.; Hong, S. H.; Shim, W. J. Microplastics as a Vector of Hydrophobic Contaminants: Importance of Hydrophobic Additives. *Integ. Environ. Assess. Management* **2017**, *13*, 494-499.

180. Verla, A. W.; Enyoh, C. E.; Verla, E. N.; Nwarnorh, K. O. Microplastic-Toxic Chemical Interaction: a Review Study of Quantified Levels, Mechanism and Implication. *SN Appl. Sci.* **2019**, *1*, 1400.

181. Endo, S.; Takizawa, R.; Okuda, K.; Takada, H.; Chiba, K.; Kanehiro, H.; Ogi, H.; Yamashita, R.; Date, T. Concentration of Polychlorinated Biphenyls (PCBs) in Beached Resin Pellets: Variability Among Individual Particles and Regional Differences. *Mar. Pollut. Bull.* **2005**, *50*, 1103-1114.

182. Andrady, A. L. Microplastics in the Marine Environment. *Mar. Pollut. Bull.* **2011**, *62*, 1596-1605.

183. Du, H.; Zhang, Y.; Jiang, H.; Wang, H. Adsorption of Rhodamine B on Polyvinyl Chloride, Polystyrene, and Polyethylene Terephthalate Microplastics in Aqueous Environments. *Environ. Tech. Innov.* **2022**, *27*, 102495.

184. Lee, H.; Shim, W. J.; Kwon, J.-H. Sorption Capacity of Plastic Debris for Hydrophobic Organic Chemicals. *Sci. Tot. Environ.* **2014**, *470-471*, 1545-1552.

185. Wu, C.; Zhang, K.; Huang, X.; Liu, J. Sorption of Pharmaceuticals and Personal Care Products to Polyethylene Debris. *Environ. Sci. Pollut. Res.* **2016**, *23*, 8819-8826.

186. Goedecke, C.; Mülow-Stolin, U.; Hering, S.; Richter, J.; Piechotta, C.; Paul, A.; Braun, U. A First Pilot Study on the Sorption of Environmental Pollutants on Various Microplastic Materials. *J. Environ. Anal. Chem.* **2017**, *4*, 1000191.

187. Seidensticker, S.; Zarfl, C.; Cirpka, O. A.; Grathwohl, P. Microplastic-Contaminant Interactions: Influence of Nonlinearity and Coupled Mass Transfer. *Environ. Toxic. Chem.* **2019**, *38*, 1635-1644.

188. Hüffer, T.; Hofmann, T. Sorption of Non-Polar Organic Compounds by Micro-Sized Plastic Particles in Aqueous Solution. *Environ. Pollut.* **2016**, *214*, 194-201.

189. Al Harraq, A.; Brahana, P. J.; Arcemont, O.; Zhang, D.; Valsaraj, K. T.; Bharti, B. Effects of Weathering on Microplastic Dispersibility and Pollutant Uptake Capacity. *ACS Environ. Au* **2022**, *2*, 549– 555,

190. Bhagat, K.; Barrios, A. C.; Rajwade, K.; Kumar, A.; Oswald, J.; Apul, O.; Perreault, F. Aging of Microplastics Increases Their Adsorption Affinity Towards Organic Contaminants. *Chemosphere.* **2022**, *298*, 134238.

191. Hankett, J. M.; Collin, W. R.; Yang, P.; Chen, Z.; Duhaime, M. Low-Volatility Model Demonstrates Humidity Affects Environmental Toxin Deposition on Plastics at a Molecular Level. *Environ. Sci. Technol.* **2016**, *50*, 1304-1312.

192. Wang, W.; J., W. Different Partition of Polycyclic Aromatic Hydrocarbon on Environmental Particulates in Freshwater: Microplastics in Comparison to Natural Sediment. *Ecotox. Envir. Safe.* **2018**, *147*, 648-655.

193. Llorca, M.; Schirinzi, G.; Martínez, M.; Barceló, D.; Farré, M. Adsorption of Perfluoroalkyl Substances on Microplastics Under Environmental Conditions. *Environ. Pollut.* **2018**, *235*, 680-691.

194. Shim, W. J.; Song, Y. K.; Hong, S. H.; Jang, M. Identification and Quantification of Microplastics Using Nile Red Staining. *Mar. Pollut. Bull.* **2016**, *113*, 469-476.

195. Maes, T.; R., J.; Wellner, N.; Haupt, K.; Mayes, A. G. A Rapid-Screening Approach to Detect and Quantify Microplastics Based on Fluorescent Tagging with Nile Red. *Sci. Rep.* **2017**, *7*, 44501.

196. Erni-Cassola, G.; Gibson, M. I.; Thompson, R. C.; Christie-Oleza, J. A. Lost, but Found with Nile Red: A Novel Method for Detecting and Quantifying Small Microplastics (1 mm to 20 μm) in Environmental Samples. *Environ. Sci. Technol.* **2017**, *51*, 13641-13648.

197. Magde, D.; Elson, E.; Webb, W. W. Thermodynamic Fluctuations in a Reacting System - Measurement by Fluorescence Correlation Spectroscopy. *Phys. Rev. Lett.* **1972**, *29*, 705-708.

198. Aragon, S. R.; Pecora, R. Fluorescence Correlation Spectroscopy as a Probe of Molecular Dynamics. *J. Chem. Phys.* **1976**, *64*, 1791-1803.

199. Vasseghian, Y.; Hosseinzadeh, S.; Khataee, A.; Dragoi, E.-N. The Concentration of Persistent Organic Pollutants in Water Resources: A Global Systematic Review, Meta-Analysis and Probabilistic Risk Assessment. *Sci. Tot. Environ.* **2021**, *796*, 149000.

200. Tsironi, T. N.; Chatzidakis, S. M.; Stoforos, N. G. The Future of Polyethylene Terephthalate Bottles: Challenges and Sustainability. *Packag. Technol. Sci.* **2021**, *35*, 317-325.

201. Baird, C.; Cann, M.: Environmental Chemistry; Fifth ed.; *W. H. Freeman*. New York, **2012**.

202. Lin, C.-C.; Krommenhoek, P. J.; Watson, S. S.; Gu, X. Depth Profiling of Degradation of Multilayer Photovoltaic Backsheets after Accelerated Laboratory Weathering: Cross sectional Raman Imaging. *Solar Energy Mater. Solar Cell.* **2016**, *144*, 289-299.

203. Liang, C. Y.; Krimm, S. Infrared Spectra of High Polymers Part IX. Polyethylene Terephthalate. *J. Mol. Spectrosc.* **1959**, *3*, 554-574.

204. Stalder, A. F.; Melchior, T.; Mueller, M.; Sage, D.; Blu, T.; Unser, M. Low-Bond Axisymmetric Drop Shape Analysis for Surface Tension and Contact Angle Measurements of Sessile Drops. *Colloids Surf. A.* **2010**, *364*, 72-81.

205. Rebollar, E.; Pérez, S.; Hernández, M.; Domingo, C.; Martín, M.; Ezquerra, T. A.; Garcia-Ruiz, J. P.; Castillejo, M. Physicochemical Modifications Accompanying UV Laser Induced Surface Structures on Poly(ethylene terephthalate) and Their Effect on Adhesion of Mesenchymal Cells. *Phys. Chem. Chem. Phys.* **2014**, *16*, 17551-17559.

206. Teare, D. O. H.; Ton-That, C.; Bradley, R. H. Surface Characterization and Ageing of Ultraviolet-Ozone-Treated Polymers Using Atomic Force Microscopy and X-Ray Photoelectron Spectroscopy. *Surf. Interf. Anal.* **2000**, *29*, 276-283.

207. Gotoh, K.; Kobayashi, Y.; Yasukawa, A.; Ishigami, Y. Surface Modification of PET Films by Atmospheric Pressure Plasma Exposure with Three Reactive Gas Sources. *Colloid. Polym. Sci.* **2012**, *290*, 1005-1014.

208. Stubbins, A.; Lavender Law, K.; Muñoz, S. E.; Bianchi, T. S.; Zhu, L. Plastics in the Earth System. *Science.* **2021**, *373*, 51-55.

209. Rozman, U.; Kalcikova, G. Seeking for a Perfect (Non-spherical) Microplastic Particle - The Most Comprehensive Review on Microplastic Laboratory Research. *J. Haz. Mater*. **2022**, *424*, 127529.

210. Krichevsky, O.; Bonnet, G Fluorescence Correlation Spectroscopy: The Technique and its Applications. *Rep. Prog. Phys.* **2002**, *65*, 251– 297.